Westfälische Wilhelms-Universität Münster
Fachbereich Physik

Source Analysis of Simultaneous sEEG and iEEG Measurements in Presurgical Epilepsy Diagnosis

von
Christian Röer

Diplomarbeit in Physik

27. Juni 2008

Angefertigt am

Institut für Theoretische Physik
Westfälische Wilhelms-Universität Münster
bei Prof. Dr. R. Friedrich

Institut für Biomagnetismus und Biosignalanalyse
Universitätsklinikum Münster
bei Prof. Dr. C. Pantev

Zusammenfassung

Mit Hilfe von Elektro- (EEG) und Magnetoenzephalographie (MEG) ist es möglich, die elektrischen Potential auf der Kopfhaut bzw. die magnetischen Felder in geringer Entfernung von der Kopfoberfläche zu messen, die durch elektrische Ströme in aktiven Gehirnarealen entstehen. Beide Verfahren finden Anwendung sowohl in der Forschung (z.B. in der Epilepsie-Forschung) als auch im klinischen Alltag.

Das sog. *inverse Problem* beschreibt die Aufgabe, die zu einer gemessenen Potential- oder Magnetfeldverteilung gehörende Quellstromdichte innerhalb des Gehirns zu finden. Zur Lösung dieses Problems ist es nötig, das EEG/MEG-Signal an den Messelektroden für gegebene Stromdichtekonfigurationen zu simulieren. Dieses Problem bezeichnet man als *Vorwärtsproblem.*

Zur Lösung des Vorwärtsproblems bedient man sich verschiedener analytischer und numerischer Verfahren. In dieser Arbeit wurde die *Finite Elemente Methode (FEM)* benutzt. Zur Anwendung der FEM ist es erforderlich, das Untersuchungsgebiet zu diskretisieren. Hierzu kamen Tetraeder-Netze zum Einsatz, welche mit der Software TetGen erstellt wurden.

Im vierschaligen isotropen Kugelmodell wurden mit Anwendung der FEM für einen Subtraktionsansatz zum ersten Mal relative Fehler von unter 1 % für dipolare Quellen mit 2 mm Abstand zum nächsten Leitfähigkeitssprung gefunden. Die hohe Genauigkeit beruht auf der qualitativen Güte der Tetraedernetze und der Netzfeinheit in den äußeren Schichten. Basierend auf den Ergebnissen der Netzgenerierung wurde ein Paper[1] zur Veröffentlichung eingereicht.

Nach der erfolgreichen Validierung der FEM in Kugelmodellen wurden die Netzgenerierungstechniken auf ein realistisches Kopfmodell eines Epilepsie-Patienten angewandt, der ein intrakranielles Elektrodenmessgitter (iEEG) für kortikale Oberflächenmessungen implantiert bekam. Gleichzeitig wurde ein Oberflächen-EEG (sEEG) aufgenommen, um die simultane Auswertung von iEEG- und sEEG-Daten unter Berücksichtigung des bei der Implantation entstandenen Lochs in der Schädeldecke und der Kunststofffolie zu ermöglichen.

Anschließend wurde die FEM zur Lokalisierung einer gemessenen peri-iktalen ICA (*Independent Component Analysis*)-EEG-Komponente benutzt. Dabei wurde die dipolare Quelle anhand des iEEG-Signales direkt unter dem Gitter lokalisiert, während die auf dem Oberflächen-EEG basierende Rekonstruktion zu tief im Gehirn lag. Dieses Ergebnis legt die Vermutung nahe, dass die Annahme, dass die zugrundeliegende Quelldistribution der iEEG- und sEEG-Signale bei simultaner iEEG/sEEG-ICA identisch ist, kritisch hinterfragt werden muss.

In allen Untersuchungen konnte jedoch gezeigt werden, dass sich mittels der FEM sowohl das Vorwärtsproblem als auch das inverse Problem bei der Quell-Lokalisierung im menschlichen Gehirn akkurat und mit der Transfermatrixmethode auch sehr schnell lösen lässt.

Contents

1 Introduction

Understanding how the human brain processes information is the key question in modern neuroscience. Different imaging techniques are therefore applied to study active areas during certain cognitive tasks or to locate pathogenic tissue e. g. in epilepsy patients.

Among those is the *functional magnetic resonance imaging (fMRI)*, which extends the classical MRI method with a functional part. It measures the magnetization changes, that occur due to variations in the blood oxygenation level of activated cortical areas (*blood oxygenation level dependency (BOLD)*). With fMRI it is possible to localize active brain areas with a spatial resolution of three to six millimeters, though the temporal resolution is in the dimension of some seconds. Furthermore brain activity is measured indirectly through the BOLD-signal, whereas other methods aim directly at the generated electrical signals.

Electro- (EEG) and Magnetoencephalography are important tools both in clinical practice and research as well as in cognitive neuroscience. They are based on the electric currents, that are produced in active cortical areas. These currents produce electric potentials and magnetic fields, that can be measured outside or on the surface of the head using sufficiently sensible sensors.

For the first time H. Berger published in 1929 his results of measuring electrical activity directly on the brain surface[2]. Because of its small amplitudes the magnetic counterpart took about forty years longer to acquire and finally in 1968 D. Cohen was able to record the MEG of a human brain[3]. The breakthrough for developing more sensible MEG sensors came with the invention of *Superconducting Quantum Interface Devices (SQUID)*, that allowed for very accurate measuring of very small changes in the magnetic field[4]. The great advantage of EEG/MEG over other brain imaging techniques is their high temporal resolution of less than one millisecond.

Today the tendency is to measure EEG and MEG simultaneously to combine the information provided by both modalities.

In the field of source analysis EEG/MEG data are evaluated in order to localize the active brain area which generated the measured potentials and fields. Methods to compute the original current distribution (a procedure called the *inverse problem*) heavily rely on the accurate modeling of the potential distribution that a given source will generate (the *forward problem*). As analytical solutions for the forward problem usually only exist for special geometries (such as spherical volume conductors), there exist several methods to solve the forward problem numerically. Among these are the *Finite Difference Method (FDM)*, the *Boundary Element Method (BEM)* or the *Finite Element Method (FEM)*.

In this thesis the FEM was used because of its flexibility and the possibility to model anisotropy and very complex geometries. After validating EEG forward calculations in multilayer sphere models of varying complexity the FEM was applied to model a thin plastic sheet with intracranial EEG (iEEG) electrodes, that an epilepsy patient had implanted for monitoring. The skull had to be trepanated to place the iEEG directly on the cortex surface in order to localize the epileptogenic tissue with the maximal possible accuracy.

For evaluation of the simultaneously recorded surface EEG (sEEG), which is a non-standard procedure and difficult to perform because of the need for a pressure bandage and the danger of infection, an *Independent Component Analysis* (ICA) was performed in [5], so the simultaneous analysis of the sEEG/iEEG-dataset was possible.

Because of the very complex geometry (skull trepanation hole) and the fact that the skull was modeled as anisotropic conductor the BEM is inferior to the FEM in this case.

For all FEM calculations in this thesis the software toolbox SimBio[6] was used. Visualization was done using SCI's BioPSE package[7].

2 Theory

In this chapter a general overview of the theoretical background for bioelectricity especially concerning the human head shall be given and the used methods and algorithms will be explained.

2.1 Basics of Bioelectricity

The electric potential differences and magnetic fields that can be measured outside the human body by means of EEG and MEG are caused by electric currents inside. As this thesis focuses on modeling the human head and brain and the current distributions inside, a short overview of the anatomical structure and physiology of the brain is presented.

The human brain basically consists of three parts (see Figure 2.1), the *brain stem* consisting of diencephalon, midbrain, pons and medulla oblongata, the *cerebellum* and the *telencephalon* or cerebrum, the biggest part of the brain which is responsible for such complex tasks as movement and sensory or language processing. The telencephalon is divided into two symmetric hemispheres which are separated by the *medial longitudinal fissure*, a deep gap running from frontal to dorsal direction. The two hemispheres are connected through several commissures with the *corpus callosum* as largest fiber bundle.

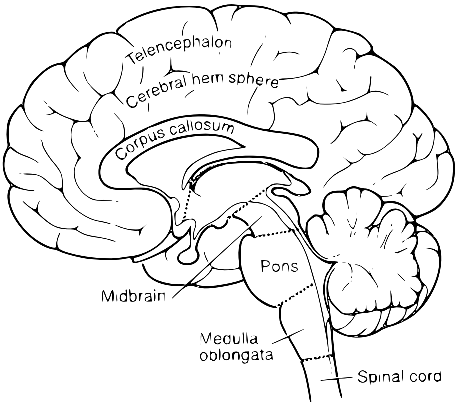

Figure 2.1: Anatomical overview of the brain (from [8])

The surface of each hemisphere is two to four millimeters thick and called *cortex* or gray matter. It is strongly folded into deep grooves called *sulci* which are surrounded by the *gyri*. The cortex consists of a large number of nerve cells (mostly pyramidal *neurons*) arranged in six layers whereas the underlying *white matter* is composed of nerve fibers connecting different parts of the brain. By interactions of these neurons information is processed and stored.

A neuron (Figure 2.2) mainly consists of three parts, the cell body or *soma*, the dendrites and the axon. The dendrites are used to receive electrical signals from other neurons, that can be transmitted to further neurons by the axon. Therefore a neuron has many dendrites yet only one axon. The connection of one neuron's axon to another neuron's dendrite is called *synapse*.

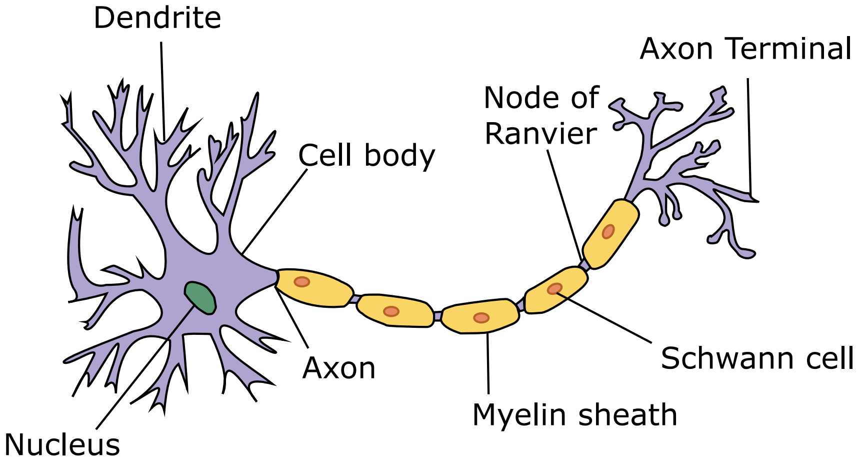

Figure 2.2: Schematic drawing of a neuron (from [9])

The signal transmission is achieved by electric potential changes that are caused by ion diffusion. When the neuron is at rest, a *resting membrane potential* of -50 to -80 mV can be measured between the inside (negatively charged) and the outside of the cell. It is caused by the diffusion of K^+-ions to the outside of the neuron, that is driven by a concentration gradient between the extra- and intracellular liquid. The diffusion continues until an equilibrium is reached between the electric force caused by the resting membrane potential and the diffusion force caused by the ion concentration gradient.

The resting membrane potential however is not a source of the signals measured by EEG or MEG. Instead two mechanisms of neuron-neuron-interaction can be considered to generate such potential differences.

The first process is the *action potential*, which erupts when the membrane potential is increased by about 20 mV by an external stimulus. The Na^+-ion channels suddenly open and sodium ions can diffuse into the cell. The inflow results in further depolarization and a positivity inside the neuron's cell body which gives rise to the action potential with an amplitude of about 60 to 100 mV. As this polarization process lasts only for about 1 ms and as the K^+-ion channels are opened simultaneously a repolarization back to the resting membrane potential occurs. A model to describe the initiation and propagation of action potentials is the Hodgkin-Huxley model[10], where the biological components are represented by their electrical counterparts.

The whole process of action potential rise and repolarization back to the membrane resting potential occurs very fast, it takes only 0.5 – 2 ms. Because of this short time and as even for synchronous activity across simultaneous active neurons the action potentials are not in perfect synchronization the generated signals are too weak to be measured from outside the body.

Another process of electric signal generation that appears in neurons is the occurrence of *excitatory postsynaptic potentials (EPSP)*. When an electric signal travels from the axon to the synapse the signal is transmitted through the synapse chemically. Certain messenger substances are emitted in the synapse, that, when arriving at the dendrite end cause an increase of the membrane potential of the receiving cell. This depolarization of the dendrites is called excitatory postsynaptic potential.

This potential, which lasts for some ten milliseconds, causes electrical currents to flow through the extracellular liquids and can cause the firing of an action potential in the receiving cell. If many neighboring neurons are simultaneously generating EPSPs (10000 – 50000, [11]), the resulting signals will be measurable from outside by means of EEG/MEG. This was also proved in animal experiments, where the potentials inside the cell and outside the head were measured simultaneously.

So the source of the signals that are measured in EEG/MEG are the excitatory post synaptic potentials of many simultaneously active neurons.

2.2 Physical Modeling

The fundamental equations governing electrodynamics are the Maxwell equations (2.1). From these a partial differential equation for the electric potential can be derived which can then be simplified by a quasi-static approximation of the dynamic effects.

The starting point for the derivation are the Maxwell equations for the magnetic flux density $\boldsymbol{B}$, the electric and magnetic fields $\boldsymbol{E}$ and $\boldsymbol{H}$ and the electric displacement field $\boldsymbol{D}$ in differential form:

$$\nabla \cdot \boldsymbol{B} = 0 \tag{2.1a}$$

$$\nabla \times \boldsymbol{E} + \dot{\boldsymbol{B}} = 0 \tag{2.1b}$$

$$\nabla \cdot \boldsymbol{D} = \varrho \tag{2.1c}$$

$$\nabla \times \boldsymbol{H} - \dot{\boldsymbol{D}} = \boldsymbol{j}. \tag{2.1d}$$

Here $\boldsymbol{j}$ is the current density and ϱ the electric charge. As biological tissue can be treated as an electrolyte the material equations for a linear homogeneous medium can be used:

$$\boldsymbol{B} = \mu_0 \boldsymbol{H} \tag{2.2a}$$

$$\boldsymbol{D} = \varepsilon_r \varepsilon_0 \boldsymbol{E}. \tag{2.2b}$$

Because biological tissue is non-magnetic the relative magnetic permittivity μ_r is assumed to be equal to one: $\mu_r = 1$. Furthermore μ_0 describes the vacuums permeability and ε_r and ε_0 stand for the relative permittivity and the permittivity of free space, respectively.

Generally in bioelectricity the current density $\boldsymbol{j}$ on the right hand of (2.1d) is divided into two parts: the impressed or *primary currents* $\boldsymbol{j}_p$, that represent the electric source distribution in the brain and the ohmic *return currents* $\sigma \boldsymbol{E}$:

$$\boldsymbol{j} = \boldsymbol{j}_p + \sigma \boldsymbol{E}. \tag{2.3}$$

Inserting (2.3) in (2.1d) leads to

$$\nabla \times \boldsymbol{H} - \dot{\boldsymbol{D}} = \boldsymbol{j}_p + \sigma \boldsymbol{E}. \tag{2.4}$$

It is now possible to introduce potentials $\boldsymbol{A}, \phi$ that automatically fulfill the homogeneous Maxwell equations (2.1a) and (2.1b):

$$\boldsymbol{B} = \nabla \times \boldsymbol{A} \tag{2.5a}$$

$$\boldsymbol{E} = -\nabla\phi - \dot{\boldsymbol{A}} \tag{2.5b}$$

The vector potential $\boldsymbol{A}$ and the scalar potential ϕ have to be determined by solving the inhomogeneous Maxwell equations (2.1c) and (2.1d). Eq. (2.5) however does not uniquely determine $\boldsymbol{A}$ and ϕ, as the magnetic flux density $\boldsymbol{B}$ obviously does not change if $\boldsymbol{A}$ is transformed to $\bar{\boldsymbol{A}}$:

$$\bar{\boldsymbol{A}} = \boldsymbol{A} + \nabla\chi. \tag{2.6}$$

The function $\chi = \chi(\boldsymbol{r}, t)$ is an arbitrary scalar function. Of course ϕ has to be transformed as well:

$$\bar{\phi} = \phi - \dot{\chi}. \tag{2.7}$$

As the resulting fields $\boldsymbol{E}$ and $\boldsymbol{B}$ are not changed by this *gauge transformation*, the choice of a suitable gauge is free.

A useful gauge fixing for the electrodynamic case is the fulfillment of the *Lorenz condition*

$$\nabla \cdot \boldsymbol{A} + \mu_0\varepsilon_r\varepsilon_0\dot{\phi} + \mu_0\sigma\phi = 0. \tag{2.8}$$

To derive an equation for the potential ϕ the divergence of (2.4) is taken, the material equations (2.2) are used and the auxiliary potentials (2.5) are inserted. Assuming harmonic time dependencies of $\boldsymbol{j}_p$, $\boldsymbol{A}$ and ϕ,

$$\boldsymbol{A}(\boldsymbol{r}, t) = \boldsymbol{A}(\boldsymbol{r})\,\mathrm{e}^{\mathrm{i}\omega t} \tag{2.9a}$$

$$\boldsymbol{j}_p(\boldsymbol{r}, t) = \boldsymbol{j}_p(\boldsymbol{r})\,\mathrm{e}^{\mathrm{i}\omega t} \tag{2.9b}$$

$$\phi(\boldsymbol{r}, t) = \phi(\boldsymbol{r})\,\mathrm{e}^{\mathrm{i}\omega t}, \tag{2.9c}$$

leads to the following partial differential equation for ϕ and $\boldsymbol{A}$:

$$\nabla \cdot \left(\sigma\left(1 + \frac{\mathrm{i}\omega\varepsilon_0\varepsilon_r}{\sigma}\right)\nabla\phi + \sigma\mathrm{i}\omega\left(1 + \frac{\mathrm{i}\omega\varepsilon_0\varepsilon_r}{\sigma}\right)\boldsymbol{A}\right) = \nabla \cdot \boldsymbol{j}_p. \tag{2.10}$$

It describes three kinds of dynamic effects, that can be neglected when applied to the calculation of EEG (and MEG) potentials: propagation effects, capacitive effects and induction effects.

Before these effects are discussed a quick overview for some electrical properties of biological materials is given to provide numerical values for necessary error approximations.

As it becomes necessary to consider complex conductivities of the form $\sigma\left(1 + \frac{\mathrm{i}\omega\varepsilon_r\varepsilon_0}{\sigma}\right)$, the numerical values of the ratio of capacitive to resistive currents $\frac{\mathrm{i}\omega\varepsilon_r\varepsilon_0}{\sigma}$ are of interest. Measured values for this ratio of several different tissues at different frequencies are listed in Table 2.1 (from [12]). The highest relevant frequency in bioelectric systems is of the order of 1 kHz, as the rise of the action potential with a duration of about 1 ms is the fastest process of significance.

	10 Hz	**100 Hz**	**1 000 Hz**	**10 000 Hz**
Lung	0.15	0.025	0.05	0.14
Fatty Tissue		0.01	0.03	0.15
Liver	0.20	0.035	0.06	0.20
Heart Muscle	0.10	0.04	0.15	0.32

Table 2.1: Averages of Ratio Capacitive to Resistive Current for Various Frequencies and Body Tissues (from [12])

It was already mentioned that biological tissue usually is non-magnetic, so the permeability μ is that of free space $\mu_0 = 4\pi \cdot 10^{-7}$ H/m. The maximal distance of relevance when discussing fields in the human body and especially the brain is chosen to $R = 1$ m.

Propagation effects

For an infinite homogeneous medium (2.10) can be solved using Green's function

$$G_k(R) = \frac{\mathrm{e}^{-\mathrm{i}kR}}{R}, \tag{2.11}$$

with $R = |\boldsymbol{r} - \boldsymbol{r}'|$. The solution for the vector potential $\boldsymbol{A}$ is then

$$\boldsymbol{A} = \frac{\mu_0}{4\pi} \int_V \mathrm{d}V \, \frac{\boldsymbol{j}_p(\boldsymbol{r}')\mathrm{e}^{\mathrm{i}(\omega t - kR)}}{R}. \tag{2.12}$$

The propagation effect, i. e. the time required for source changes to propagate to each field point, is represented by the phase delay factor e^{-ikR}. With the Taylor series of this factor,

$$\mathrm{e}^{-\mathrm{i}kR} = 1 - \mathrm{i}kR - \frac{(kR)^2}{2!} + \mathrm{i}\frac{(kR)^3}{3!} + \ldots, \tag{2.13}$$

propagation effects can be ignored, if

$$kR \ll 1, \tag{2.14}$$

because $e^{-\mathrm{i}kR}$ is then nearly constant.

The factor k can be approximated by evaluating the defining equation

$$k = (1 - \mathrm{i})\sqrt{\frac{\omega\mu_0\sigma}{2}\left(1 + \mathrm{i}\frac{\omega\varepsilon_0\varepsilon_r}{\sigma}\right)} \tag{2.15}$$

with the aforementioned numerical values, a ratio of capacitive to resistive currents of $\sqrt{2} - 1$ and a conductivity of $\sigma = 0.33$ S/m as usually used for the human brain:

$$kR \approx (1 - \mathrm{i})0.043. \tag{2.16}$$

This yields a magnitude error of about 4 % and a phase angle error of 0.043 rad (about 2.5°) for the $\mathrm{e}^{-\mathrm{i}kR}$-term, which makes propagation effects clearly negligible.

Capacitive effects

The capacitive effects relating to the complex factor $\sigma(1+\frac{\mathrm{i}\omega\varepsilon_0\varepsilon_r}{\sigma})$ can be neglected if the capacitive currents are much smaller than the resistive currents, i. e. if

$$\frac{\omega\varepsilon_0\varepsilon_r}{\sigma} \ll 1. \tag{2.17}$$

The maximal value for this ratio in Table 2.1 is 0.32, which satisfies (2.17) reasonably good. Therefore also capacitive effects are negligible for bioelectric problems.

Inductive effects

When comparing the electric field component arising from magnetic induction to the electric field due to the electric potential, the inductive effects can be neglected if the ratio of both is sufficiently small:

$$\frac{|\mathrm{i}\omega \boldsymbol{A}|}{|\nabla\phi|} \ll 1. \tag{2.18}$$

This relation is satisfied, as $\frac{|\mathrm{i}\omega \boldsymbol{A}|}{|\nabla\phi|} = |kR|^2$, and $|kR|^2 \ll 1$ as can be seen from (2.14). Thus, if propagation effects can be neglected, also inductive effects are insignificant.

Quasi-static Approximation

Ignoring the dynamic effects in (2.10) leads to the so-called *quasi-static approximation* of the Maxwell equations for the electric potential ϕ:

$$\nabla\cdot(\sigma\nabla\phi) = \nabla\cdot \boldsymbol{j}_p. \tag{2.19}$$

The vector potential $\boldsymbol{A}$ can then be calculated using Biot-Savart's Law:

$$\boldsymbol{A}(\boldsymbol{r},t) = \frac{\mu_0}{4\pi}\int_V \mathrm{d}r'\,\frac{\boldsymbol{j}_p(\boldsymbol{r}',t)}{R} - \frac{\mu_0}{4\pi}\int_V \mathrm{d}r'\,\frac{\sigma\nabla\phi(\boldsymbol{r}',t)}{R}. \tag{2.20}$$

To complete the mathematical problem description the following boundary conditions are stated. At the interfaces Γ between different compartments Neumann boundary conditions apply:

$$(\sigma_1\nabla\phi_1)\cdot\boldsymbol{n} = (\sigma_2\nabla\phi_2)\cdot\boldsymbol{n} \qquad \text{on } \Gamma, \tag{2.21}$$

where $\boldsymbol{n}$ is the normal vector on Γ, whereas on the surface of the base domain the normal component must vanish:

$$(\sigma\nabla\phi)\cdot\boldsymbol{n} = 0 \qquad \text{on } \Gamma = \partial\Omega. \tag{2.22}$$

Furthermore the value of the electric potential must be set to a specific value at one reference point:

$$\phi(\boldsymbol{r}_{\mathrm{ref}}) \equiv 0. \tag{2.23}$$

2.2.1 The Mathematical Current Dipole

A common concept for modeling the primary current distribution $\boldsymbol{j}_p$ on the right hand side of (2.19) is the mathematical current dipole

$$\boldsymbol{j}_p(\boldsymbol{r}) = \boldsymbol{M}\cdot\delta(\boldsymbol{r}-\boldsymbol{r}'). \tag{2.24}$$

It is the abstraction of two discrete electrical monopoles (a source and a sink) with the charge Q and the distance $\boldsymbol{l}$ that come infinitely close together in $\boldsymbol{r}'$, while the dipole moment $\boldsymbol{M} = Q \cdot \boldsymbol{l}$ is constant and finite:

$$\boldsymbol{j}_p = \lim_{\substack{Q \to \infty \\ \|\boldsymbol{l}\| \to 0}} Q \cdot \boldsymbol{l}. \tag{2.25}$$

The Dirac delta distribution in (2.24) is a very strong inhomogeneity that leads to problems in numerical calculations using the mathematical current dipole as source model. There exist several methods to deal with this inhomogeneity that are discussed in Section 2.5.

2.3 Analytical Solutions

For special geometries the partial differential equation (2.19) can be solved analytically. Especially for multilayer sphere models consisting of several concentric spheres of different conductivities a variety of analytical solutions exist, that can be computed easily, which is why they are used widely in source analysis.

The series expansion formula for the electric potential of a mathematical dipole in a multilayer sphere model used in this thesis was derived by de Munck and Peters[13, 14]. It is able to treat an arbitrary number of layers with radii $r_s < r_{s-1} < \cdots < r_1$ and constant radial and tangential conductivities $\sigma^{\text{rad}}, \sigma^{\text{tang}}$ within. It is therefore also possible to model an anisotropic skull layer with de Munck's formula, as recent measurements showed that the human skull has an anisotropic conductivity[15].

The spherical harmonics expansion for the mathematical dipole is expressed in terms of the gradient of the monopole potential to the source point. Using an asymptotic approximation and an addition-subtraction method to speed up the series convergence yields

$$\phi_{\texttt{ana}}(x_0, x_e) = \frac{1}{4\pi}\langle \mathbf{M}, S_0 \frac{x_e}{r_e} + (S_1 - \cos\omega_{0e} S_0)\frac{x_0}{r_0}\rangle \tag{2.26}$$

with ω_{0e} the angular distance between the source at x_0 and the electrode at x_e, and with

$$S_0 = \frac{F_0}{r_0} \frac{\Lambda}{(1 - 2\Lambda\cos\omega_{0e} + \Lambda^2)^{3/2}} + \frac{1}{r_0}\sum_{n=1}^{\infty} \{(2n+1)R_n(r_0, r_e) - F_0\Lambda^n\} P_n'(\cos\omega_{0e}) \tag{2.27}$$

and

$$S_1 = F_1 \frac{\Lambda\cos\omega_{0e} - \Lambda^2}{(1 - 2\Lambda\cos\omega_{0e} + \Lambda^2)^{3/2}} + \sum_{n=1}^{\infty} \left\{(2n+1)R_n'(r_0, r_e) - F_1 n\Lambda^n\right\} P_n(\cos\omega_{0e}). \tag{2.28}$$

The coefficients R_n and their derivatives, R_n', are computed analytically and the derivative of the Legendre polynomials, P_n, are determined by means of a recursion formula. The derivation of the above series of differences and the definition of F_0, F_1 and Λ can be found in [14].

In later chapters this analytical solution is used as a reference, against which the numerical solutions are compared.

2.4 The Finite Element Method

The method of choice to numerically solve (2.19) in this thesis is the finite element method (FEM, [16]), as it is able to treat arbitrary complex geometries and even anisotropic conductivities σ. It is also widely used in various scientific or engineering fields such as fluid dynamics, heat transfer problems or crash simulations in automotive engineering.

As a first step in solving a differential equation using FEM the base domain must be discretized into small regions, the so-called *elements*. In two dimensions these are often triangular or rectangular, in three dimensions often tetrahedra or cubes are used. This decomposition of the whole head domain into small elements is called *triangulation*. Effective strategies to create quality tetrahedral triangulations are discussed in Section 3.1.

For the electric potential appropriate ansatz functions in the elements have to be chosen. Usually low order polynomials are used here. For the tetrahedral elements in this thesis the linear ansatz

$$^{(e)}\phi^h(x,y,z) = c_1 + c_2 x + c_3 y + c_4 z \tag{2.29}$$

was used.

As the electric potential is continuous throughout the head domain also its approximation has to be continuous from one element to the other. This continuity condition can be fulfilled more easily when turning from element based ansatz functions $^{(e)}\phi^h$ to node based *form functions* $^{(e)}\psi_k$:

$$^{(e)}\phi^h(x,y,z) = \sum_{k}^{n} {}^{(e)}u_k \, {}^{(e)}\psi_k(x,y,z). \tag{2.30}$$

The $^{(e)}u_k$ in (2.30) are called *node variables*, whereas n is the number of nodes in an element. As this relation has to be fulfilled for every value combination of node variables, the form functions $^{(e)}\psi_k$ have to meet the Lagrange condition

$$^{(e)}\psi_k(x_j) = \delta_{jk}, \tag{2.31}$$

i. e. for every node x_j of the element it holds, that

$$^{(e)}\psi_k(x_j) = \begin{cases} 1 & \text{if } j = k, \\ 0 & \text{if } j \neq k \end{cases}. \tag{2.32}$$

The potential approximation for the whole domain is then constructed piecewise from the elements' ansatz functions. As already mentioned the use of node based form functions is of advantage. In order to compose these *global form functions* ψ_k, all nodes of the triangulation have to be numbered consecutively. Then the global form functions ψ_k are constructed from all the local form functions $^{(e)}\psi_k$ that have the value 1 at node k.

Due to this construction approach the function ψ_k is only non-zero in such elements the node k is part of. With this notation the equation for the electric potential becomes

$$\phi^h(x,y,z) = \sum_{k=1}^{N} u_k \psi_k(x,y,z). \tag{2.33}$$

Next this ansatz (2.33) is inserted into the differential equation (2.19). As the solution for an arbitrary choice of node variables will in general not be exact, a residuum R remains:

$$R(x,y,z) = \sum_{k=1}^{N} u_k \, \nabla \cdot (\sigma \nabla \psi_k) - \nabla \cdot \boldsymbol{j}_p. \tag{2.34}$$

Applying the method of *weighted residues* this residuum is weighted with weighting functions w_j. Now the node variables u_k are chosen in such a way, that the integral of the weighted residuum over the whole domain vanishes:

$$\int_{\Omega} \mathrm{d}\Omega \, R(x,y,z) w_j \overset{!}{=} 0. \tag{2.35}$$

Following Galerkin's method these weighting functions w_j are chosen equal to the form functions ψ_j, $w_j = \psi_j$. Inserting this into (2.34) and applying integration by parts yields

$$\sum_{k=1}^{N} u_k \underbrace{\int_{\Omega} \mathrm{d}\Omega \, \sigma \nabla \psi_k \cdot \nabla \psi_j}_{=:K_{jk}} + \underbrace{\int_{\Omega} \mathrm{d}\Omega \, \psi_j \, \nabla \cdot \boldsymbol{j}_p}_{=:-J_j} = 0. \tag{2.36}$$

The occurring surface integral is zero because of the boundary conditions on the surface of the base domain (2.22).

With these definitions for $\boldsymbol{K}$ and $\boldsymbol{J}$ (2.36) can be rewritten as a matrix equation:

$$\boldsymbol{K} \boldsymbol{u} = \boldsymbol{J}. \tag{2.37}$$

The matrix $\boldsymbol{K}$ is usually called the *stiffness matrix.* The task is now to solve (2.37) for the electric potential $\boldsymbol{u}$ at the nodes of the finite element mesh. To efficiently calculate the solution a fast and accurate algebraic multigrid pre-conditioned conjugate gradient method (AMG-CG)[17] was used. A direct inversion of $\boldsymbol{K}$ is usually not feasible due to the large size. Instead, the sparseness of $\boldsymbol{K}$ is exploited.

As the ansatz function ψ_k is only non-zero in elements the node k belongs to, the integrand in $\boldsymbol{K}$ is only non-zero, if j and k belong to the same element. Therefore, every row of $\boldsymbol{K}$ has only as many non-zero entries as a node has neighbors. Furthermore the stiffness matrix is symmetric, which makes it easy to store in memory on normal desktop computers even for hundreds of thousands of elements. For the FE calculations in this thesis a desktop computer with a 2.0 GHz CPU and 2 GB RAM was used to solve the equation systems.

2.5 Dipole Modeling Strategies

There exist several methods to numerically treat the singularity, that appears on the right hand side of (2.19) when the mathematical dipole (2.24) is used as a source model. The use of *Venant's Law* and a mathematically more sound *subtraction approach* are discussed in this section. Both approaches are implemented in the IP-NeuroFEM-Toolbox [18] that was used for all forward and inverse computations for this thesis.

2.5.1 Venant Principle

The principle of Saint Venant known from mechanics states, that for the measured signal at the electrodes far away from the source it is not important how in detail the current dipole is modeled.

Therefore the mathematical dipole can be approximated by monopoles that are distributed on the neighboring FE nodes and adjusted in strength. To find the appropriate mesh nodes at first the node closest to the source position is determined, then the monopole sources and sinks are distributed on all the neighbors of this node. The mathematical procedure to determine the monopole source strengths is covered in detail in [19].

In a nutshell the normalized resultant moments of order n_0 in the direction $\boldsymbol{r}$ at node i are calculated from the nodal loads J_k as

$$ {}^{n_0}M_i^r = \left(\frac{\Delta x_{ki}^r}{a_{\text{ref}}} \right)^{n_0} \cdot J_k, \tag{2.38} $$

in which Δx_{ki}^r means the r-component of the vector between node i and the source node k and a_{ref} denotes a reference length, that ensures the convergence to 0 of the series $\left(\frac{\Delta x_{ki}^r}{a_{\text{ref}}} \right)^{n_0} \cdot J_k$ for $n_0 \to \infty$.

2.5.2 Subtraction Approach

Another feasible approach to treat the mathematical dipole singularity is the *subtraction approach*[20, 21]. In order to eliminate the singularity from the partial differential equation (2.19) the electric potential ϕ and the conductivity σ are split up:

$$ \phi = \phi^{\infty} + \phi^{\text{corr}} \tag{2.39} $$

$$ \sigma = \sigma^{\infty} + \sigma^{\text{corr}}. \tag{2.40} $$

In a small non-empty area around the source position the conductivity σ^{∞} is assumed to be constant and σ^{corr} is zero in this region. The singularity potential ϕ^{∞} deals with the inhomogeneity at the source position x_0, as it is defined as the solution for a dipole in an infinite homogeneous conductor with constant conductivity σ^{∞}, which is governed by the Poisson equation

$$ \Delta \phi^{\infty} = \frac{\nabla \cdot \boldsymbol{j}_p}{\sigma^{\infty}}. \tag{2.41} $$

The solution of (2.41) can be formed analytically as

$$ \phi^{\infty}(x) = \frac{1}{4\pi\sigma^{\infty}} \frac{\langle \boldsymbol{M}, (x - x_0) \rangle}{|x - x_0|^3}. \tag{2.42} $$

For a homogeneous and anisotropic conductivity σ^{∞} (2.42) becomes

$$ \phi^{\infty}(x) = \frac{1}{4\pi\sqrt{\det \sigma^{\infty}}} \frac{\langle \boldsymbol{M}, (\sigma^{\infty})^{-1}(x - x_0) \rangle}{\langle (\sigma^{\infty})^{-1}(x - x_0), x - x_0 \rangle^{3/2}}. \tag{2.43} $$

As the singularity potential ϕ^{∞} describes the potential in an unbounded volume conductor, the correction potential ϕ^{corr} has to be computed to correct the potential with respect to the realistic volume conductor.

Inserting (2.39) and (2.40) into (2.19) and using (2.41) yields a Poisson equation for the correction potential

$$\nabla \cdot (\sigma \nabla \phi^{\mathrm{corr}}) = -\nabla \cdot (\sigma^{\mathrm{corr}} \nabla \phi^{\infty}) \qquad \text{in } \Omega \tag{2.44a}$$

with inhomogeneous Neumann boundary conditions

$$(\sigma \nabla \phi^{\mathrm{corr}}) \cdot \boldsymbol{n} = -\left(\sigma \nabla \phi^{\infty}\right) \cdot \boldsymbol{n} \qquad \text{on } \Gamma = \partial\Omega. \tag{2.44b}$$

In (2.44) the right-hand side is now singularity-free because of the homogeneity condition:

$$\sigma^{\mathrm{corr}} = \sigma^{\infty} - \sigma = 0 \quad \text{in } \Omega. \tag{2.45}$$

To numerically solve (2.44) a FEM ansatz as derived in Section 2.4 is employed using Galerkin's method which leads to the matrix equation

$$\boldsymbol{K} \cdot \boldsymbol{u}^{\mathrm{corr}} = \boldsymbol{J}^{\mathrm{corr}}, \tag{2.46}$$

where $\boldsymbol{K}$ is the stiffness matrix, $\boldsymbol{u}^{\mathrm{corr}}$ the numerically calculated correction potential vector and the right hand side vector $\boldsymbol{J}^{\mathrm{corr}}$ stands for

$$\boldsymbol{J}^{\mathrm{corr}} = -\int_{\Omega} \mathrm{d}\Omega \; ((\sigma - \sigma^{\infty}) \nabla \phi^{\infty}) \cdot \nabla \psi_i - \int_{\Gamma = \partial\Omega} \mathrm{d}\Gamma \, \sigma^{\infty} \psi_i \, \boldsymbol{n} \cdot \nabla \phi^{\infty}. \tag{2.47}$$

The node based global ansatz functions ψ_i are explained in Section 2.4.

To calculate the total electric potential first the singularity potential ϕ^{∞} is evaluated using (2.43). Then the correction potential is computed by solving the equation system (2.46). Finally the total electric potential is constructed using (2.39).

In [21] a theoretical reasoning is given alongside with a validation in a four-layer sphere model with anisotropic skull compartment for the fact, that second order Gaussian integration is necessary and sufficient for the right-hand side integration in (2.47). This implementation of the full subtraction approach is in an order of magnitude more accurate than the *projected subtraction approach* suggested in [20], where the singularity potential ϕ^{∞} is projected into the finite element space and approximated by linear ansatz functions.

2.6 Transfer Matrix Approach

For the solution of the inverse problem it is necessary to compute a forward solution many times for different dipole positions. If each time an equation system like (2.37) had to be solved this process would require too much computation time. So instead of computing the potential every time for each node of the tetrahedra mesh the law of matrix multiplication associativity is exploited in order to cut down the necessary computational effort.

As one is usually only interested in the simulated potential at the measurement sensors, a restriction matrix $\boldsymbol{R}$ is applied, that maps the large potential vector $\boldsymbol{u}$ onto the FE nodes corresponding to the measurement electrodes (if the electrodes are not part of the FE mesh interpolation is required):

$$\boldsymbol{u}_{\mathrm{EEG}} = \boldsymbol{R} \cdot \boldsymbol{u}. \tag{2.48}$$

For s electrodes and a mesh with n FE nodes $\boldsymbol{R}$ is a $(s-1) \times n$ matrix (the potential at the reference electrode is fixed, so it does not need to be calculated) with $R_{ij} = 1$ if electrode i is mapped to FE node j and $R_{ij} = 0$ else.

Although the stiffness matrix $\boldsymbol{K}$ practically cannot be directly inverted because of its sparseness and size, it can be done formally and thus $\boldsymbol{u}$ can be rewritten using (2.37). Using the law of associativity then yields

$$\boldsymbol{u}_{\mathrm{EEG}} = \boldsymbol{R}\left(\boldsymbol{K}^{-1}\boldsymbol{J}\right) = \left(\boldsymbol{R}\boldsymbol{K}^{-1}\right)\boldsymbol{J} = \boldsymbol{T}\boldsymbol{J}. \tag{2.49}$$

The matrix $\boldsymbol{T}$ is called *transfer matrix*. If $\boldsymbol{T}$ is known a forward calculation for the measurement electrodes reduces to a simple matrix multiplication. To calculate the transfer matrix its definition $\boldsymbol{T} = \boldsymbol{R}\boldsymbol{K}^{-1}$ is multiplied from the right side with the stiffness matrix $\boldsymbol{K}$ and transposed ($\boldsymbol{K} = \boldsymbol{K}^t$ as $\boldsymbol{K}$ is symmetric):

$$\boldsymbol{K}\,\boldsymbol{T}^t = \boldsymbol{R}^t \tag{2.50}$$

By solving (2.50) $(s-1)$ times for the column vectors of $\boldsymbol{R}^t$ the transfer matrix $\boldsymbol{T}$ can be computed.

2.7 Inverse Methods

The reconstruction of the underlying source distribution from a measured EEG dataset is called the *inverse problem*. There exist many different algorithms for the solution of the inverse problem such as the minimum norm solution, the goal function scan or the dipole fit, which was used in this thesis and shall be briefly discussed in the next section.

2.7.1 Dipole Fit

The dipole fit is a method to determine a configuration of discrete current dipoles that will generate a given field pattern at the m measurement sensors. After having chosen an appropriate number n of active dipoles from a-priori knowledge the remaining parameters location, orientation and magnitude of each dipole have to be determined.

First, the non-linear location parameters $\boldsymbol{q}$ are determined. The linear parameters orientation and magnitude are then to be calculated, such that the difference between measured and simulated data is minimized.

To find the linear parameters from a given set $\boldsymbol{q}$ of location parameters the lead field matrix $\boldsymbol{L}_q \in \mathbb{R}^{3n \times m}$ has to be calculated, whose columns are formed by the simulated electric potential at the measurement sensors of three unit strength dipoles in orthogonal directions. With this lead field matrix a forward calculation of the simulated potential $\boldsymbol{u}_{\mathrm{sim}}$ for an arbitrary source configuration of dipoles $\boldsymbol{J}_q$ reduces to a simple matrix multiplication:

$$\boldsymbol{u}_{\mathrm{sim}} = \boldsymbol{L}_q \boldsymbol{J}_q \tag{2.51}$$

Now the goal function $H(\boldsymbol{q})$ can be formulated, which is to be minimized.

$$H(\boldsymbol{q}) := \|\boldsymbol{L}_q \boldsymbol{J}_q - u_{\mathrm{meas}}\| \overset{!}{=} \min \tag{2.52}$$

The linear parameters can now be determined e. g. by a singular value decomposition (SVD) of (2.52).

For the calculation of the nonlinear parameters $\boldsymbol{q}$ a downhill simplex optimizer[22] can be used, that determines a local minimum of the goal function. Therefore the goal function is evaluated at a set of vertices $\boldsymbol{q}_i = (\boldsymbol{q}_0, \ldots, \boldsymbol{q}_n)$, that form a simplex in the parameter space. The worst point with the highest goal function value is then replaced with a point reflected through the barycenter of the remaining points, thus moving the simplex through the parameter space. So if a minimum is found, the simplex will contract around it. The procedure is stopped when a certain stop criterion is met, such as the maximal number of iterations or the goal function's absolute value gets below a certain upper bound.

In order to avoid the optimization process getting stuck in local minima of the goal function, it has to be repeated for different initial parameter sets $\boldsymbol{q}_i$.

3 Tetrahedral Mesh Generation for Multilayer Sphere Studies

The application of the FEM on the bioelectric forward problem is studied in this chapter on the basis of multilayer sphere models. As the human head is spherical in a first approximation it can be modeled as concentric spheres of different conductivities. Section 3.1 deals with the generation of the volume conductor models which are used for forward calculations in Section 3.6.

3.1 Mesh Generation

To generate the tetrahedra models for this thesis the software TetGen[23] was used, which utilizes a *Constrained Delaunay Tetrahedralization (CDT)* approach based on a flipping algorithm[24].

A CDT[25] is a variation of a Delaunay triangulation discussed in the following section that always respects a given boundary[26, 27]. It is therefore suitable to create high-quality volume conductor models for numerical calculations. As there even exist polyhedra that cannot be tetrahedralized without adding additional points[28, 29], various point insertion approaches to generate a CDT were suggested[27, 30, 31].

TetGen uses an approach discussed in [32] and relies on the adaptive exact arithmetic predicates by Shewchuk[33] to perform geometrical operations like insphere or orientation tests.

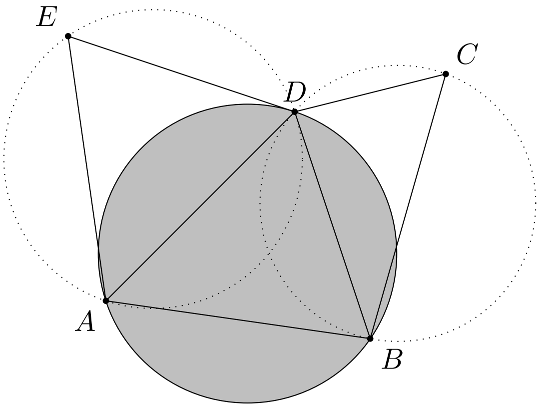

Figure 3.1: A Delaunay Triangulation of five points in two dimensions

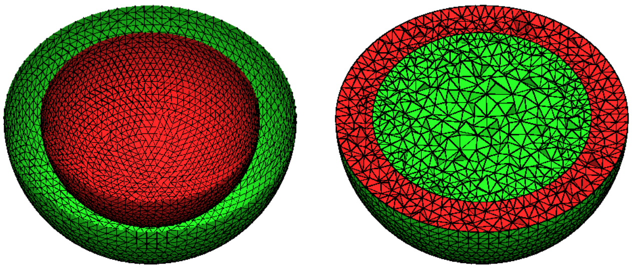

(a) Triangulated surfaces (b) Final tetrahedra mesh

Figure 3.2: Meshing procedure: From triangulated surfaces to the final volume conductor

3.1.1 Delaunay Triangulation

The Delaunay Triangulation[34] of a given vertex set V is a triangulation such that no vertex of V lies inside the circumsphere of any simplex s forming the triangulation. For the two-dimensional case a suitable Delaunay Triangulation of a five point set is shown in Figure 3.1.

The Delaunay triangulation has many optimal properties making it a good starting point for the generation of meshes used in numerical calculations. For example, it maximizes the minimum angle of the simplices while also minimizing the maximal circumradii for a point set in $\mathbb{R}^2$, therefore avoiding the creation of elements that are numerically complicated to treat. An overview with further discussion can be found in [35].

There exist several reasonably fast algorithms to generate a Delaunay Triangulation such as flipping methods[36], a divide-and-conquer approach or incremental strategies.

3.1.2 Meshing Procedure

The final meshing procedure using the aforementioned CDT approach starts with the creation of suitable boundary surfaces that describe the different compartments of the model.

Sphere Models

In the case of multilayer sphere models concentric spheres with different radii (see Figure 3.2(a)) are used. By spreading nodes equidistantly on a sphere surface a triangular discretization is obtained, that approximates the sphere more or less roughly depending on the mean vertex distance. The more vertices are on each shell from the beginning the finer will the created tetrahedra mesh be, because TetGen tries to incorporate every point on the surface into the volume mesh.

Usually three or four compartments are chosen representing the skin, the skull and the brain, which can additionally be split into CSF and brain layer. Latest studies plan to use even more shells, e. g. by considering the skull as being three-layered (with the anatomically more correct separation into osseous compacta and the inbetween spongiosa) or differentiating between gray and white matter in the brain compartment.

After having setup the different surfaces the CDT approach can be used to generate a tetrahedralization conforming to the surface meshes. First a Delaunay triangulation is built from the surface vertices. Then a local degeneracy removal algorithm is applied, which combines vertex perturbation and insertion to result in a new set of vertices which includes the input set. From this set the final CDT (Figure 3.2(b)) is constructed using a fast facet recovery method.

With TetGen it is also possible to apply various constraints to the shape and size of the tetrahedra in order to increase the mesh quality and thus the numerical accuracy of FEM calculations. The first constraint concerns the quality of the generated tetrahedra. For a tetrahedron t with a circumsphere radius R and a shortest edge length L the *radius-edge ratio* Q can be defined as

$$Q := \frac{R}{L}. \tag{3.1}$$

This ratio is large ($Q > 2$) for most badly shaped tetrahedra and small ($Q < 1$) for the best-shaped ones. The minimal value of $\sqrt{6}/4 \approx 0.612$ is reached for the regular tetrahedron. However there is a special, nearly degenerate type of tetrahedra that undermines this quality measure and that must be accounted for: the so-called *sliver* is very flat and can have a radius-edge ratio of as small as 0.707. Therefore additional mesh smoothing and optimization steps like local flip operations are required to remove slivers.

As a second constraint the volume of each generated tetrahedron can be confined to a certain value, so no element with a bigger volume will be created. This is useful for refining a mesh in certain regions where high accuracy is necessary.

Realistic Head Model

For a realistic head model the compartment boundaries are based on the individual subjects registered and segmented magnetic resonance (MR) images. The use of computed tomography (CT) imaging is also possible but ruled out for healthy subjects because of the inappropriate exposure to ionized radiation.

There are several methods of contrasting an MR image based on different pulse sequences. For instance, on a T1-weighted image gray matter and liquor or the boundary between skull and scalp can be easily distinguished. After recording of an image sequence the different image slices have to be aligned in order to compensate for movement artifacts and the like. The image is then partitioned into regions of similar gray values that represent the different head compartments. By discretizing the surfaces of those compartments the starting point for the CDT meshing approach as described above is reached.

It is important for the mesh generation that the generated surfaces do not intersect each other. That means that two facets may only intersect at a shared vertex, segment or a union of shared facets and vertices.

Conductivity Assignment

In order to compute a solution for the finite element equation system that results from the volume conductor every tetrahedron needs to be assigned a conductivity σ. TetGen is able to automatically assign a label to every created tetrahedron depending on the compartment it is located in. This label number then corresponds to the real conductivity value in the calculations.

The automatic label assignment procedure in TetGen loops over every tetrahedron and spreads the label value to its neighbors, until it stops at a boundary. Therefore it is able to assign different labels to each closed compartment in the model.

3.2 Multilayer Sphere Models

Using the mesh generation techniques described in Section 3.1.2 three groups of isotropic four layer sphere models with varying parameter constraints were created. These are based on the geometric properties of the underlying volume conduction model of the human head. The innermost compartment represents the brain (red in all the figures), it does not differentiate between white and gray matter. Then follow, as already mentioned in Section 3.1.2, the CSF (light green), skull (dark blue) and skin (yellow) layers.

In order to study the influence of different parameter combinations on the accuracy of the numerical result, the parameters *tetrahedra volume* and *surface triangle edge length* are evaluated in the meshes of Group 1 and 2. Meshes of Group 3 then combine the best results of the other two in order to achieve minimal error values for the subtraction approach.

3.2.1 Group 1 - Volume Constrained Meshes

On each sphere surface 2957 points were distributed which leads to mean mesh resolutions of 5.7 mm for the innermost shell up to 6.8 mm for the outmost sphere surface.

	Skin	**Skull**	**CSF**	**Brain**
Radius in mm	92.0	86.0	80.0	78.0
Conductivity in S/m	0.33	0.0042	1.79	0.33

Table 3.1: Parameters of the isotropic four layer sphere models

To evaluate the impact of constraining the tetrahedra volume to 1 mm^3 in the different head compartments a mesh with isotropic conductivity values (see Table 3.1) was generated for every combination of affected compartments. Furthermore the effect of quality meshing in the unconstrained model and a higher refinement for certain compartments was investigated. Table 3.2 shows the parametrization of all meshes that were used in the first part of the multilayer sphere studies. The cross-sections of the models with

	Constraints	**#Points**	**#Elements**
`unrefined`	-1 -1 -1 -1	29462	165578
`unrefined-q`	-1 -1 -1 -1[a]	39069	226404
`fineskin`	-1 -1 -1 5	42974	238645
`fineskull`	-1 -1 1 -1	124491	768271
`fineskull-skin`	-1 -1 5 5	58854	338385
`fineskull-skin*`	-1 -1 1 1	230538	1399786
`fineCSF`	-1 1 -1 -1	34149	191716
`fineCSF*`	-1 0.1 -1 -1	373380	2275401
`fineCSF-skin`	-1 0.8 -1 5	57820	324987
`fineCSF-skin*`	-1 0.1 -1 1	527833	3255504
`fineCSF-skull`	-1 1 1 -1	124265	766754
`fineCSF-skull-skin`	-1 1 2 2	117875	705085
`finebrain`	5 -1 -1 -1	140185	878325
`finebrain-skin`	1 -1 -1 1	696139	4403633
`finebrain-skull`	1 -1 1 -1	668407	4274257
`finebrain-skull-skin`	1 -1 1 1	773966	4901874
`finebrain-CSF`	1 1 -1 -1	578013	3696820
`finebrain-CSF-skin`	1 1 -1 1	697483	4411590
`finebrain-CSF-skull`	1 1 1 -1	667530	4268487
`fineall`	1 1 1 1	773846	4900971

Table 3.2: The parametrizations of the volume meshes used. The volume constraints are ordered from inmost compartment to outmost, i. e. from left to right brain, CSF, skull and scalp compartment

[a]: Model `unrefined-q` was meshed with a quality constraint of `q` = 1.2, see Section 3.1.2.

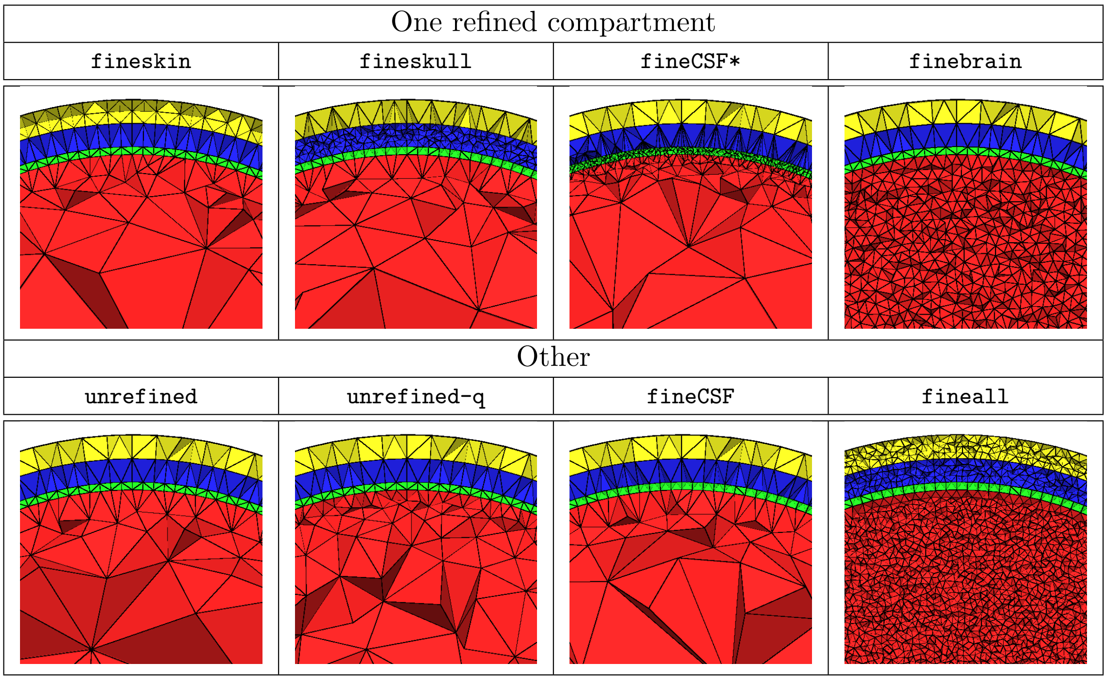

Figure 3.3: Cross-sections of some of the tetrahedral meshes with different volume constraints of Group 1

only one refined compartment as well as the unrefined ones are shown in Figure 3.3. The remaining meshes with two or more refined compartments are listed in Figure B.1 on page 96.

It is notable, that the model `fineCSF` looks quite similar to the `unrefined` one, because a volume constraint of 1 mm^3 is obviously not small enough for the very thin CSF layer. Therefore that model was not used in the further evaluation. Instead the model `fineCSF*` was created with an even tighter volume constraint of 0.1 mm^3 for the CSF compartment.

3.2.2 Group 2 - Surface Resolution Adapted Meshes

Another point of interest is the influence of the surface triangles' edge length on the accuracy of the forward solution.

Group 2a

To demonstrate the effect of increasing the spheres' surface resolution h (which will force TetGen to generate smaller tetrahedra close to the surfaces) first two models are presented with different values of h. The first model, `o11781`, had 11781 nodes on each sphere shell before meshing and resulted in a tetrahedra mesh consisting of 69602 nodes and 390677 elements. Its mean surface resolution is $h_1 = (3.1 \pm 0.4)$ mm. The same procedure with 31860 nodes on each sphere surface generated model `o31860` with 214447 nodes and 1246470 elements. It therefore has a higher surface resolution of

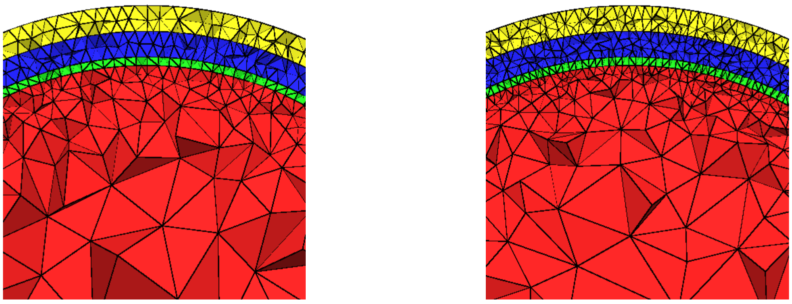
(a) The model `o11781` (b) The model `o31860`

Figure 3.4: The two meshes of Group 2a with different surface resolutions h

$h_2 = (1.9 \pm 0.3)$ mm.

Group 2b

For a more thorough analysis of the numerical error's h-dependence six other sphere meshes were generated with gradually increasing surface mesh resolutions and also without any volume constraints. The geometrical properties were again the same as before, so the outmost sphere radius is 92 mm. The final meshes' properties are shown in Table 3.3. To create the meshes with a higher sphere surface resolution the coarsest mesh was gradually refined.

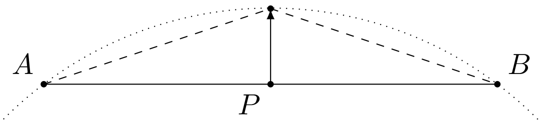

Figure 3.5: Refinement of a sphere triangulation by adding a new point P on the sphere surface instead in the middle of $\overline{AB}$

In order to keep these refined meshes as close as possible to the original ones, the idea is to add additional points to an existing mesh instead of recreating a new sphere triangulation with a finer volume constraint. Instead of just adding a new point P in the middle of $\overline{AB}$ as TetGen would do if used to refine a mesh, the new node is shifted towards the sphere surface to better approximate the curved outline. The principle is shown in Figure 3.5.

This refinement process was performed two times on a mesh with a mean surface resolution of ca. 8 mm and on another mesh with 6 mm leading to the six tetrahedra meshes listed in Table 3.3. Cross-sections of these are shown in Figure 3.6.

Another refinement series was carried out on a model with an inmost-sphere-radius of only 74 mm, so the influence of a thicker CSF layer can be studied (see Figure 3.7 and

	edge length h in mm	**#nodes**	**#elements**
8mm	8.05 ± 1.09	7500	38866
6mm	6.11 ± 0.77	13604	71045
4mm	4.01 ± 0.54	34636	188958
3mm	3.01 ± 0.38	69498	384090
2mm	2.00 ± 0.27	190126	1093263
1.5mm	1.50 ± 0.19	364691	2100452

Table 3.3: The tetrahedra meshes of the first refinement group in Group 2b

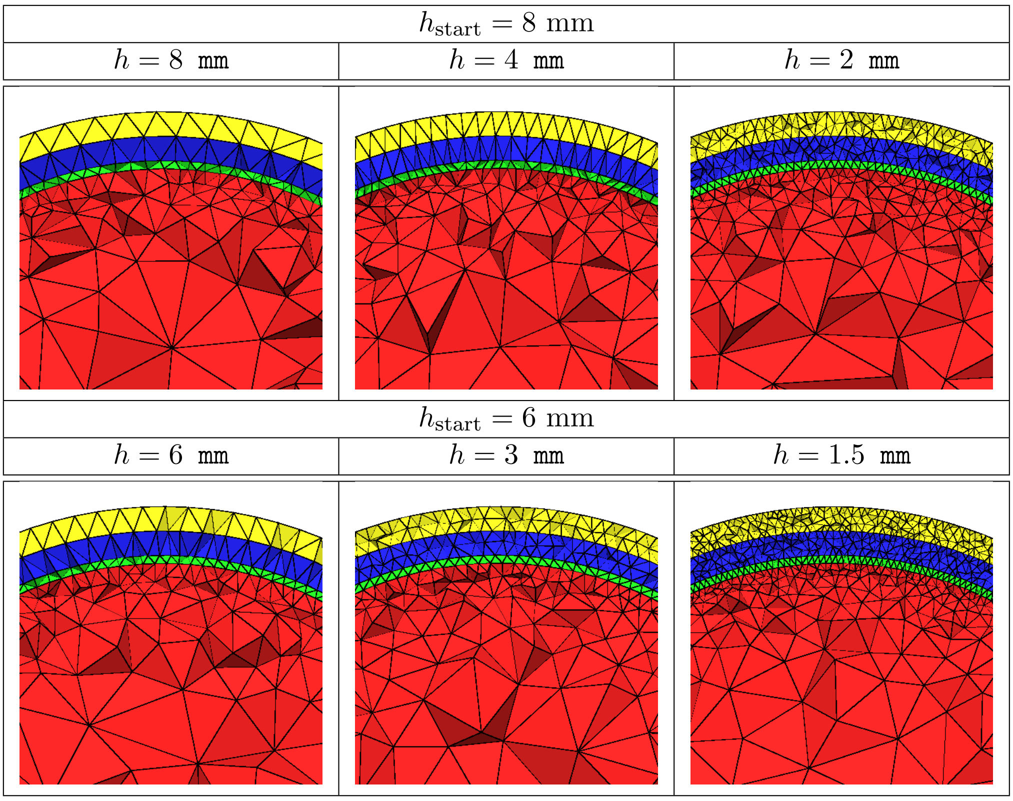

Figure 3.6: The tetrahedra meshes of the first refinement group in Group 2b

	edge length h in mm	**#nodes**	**#elements**
6mm	6.05 ± 0.76	13621	71130
3mm	2.97 ± 0.37	75855	426072
1.5mm	1.48 ± 0.19	445396	2616464

Table 3.4: Parameters for the meshes of Group 2b shown in Figure 3.7

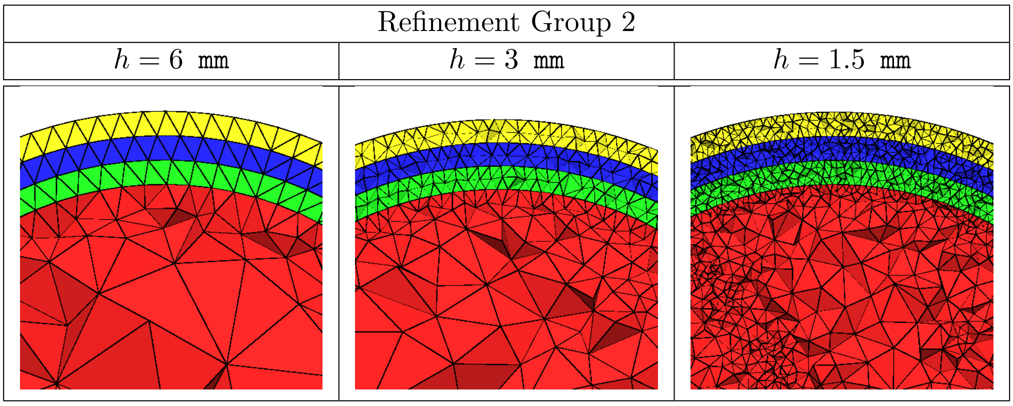

Figure 3.7: The tetrahedra meshes of the second refinement group in Group 2b. The spheres' radii were 92, 86, 80 and 74 mm

Table 3.4).

The third series of refined models were created with equally thick head compartments. The resulting models are shown in Figure 3.8 and the properties are listed in Table 3.5. Every layer in the last three models is 10 mm thick, thus not appropriately describing the human head any more.

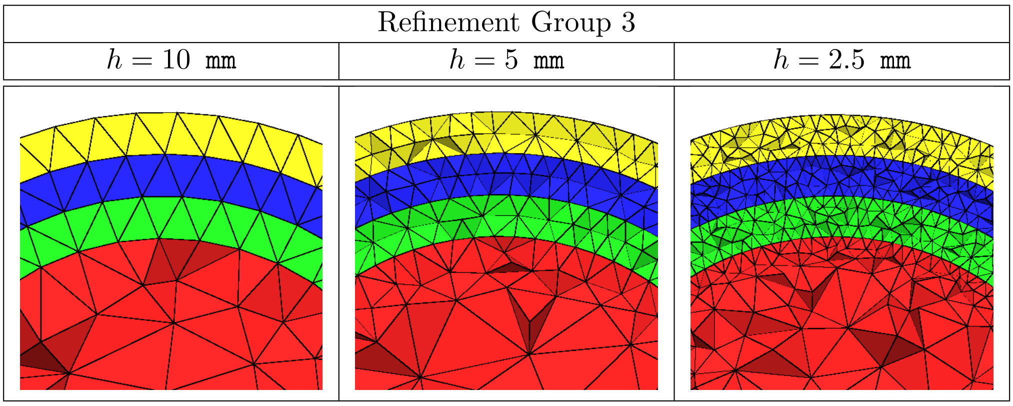

Figure 3.8: The tetrahedra meshes of the third refinement group in Group 2b. The spheres' radii were 90, 80, 70 and 60 mm

	edge length h in mm	**#nodes**	**#elements**
10mm	10.35 ± 1.30	3652	18427
5mm	5.09 ± 0.65	19984	109548
2.5mm	2.53 ± 0.32	109976	635177

Table 3.5: Parameters for the meshes of Group 2b shown in Figure 3.8

3.2.3 Group 3 - Specifically Tuned Meshes

As a last mesh group two meshes shall be presented that resulted for the first time in RDM values under 1 % for nearly all eccentricities. To achieve this good numerical quality, a high sphere surface resolution was combined with specific volume constraints to create a fine mesh with very regular tetrahedra. The first model, labeled `o11781-Skin` and displayed in cross-section in Figure 3.9(a), was constructed by distributing 11781 points on each of the four spheres which leads to a mean surface triangle edge length of 3.1 ± 0.4 mm. Meshing this model with TetGen while applying a volume constraint for the skin compartment of 1 mm^3 results in a model with 149102 nodes and 905539 tetrahedra elements.

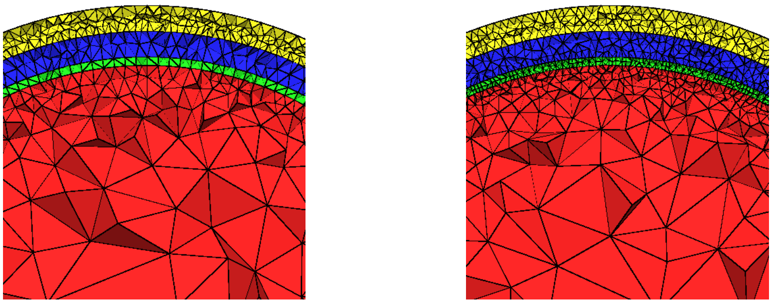

(a) The model `o11781-Skin`

(b) The model `o31860-CSF-Skin`

Figure 3.9: The two specifically for the subtraction approach designed meshes

The same procedure was used for the `o31860-CSF-Skin`-model as seen in Figure 3.9(b), only this time 31860 nodes on each shell and different volume constraints were used. The mean surface resolution before meshing was 1.9 ± 0.3 mm and not only the skin compartment but also the CSF section was volume constrained to 1 mm^3 and 0.1 mm^3 respectively. The total number of nodes after meshing was 360056 and 2165281 elements were created.

3.3 Sensor Configuration

In the multilayer sphere studies an artificial electrode cap was used containing 748 measurement points. These were distributed regularly on a sphere shell with 92 mm radius.

The sensor locations on the corresponding sphere are shown in Figure 3.10.

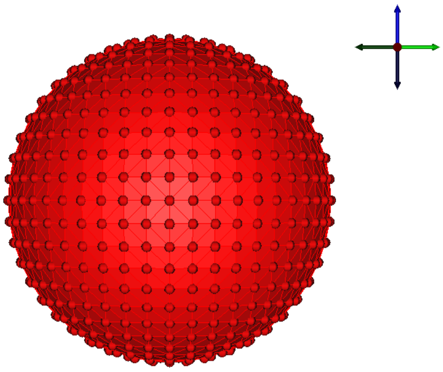

Figure 3.10: The artificial 748-electrode cap used in the multilayer sphere studies

3.4 Error Measures

To quantify the deviation between (quasi-)analytical potential Φ^{ana} and the numerical solution Φ^{num} usually three different kind of error measures are used.

The *relative error (RE)* is generally defined as

$$\text{RE} := \frac{||\Phi^{\text{num}} - \Phi^{\text{ana}}||_2}{||\Phi^{\text{ana}}||_2}. \tag{3.2}$$

where $||\cdot||_2$ denotes the L_2-norm which is defined for n sensors as

$$\|x\|_2 := \sqrt{\sum_{i=1}^{n} x_i^2}. \tag{3.3}$$

One major drawback of the RE is the fact that it does not differentiate between a topographical error and a magnitude error. To better distinguish between these two, Meijs et al.[37] introduced the *relative difference measure (RDM)*, that mirrors changes of the dipole position and orientation, and the *magnification factor (MAG)*, which indicates source strength differences. RDM and MAG are defined as follows:

$$\text{RDM} : = \left|\left| \frac{1}{||\Phi^{\text{ana}}||_2}\Phi^{\text{ana}} - \frac{1}{||\Phi^{\text{num}}||_2}\Phi^{\text{num}} \right|\right|_2 \tag{3.4}$$

$$= \sqrt{2\left(1 - \cos\angle(\Phi^{\text{ana}}; \Phi^{\text{num}})\right)} \tag{3.5}$$

$$\text{MAG} : = \frac{||\Phi^{\text{num}}||_2}{||\Phi^{\text{ana}}||_2} \tag{3.6}$$

As the RDM is therefore bounded by 0 (minimal value) and 2 (maximum) respectively, a percental value can be defined:

$$\text{RDM}(\%) := 100 \cdot \text{RDM}/2 \tag{3.7}$$

The same can be done for the MAG, whose optimal value is 1. This leads to the definition

$$\mathrm{MAG}(\%) := |1 - \mathrm{MAG}| \cdot 100 \tag{3.8}$$

3.5 Validation Platform

In order to evaluate the numerical errors of a forward simulation approach a validation platform has to be set up, by which the quality of the method can be quantified. For this purpose seventy-seven dipoles were placed inside the inmost sphere of the four layer sphere models pointing either radially outwards or in the tangential direction as shown in Figure 3.11 (only some dipoles are shown for better visualization). The dipoles have an eccentricity[1] ranging from 0 % to 99 %, as the last dipole is only 1 mm away from the conductivity jump between brain compartment and CSF layer.

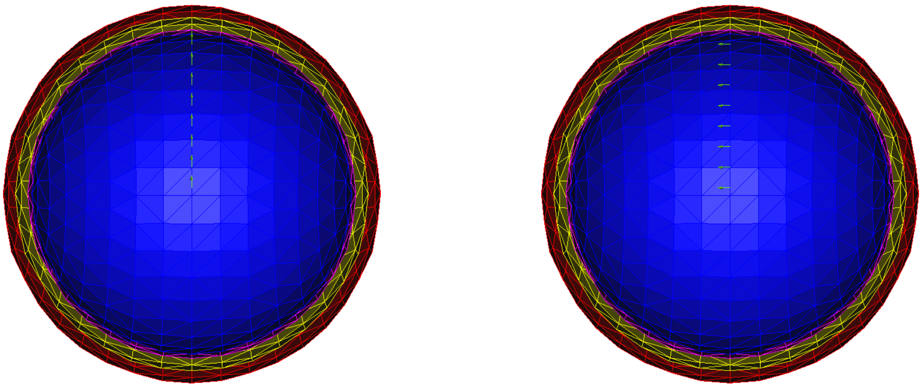

(a) Radial direction

(b) Tangential direction

Figure 3.11: Dipoles in radial (left) and tangential (right) direction placed in the spheres for validation purposes

Realistic sources in the human head however are usually located in the middle of the cortex, which is approximately 4 mm thick. Therefore the most relevant source with regard to the real situation in the head is the penultimate with a distance of 2 mm to the next compartment. The last source used in the validation procedure was therefore placed to strongly challenge the numerics. A convergence analysis for the errors and reasoning for higher values close to conductivity jumps is found in [20].

For each of these seventy-seven dipoles the forward solution can be calculated using the numerical method of choice and it can be compared with the analytical solution derived by de Munck's formula (2.26). The error between both can then be quantified by the value of the RE or further differentiated using the RDM and MAG mentioned above.

---

[1] The eccentricity is defined as the quotient of the dipole's distance to the center of the sphere and the radius of the inner shell.

3.6 Results

On the following pages the numerical errors (RDM and MAG) with regard to the analytical solution for the three mesh groups are shown. These are calculated as explained in the previous section.

As dipole model the subtraction approach (see Section 2.5.2) was used. The accuracy of the PCG-solver was set to 10^{-9}.

For Group 1 only certain models are presented, an overview of all the meshes' errors can be found in Appendix B.1.

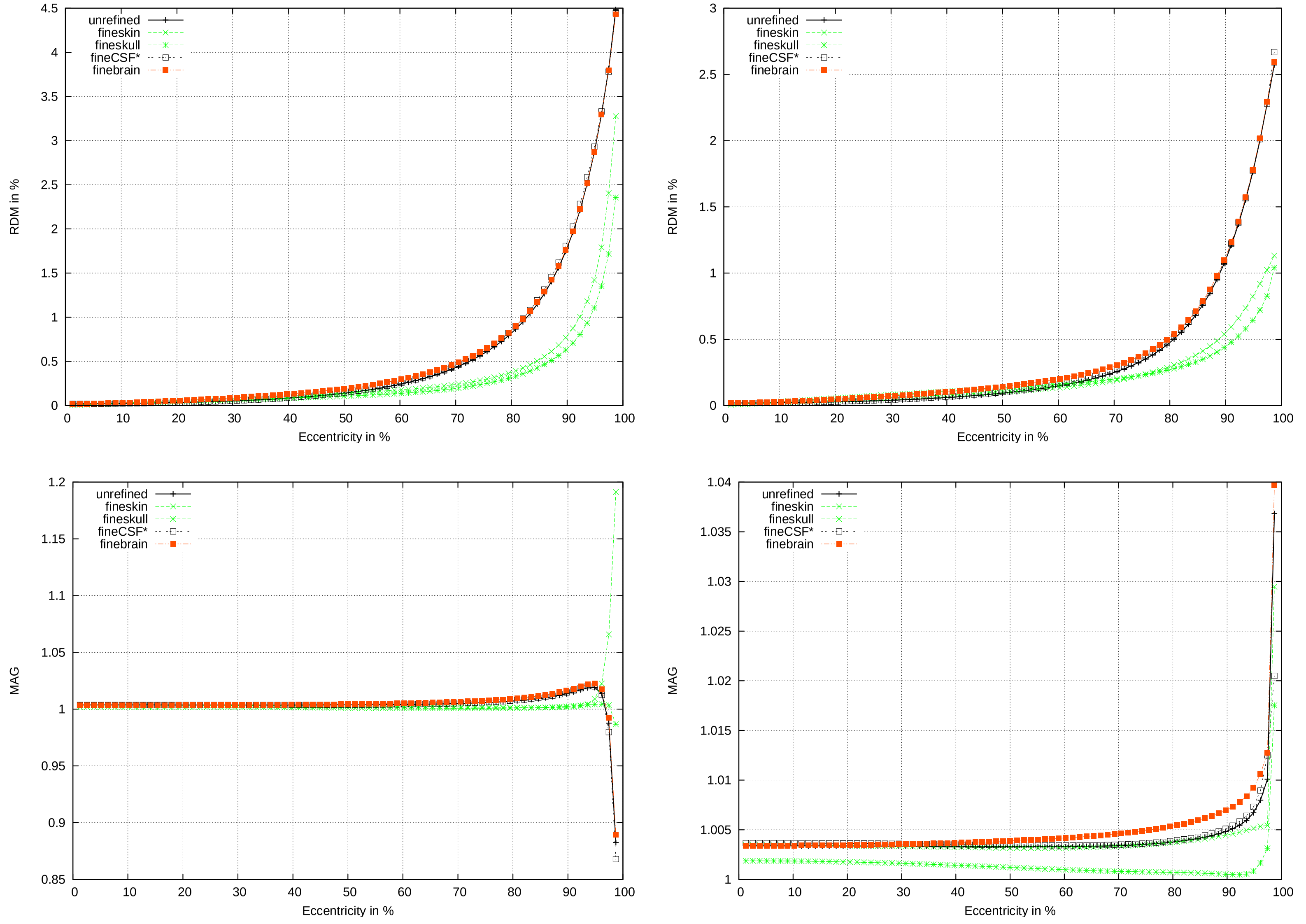

Figure 3.12: RDM (top) and MAG (bottom) for the 4 models of Group 1 with only one refined compartment (volume constraint of 1 mm^3) and the unrefined one for radial (left) and tangential (right) dipole directions

Group 1 - Volume Constrained Meshes

Figure B.2 on page 97 shows that for all models listed in Table 3.2 the RDM does not exceed a value of 5 % while the MAG stays between 0.85 and 1.2 in the worst cases.

When only one compartment is meshed with a tight volume constraint the figure on the left shows that for best numerical accuracy with the subtraction approach this compartment should be the skull. Tetrahedra with a maximal volume of one cubic millimeter produce an RDM value below 2.5 % for all eccentricities and a maximal MAG of below 1.02 in this case. The overall error in form of the RE is then below 5 %.

Table 3.6 shows the errors for the most eccentric dipole position ordered by the RE value for the radial direction.

Model	**RE** rad in %	**RDM** rad in %	**MAG** rad	**RE** tang in %	**RDM** tang in %	**MAG** tang
`fineskin`	20.418	3.27652	1.19124	3.73592	1.13187	1.02946
`fineCSF`	15.5835	4.4411	0.867951	5.7672	2.6683	1.02049
`unrefined`	14.4581	4.48384	0.882498	6.40246	2.57144	1.03683
`finebrain`	13.8677	4.42775	0.889286	6.60982	2.59129	1.0397
`fineskull`	4.86713	2.35631	0.986673	2.73551	1.04066	1.01754

Table 3.6: Errors for the most eccentric dipole in the meshes of the Group 1

If more compartments are taken into account for refinement, one can see from the zoomed Figure B.3 on Page 98 that then even RDM values of below 1.5 % are achievable. By refining brain, skull and skin or simply all compartments the RE for both directions stays below 2.1 %

So for the meshes of Group 1 that were created from pretty coarse sphere surface meshes especially constraining the tetrahedra volume of the outer compartments leads to increased numerical accuracy.

This relates to the large potential gradient of dipolar current sources close to conductivity discontinuities that cannot be approximated good enough by the finite element ansatz functions if there are just few very big elements between the source and the conductivity jump.

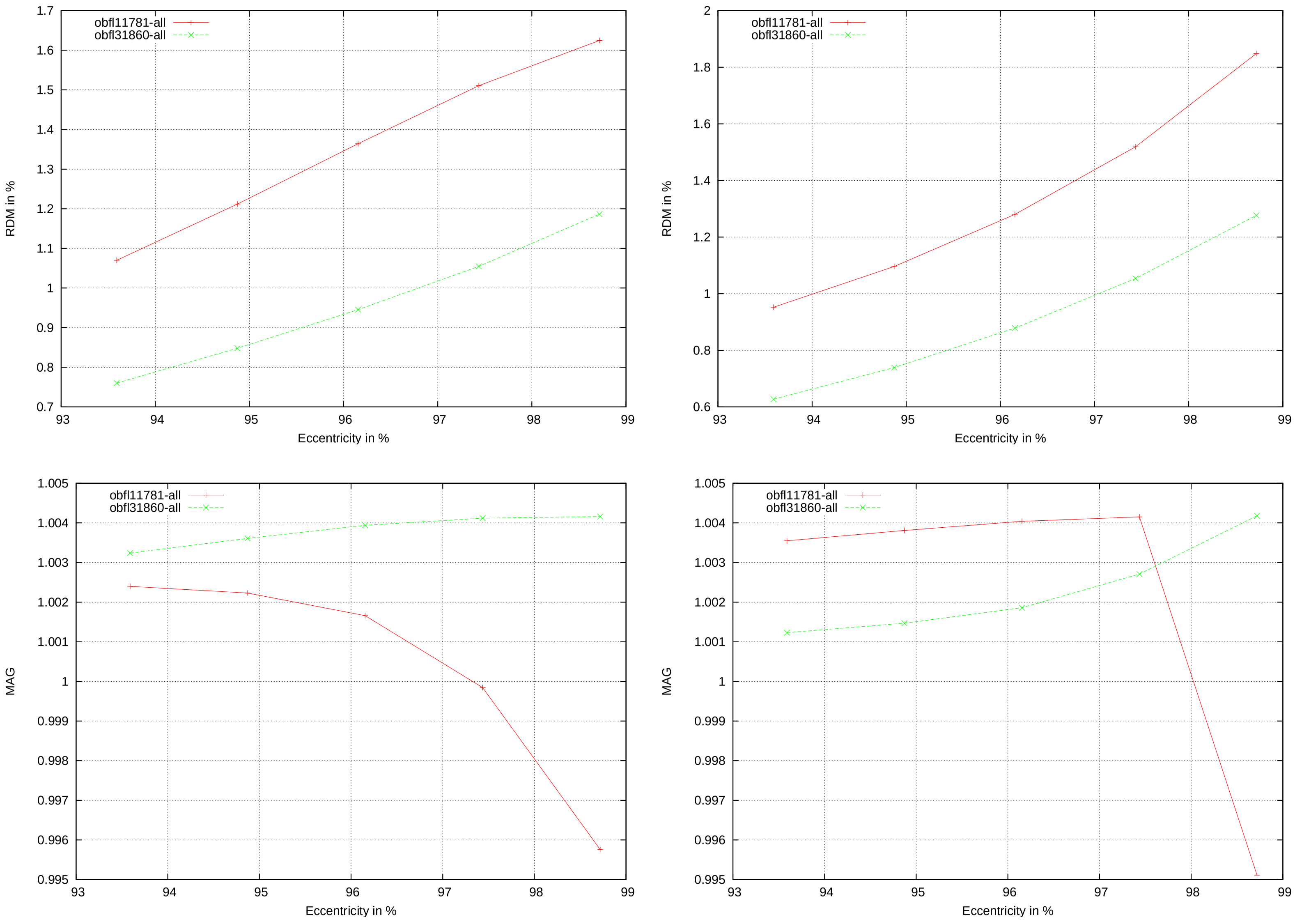

Figure 3.13: RDM (top) and MAG (bottom) for the models `obfl11781-all` and `obfl31860-all` of Group 2a for radial (left) and tangential (right) dipole directions (only the highest five eccentricities are shown)

Group 2a - Surface Resolution Adapted Meshes

The first two meshes of Group 2 show the expected decrease of the RDM values for a higher surface resolution. Whereas the coarse model's `obfl11781-all` RDM values range between 1 and 2 %, they drop to between 0.5 and 1.2 % for the finer one.

Model	**RE** rad in %	**RDM** rad in %	**MAG** rad	**RE** tang in %	**RDM** tang in %	**MAG** tang
`obfl11781-all`	3.27032	1.62479	0.995757	3.72014	1.84846	0.995111
`obfl31860-all`	2.41426	1.18658	1.00416	2.59294	1.27688	1.00418

Table 3.7: Errors for the most eccentric dipole in the meshes of the Group 2a

With the exception of the most eccentric dipole location the MAG in radial direction is better for the coarser model. Even for this outlier the relative error is below 4 %, as shown in Table 3.7.

The increase of numerical accuracy is reasonable as the subtraction approach includes the evaluation of the surface integral (2.47), which will be better approximated the higher the outer surface resolution becomes.

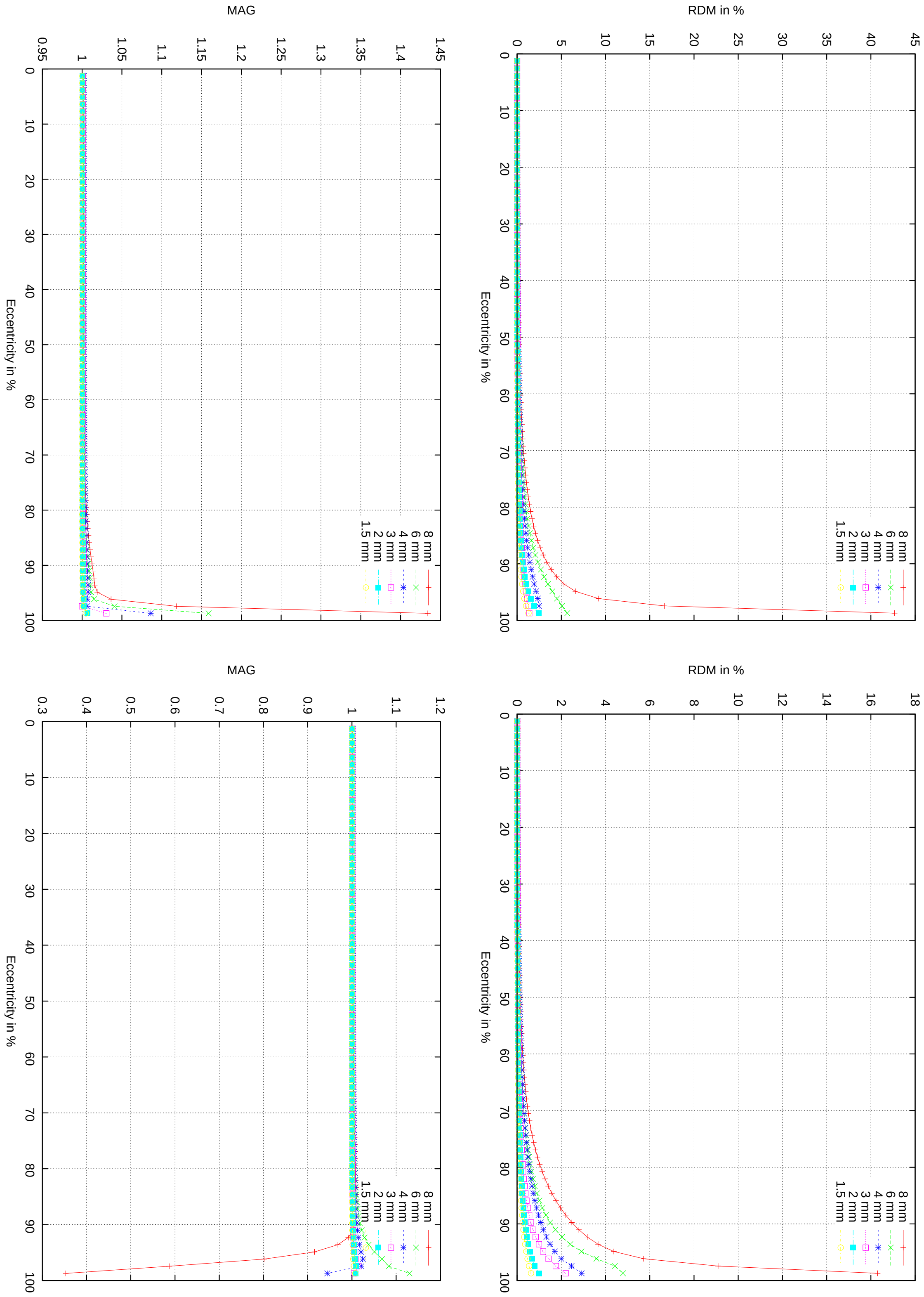

Figure 3.14: RDM (top) and MAG (bottom) for radial (left) and tangential (right) dipole orientations for the meshes of Group 2b's first refinement series with varying surface solution h

Group 2b - Surface Resolution Adapted Meshes

The gradually refined meshes show the expected error convergence for both directions in the RDM as well as in the MAG values. The biggest error in all modalities belongs to the coarsest model, while the finest mesh with $h = 1.5$ mm produces the best errors of below 1.3 % RDM for all eccentricities. The extraordinary high RDM value for the last dipole 8 mm-model probably relates to a badly shaped tetrahedron, as the errors for the other refinement groups are by far not so huge.

The highest occurring errors are listed in Table 3.8. They belong to the last source which is only one millimeter away from the conductivity jump to the CSF compartment. This relation for the relative error is also visualized in Figure 3.15.

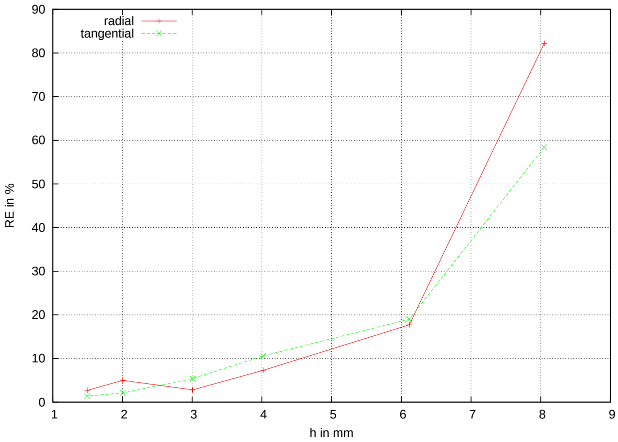

Figure 3.15: RE of the dipole with highest eccentricity of the first refinement group in Group 2b depending on the surface resolution h

As the sphere surface resolutions become gradually finer the real shape is approximated better and better. Therefore the numerical error decreases. A theoretical reasoning for this convergence towards the exact solution is given in [20].

h in mm	**RE** rad in %	**RDM** rad in %	**MAG** rad	**RE** tang in %	**RDM** tang in %	**MAG** tang
8	82.202	42.670	0.352968	58.393	16.300	1.43421
6	17.7	5.669	1.13015	18.941	4.7871	1.15892
4	7.3048	2.4348	0.944352	10.553	2.9209	1.08621
3	2.797	1.3761	1.00467	5.3989	2.1980	1.03039
2	4.9752	2.4457	1.00797	2.122	1.0054	1.00658
1.5	2.706	1.2956	1.00748	1.3505	0.63107	1.00473

Table 3.8: Errors for the most eccentric dipole in the meshes of the first refinement series of Group 2

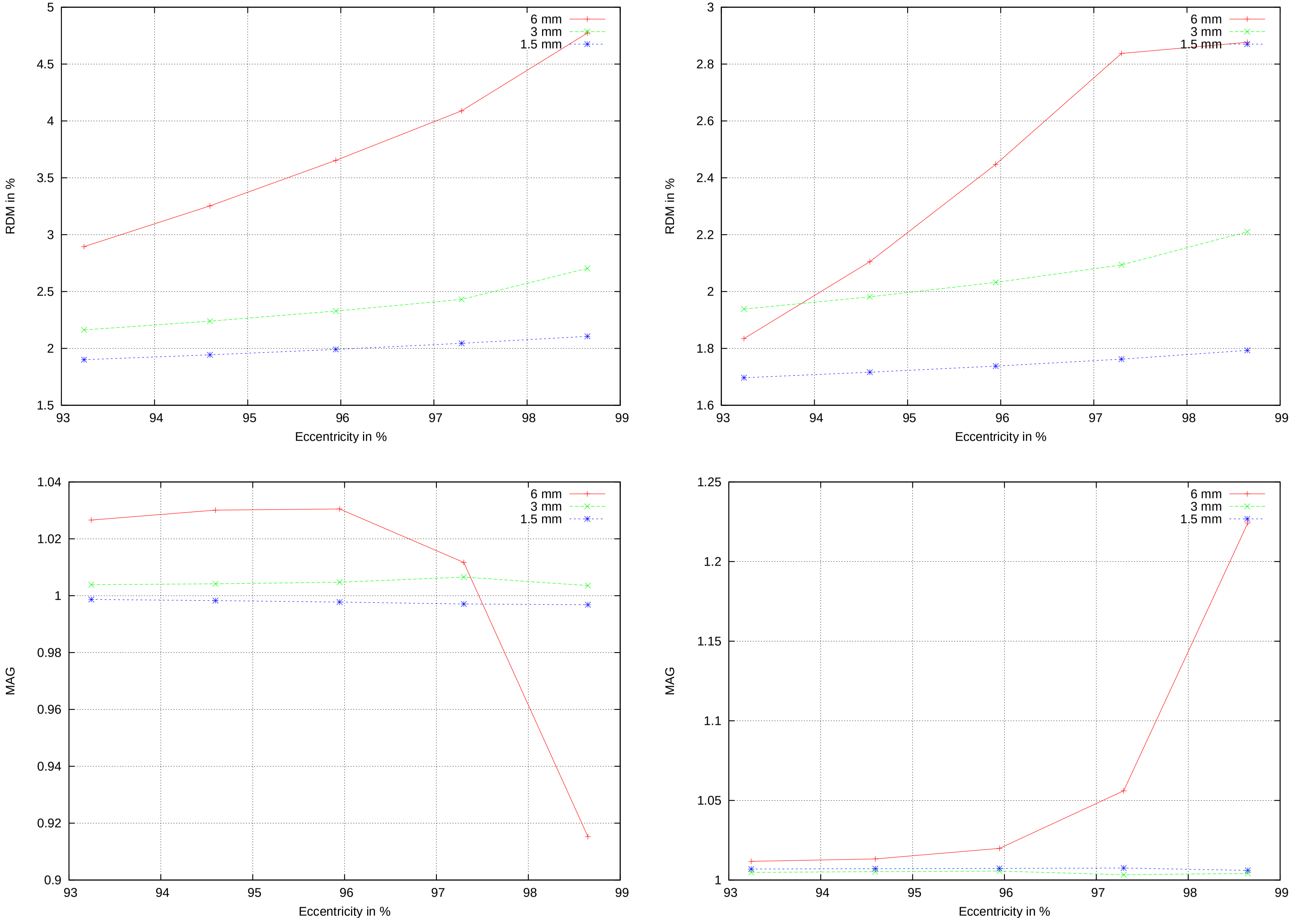

Figure 3.16: RDM (top) and MAG (bottom) for radial (left) and tangential (right) dipole orientations with varying surface solution h for the meshes of the second refinement series of Group 2b

The error convergence towards the analytical solution when increasing the surface mesh resolution can also be seen if the CSF compartment is made thicker, as is the case for the meshes of the refinement group 2.

Table 3.9 lists the errors for the most eccentric dipole and Figure 3.17 depicts the dependence of the relative error from the mesh resolution h.

h in mm	**RE** rad in %	**RDM** rad in %	**MAG** rad	**RE** tang in %	**RDM** tang in %	**MAG** tang
6	12.4596	4.77351	0.915252	23.3077	2.87671	1.22422
3	5.42823	2.70347	1.00356	4.44889	2.21003	1.00417
1.5	4.2178	2.10626	0.996825	3.64848	1.79317	1.00609

Table 3.9: Errors for the most eccentric dipole in the meshes of the second refinement group in Group 2b

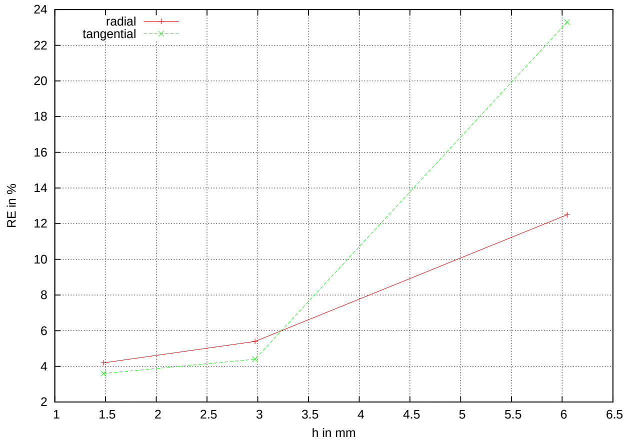

Figure 3.17: RE of the dipole with highest eccentricity of the second refinement series of Group 2b depending on the surface resolution h

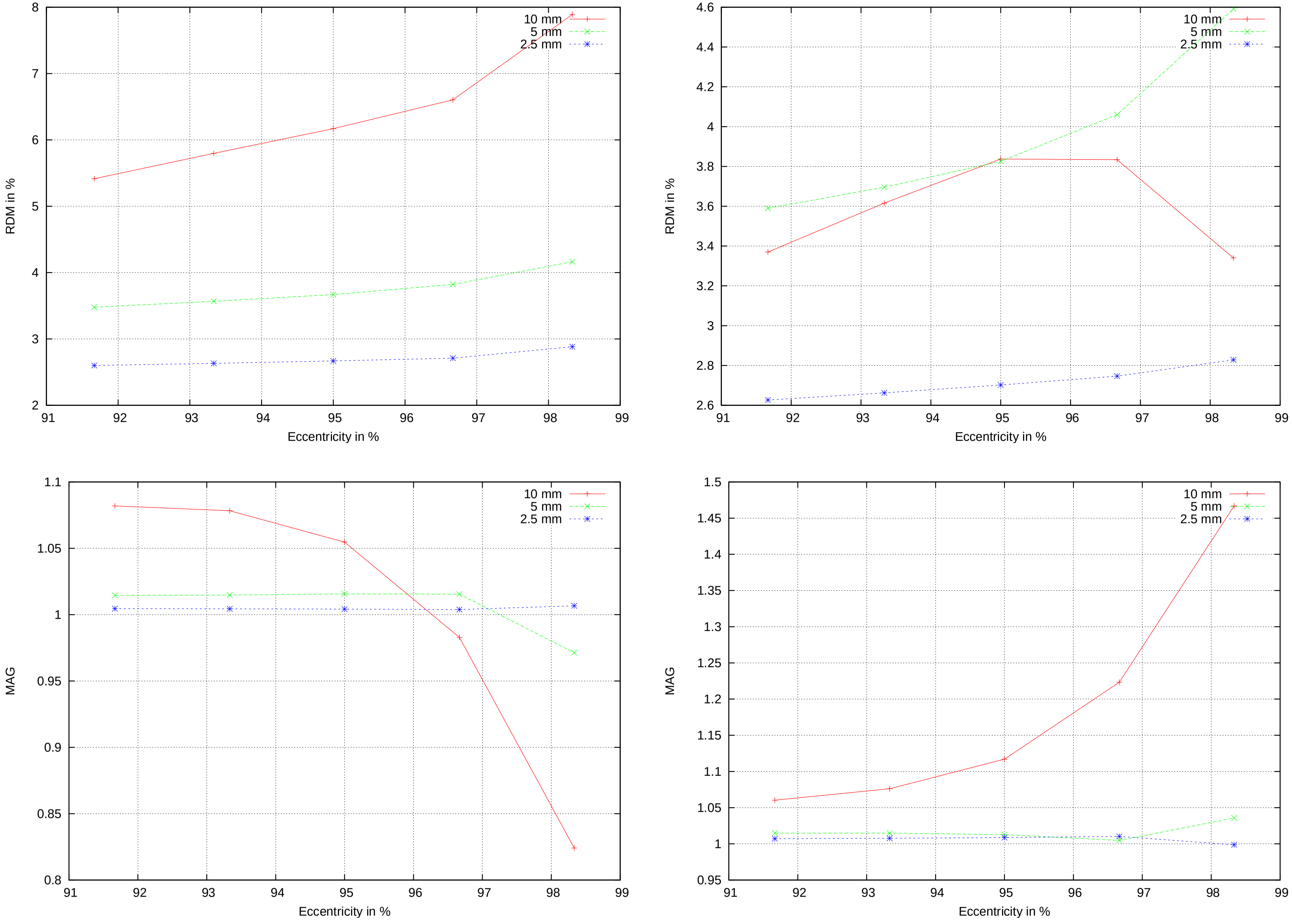

Figure 3.18: RDM (top) and MAG (bottom) for radial (left) and tangential (right) dipole orientations with varying surface solution h for the third refinement series of Group 2b

Even if all the outer compartments are modeled with the same thickness of one centimeter (refinement group 3) the numerical errors to the analytical solution are in the same range as for the second refinement series. As seen in Figure 3.18 the RDM value is below 10 % for all dipoles and the MAG is close to 1 at least for the two finer models. Table 3.10 lists the errors for the last dipole position, which are also plotted against the surface resolution h in Figure 3.19.

h in mm	**RE** rad in %	**RDM** rad in %	**MAG** rad	**RE** tang in %	**RDM** tang in %	**MAG** tang
10	22.6859	7.89137	0.824112	47.3902	3.33986	1.46695
5	8.68974	4.16261	0.97139	10.0043	4.59151	1.0357
2.5	5.82281	2.88257	1.00668	5.65428	2.82825	0.998621

Table 3.10: Errors for the most eccentric dipole in the meshes of the third refinement group in Group 2b

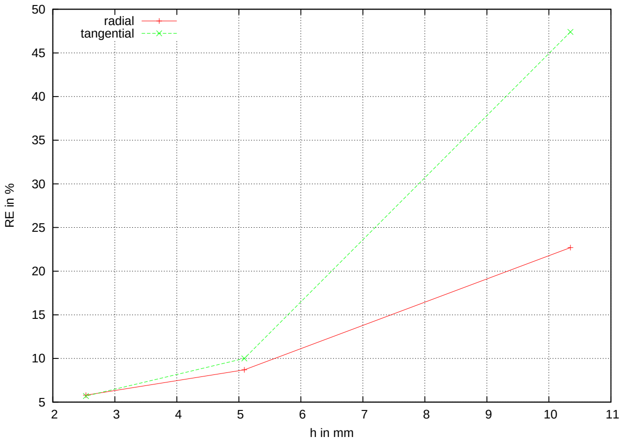

Figure 3.19: RE of the dipole with highest eccentricity of the third refinement group of Group 2b depending on the surface resolution h

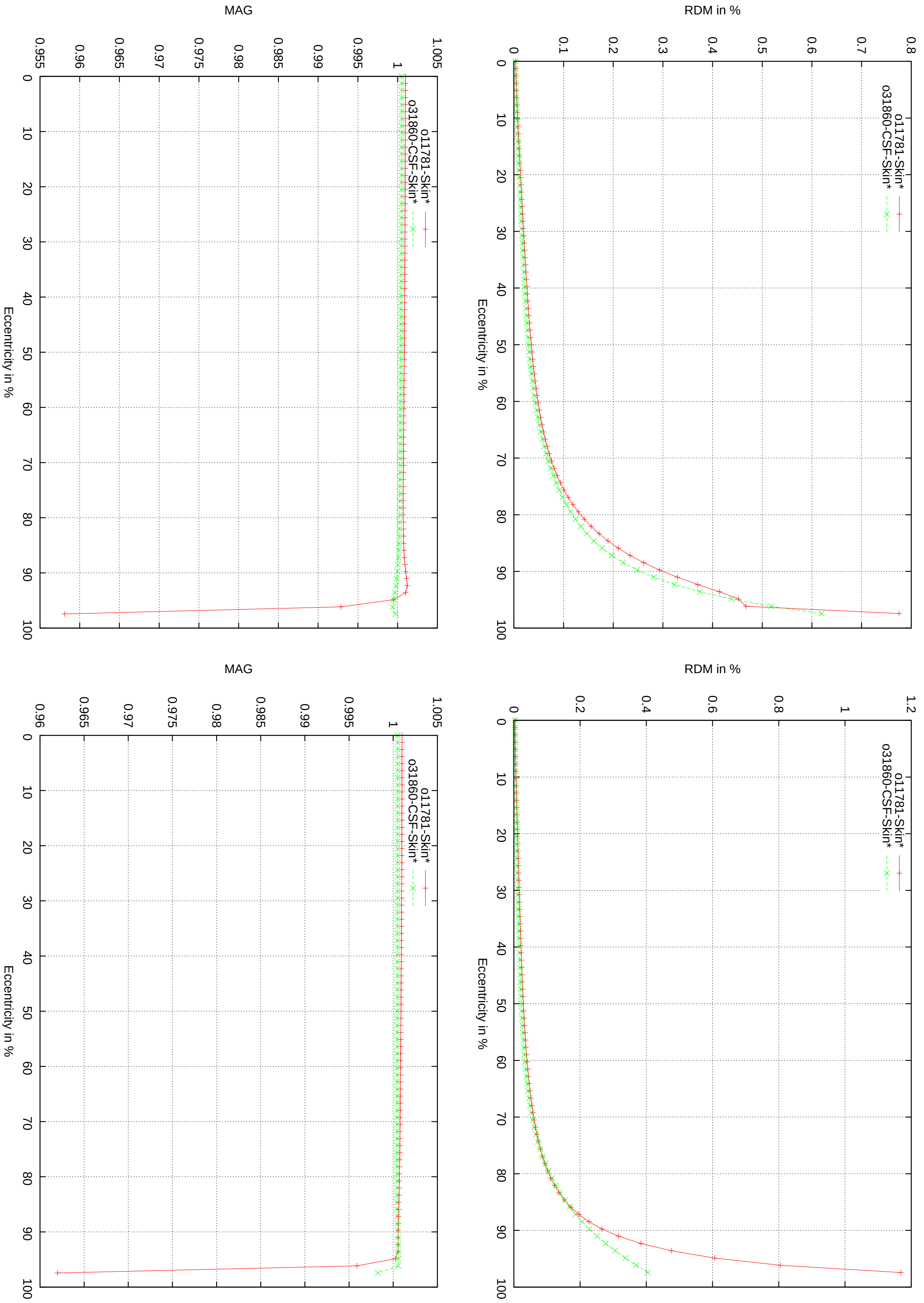

Figure 3.20: RDM (top) and MAG (bottom) for radial (left) and tangential (right) dipole orientations for the models of Group 3

Group 3 - Specifically Tuned Meshes

As mentioned above the last two multilayer sphere meshes were specifically tuned for the numerical needs of the subtraction approach, so the RDM values for both radial and tangential sources are below 1 % for all but the last source.

The MAG is very close to the optimal value of 1, only for the last dipole position there is a bigger difference of about 0.05 (for the radial direction).

Model	**RE** rad in %	**RDM** rad in %	**MAG** rad	**RE** tang in %	**RDM** tang in %	**MAG** tang
`o11781-Skin`	4.45636	0.775647	0.958103	4.43942	1.16863	0.961982
`o31860-CSF-Skin`	1.23972	0.619797	0.999731	0.82759	0.404854	0.998256

Table 3.11: Errors for the most eccentric dipole in the meshes of the Group 3

The meshes of Group 3 perform best regarding numerical accuracy because they combine high initial sphere surface resolutions with tight volume constraints for the skin and CSF compartment respectively.

Judging from the results of the Group 1 meshes it should be possible to lower the numerical errors even further by also constraining the tetrahedra volume in the brain compartment, though the computational effort would then be even higher than for the two million elements of the `o31860-CSF-Skin` model.

A study basing partially on this work and comparing the subtraction approach to other dipole approaches and different solver methods can be found in [1].

4 Application on Realistic Head Models

In this chapter the previously mentioned mesh generation techniques are applied to construct a realistic head model with an implanted intracranial electrode grid made from an electrically isolating silicone elastomer. The impact of this very badly conducting sheet of plastic on EEG measurements is studied as well as its influence on inverse techniques like source localization. Finally the generated volume conductor model is used to perform source localization on a highly dipolar EEG pattern measured in an epilepsy patient.

4.1 Motivation

Epilepsy is a common neurological disorder affecting over 50 million people worldwide and remains inadequately controlled in 30% of the patients. Even those whose seizures are controllable may suffer from chronic medication side effects and cuts in their personal lives[38].

Presently treatment options for patients suffering of epilepsy that cannot be treated medically narrow down to implantation of a vagus nerve stimulator that is connected to the subject's chest wall or surgical removal of the epileptogenic areas of the brain[39, 40]. Whereas the implantation of the nerve stimulator rarely leads to complete seizure freedom the epilepsy surgery has best chances of providing a cure, but it is only applicable, when the source region of the epileptic foci can be accurately localized and safely removed.

The current concept for epileptic seizures assumes a discrete area of the brain becoming active, the so called *Ictal Onset Zone IOZ*. The activation then propagates to the surrounding tissue, the *Epileptogenic Zone EZ*, to generate seizures. It is believed, that upon removal of both the IOZ and the attached EZ the patient should become seizure-free[41].

In order to localize this IOZ patients EEG data are recorded during a seizure and the active brain areas are reconstructed by means of source analysis.

4.2 Epilepsy Patient's Head Model

In a preliminary data collection for a larger epilepsy study at the Mayo Clinic, Rochester, USA, the University of California, San Diego and the University of Utah, Salt Lake City, one subject with medically intractable epilepsy underwent intracranial monitoring and had a 78 channel iEEG electrode grid implanted[5]. Simultaneously a regular 29 channel surface EEG was recorded. To implant the electrode grid, the subject's head was opened and part of the skull removed. Then the plastic sheet was placed directly on the cortex, and the wound was closed with a pressure bandage.

Presurgically a T1-MRI was recorded with a resolution of 256 slices in axial, 256 in sagittal and 120 in coronal direction and a voxel-size of $0.86\times1.6\times0.86$ mm. Furthermore, a post-surgical CT was taken with a resolution of 68 slices in axial, 512 in sagittal and 635 in coronal direction and a voxel-size of $0.49 \times 0.49 \times 2.65$ mm (see figure 4.1). The iEEG electrode positions were reconstructed from the CT.

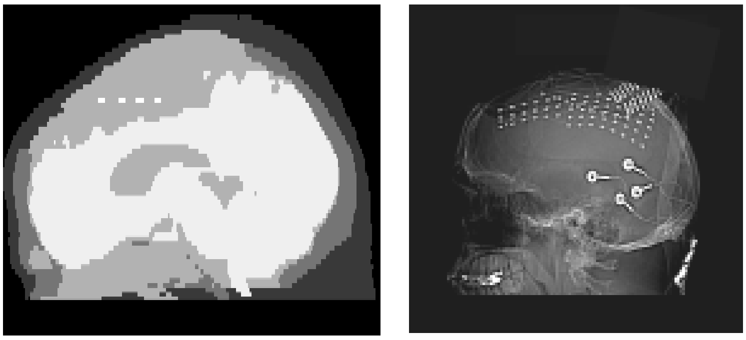

(a) Pre-surgical MRI, registered and segmented

(b) Post-surgical CT

Figure 4.1: Pictures with implanted electrodes grid. (a) Pre-surgical MRI with skull trepanation hole, (b) Post-surgical CT with 2 electrode grids and 4 sEEG electrodes visible (down right)

For data evaluation and numerical simulations a three-dimensional volume conductor model was then constructed from the image slices. Therefore the MRI dataset was loaded into the commercial software CURRY[42] which is able to segment the different compartments of the brain by their gray value. The triangulated surfaces of the segmented brain compartments were then exported and subjected to a meshing procedure with TetGen as described in Section 3.1.2.

4.2.1 Modeling the Plastic Sheet

In order to generate a three-dimensional tetrahedral mesh of the plastic sheet from the given electrode positions (Figure 4.2(a)) first a closed surface has to be created, that can be meshed with TetGen. To do so each of the 108 given points defining the two-dimensional surface was shifted in the average surface normal direction of the triangles it belongs to (see Section A.1 for a detailed explanation), thus creating a second surface (the green line in Figure A.1(c) on Page 92).

The resulting model of the plastic sheet has a thickness of 0.127 mm, which forces the mesh generator to create a big number of very small tetrahedra.

Because of the brain shift[43] and the different imaging modalities the electrode locations and the head compartments are based on, the grid surface intersects with the brain surface at several points. Moreover also the inner and outer skull surface pose a problem, because both base on pictures where already a big part of the skull is missing.

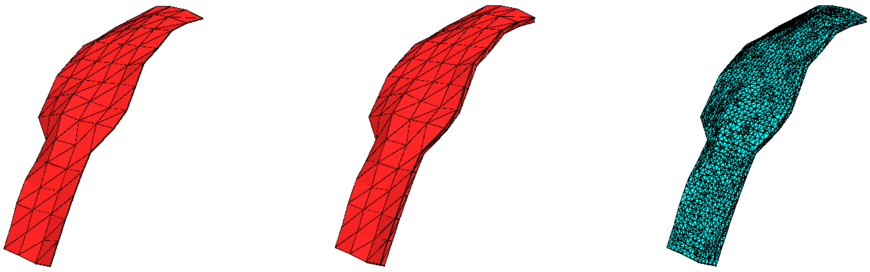

(a) Two-dimensional grid surface (b) Three-dimensional closed surface suitable for meshing (c) Final tetrahedral mesh of the grid

Figure 4.2: From two-dimensional surface to three-dimensional tetrahedra mesh

The resulting hole and the implanted grid can not be modeled by closed surfaces anymore as TetGen requires. The skull is further problematic in the lower areas near the neck, where the spine passes through. The skin surface layer also leads to intersections in that area because the MR data ends there.

Therefore another approach was taken. First the non-intersecting surfaces that TetGen can mesh without problems are used to create a preliminary head model without any volume constraints. This does not incorporate every head compartment and has very large tetrahedra away far from the surface. One by one the missing compartments (including the grid) are added to the model by inserting the surfaces' points using TetGen's `-I`-switch. With this option it is possible to add a list of points to an existing tetrahedra mesh.

Using this technique on the problematic surfaces of the outer and inner skull resulted in a tetrahedra model that incorporates the layers skin, skull with trepanation hole, CSF, brain and the plastic sheet. The final realistic head model with the inserted grid points is presented in Figure 4.3. It consists of 116651 nodes which form 662099 tetrahedra.

But as in the process points are inserted into an already existing tetrahedra mesh the automatic labeling algorithm of TetGen (see Section 3.1.2) cannot determine which material each tetrahedron has to be assigned. Therefore after mesh generation an additional labeling step has to be performed in order to assign the correct conductivities.

The labeling approach used in this thesis identifies each tetrahedron by its barycenter and checks if it lies inside a given closed surface. It is described in detail in Section A.2. This conservative approach is very slow, because for every tetrahedron of the 662099 elements it has to loop over every triangle of the defining surface. At a resolution of 2.5 mm these surfaces have about 20000 to 30000 triangles. Therefore the runtime of the labeling algorithm lasts even on a dual core Desktop machine for several hours.

To evaluate the impact of the grid on source simulations and reconstruction a second model without implanted plastic sheet was created by using the aforementioned labeling approach and assigning every tetrahedron belonging to the plastic sheet the conductivity of the CSF, thus effectively removing the sheet.

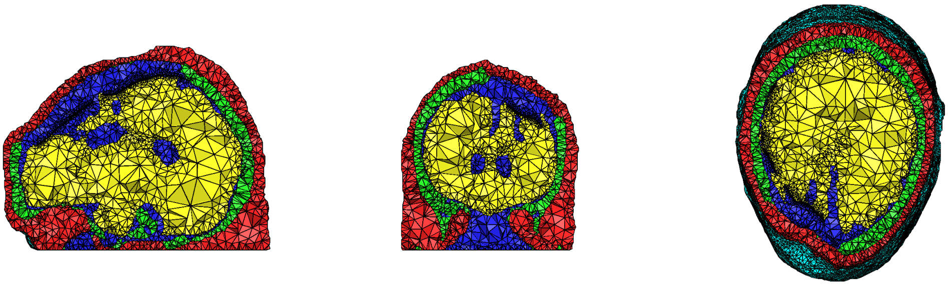

(a) Cross-sections in sagittal, frontal and transversal directions

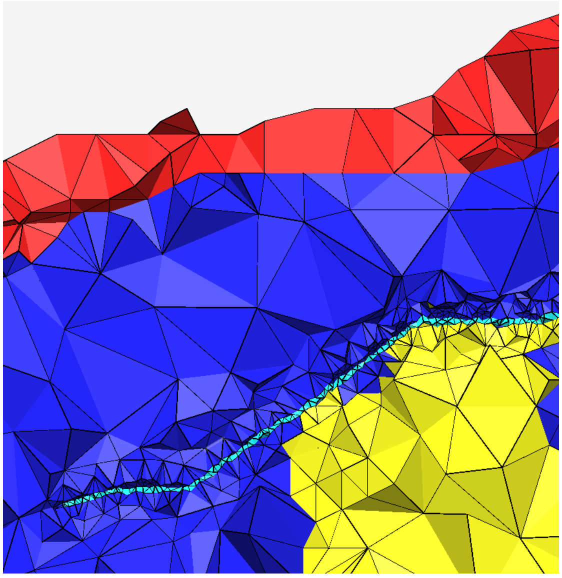

(b) Zoomed into grid region

Figure 4.3: Realistic FEM model of the epilepsy patient's head with the intracranial electrode grid (light blue)

4.3 Sensor Configuration

As mentioned in section 4.2 for the data acquisition of the epilepsy patient a surface EEG and an intracranial EEG were recorded simultaneously. Figure 4.4(a) shows the location of the 30 sEEG electrodes in relation to the brain surface while Figure 4.4(b) depicts the implanted plastic sheet with the subdural electrode layer.

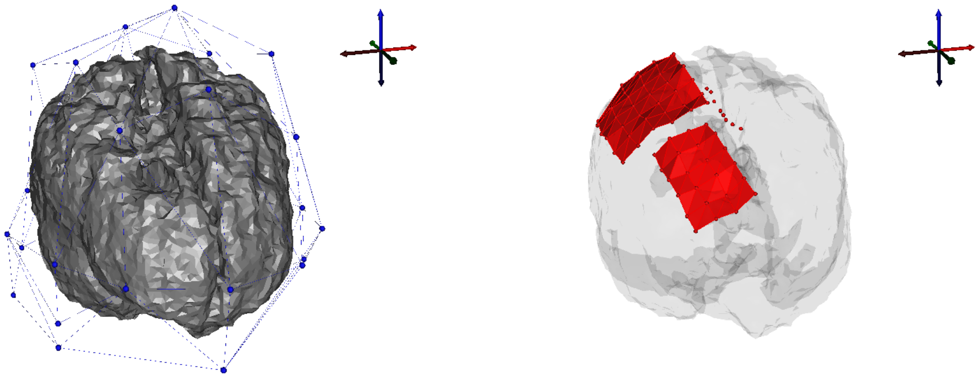

(a) The 30 sEEG sensor locations

(b) The 78 iEEG sensor locations

Figure 4.4: The locations of the 108 electrodes which where measured simultaneously

The plastic sheet in fact consists of two separated electrode layers, a small 4 × 6-electrode sheet and a bigger 6 × 8-electrode grid with only 46 sensors. Furthermore a separate strip consisting of eight measurement sensors was deposited in the interhemispheric fissure (*fissura cerebri longitudinalis*).

4.4 Error Measures

In the following sections forward and inverse calculations are compared, that were generated with and without the grid. In inverse computations, the reference data were simulated in the model with grid and the dipole fits were always run in the model without the grid.

4.4.1 Errors in forward calculations

To describe the errors between forward calculations again the RDM (3.7) and MAG (3.6) values from Section 3.4 are used.

4.4.2 Errors in inverse calculations

To quantify the error between an original and the corresponding reconstructed current dipole the overall error is split up in three parts that are presented separately, namely a spatial error or *error in space*, an *angular error* and an *error in magnitude*. These are examined independently from each other.

Dipole #	**x** in mm	**y** in mm	**z** in mm	**Magnitude** in nAm
1	110.0	102.16	150	100
2	110.0	102.16	160	100
3	110.0	102.16	170	100
4	110.0	102.16	180	100
5	110.0	102.16	190	100

Table 4.1: Locations and Magnitudes of the 5 dipoles

Error in space

An arrow is drawn from the original dipole position used to create the forward solution to the location resulting from a dipole fit. Thus, large arrows correspond to large spatial errors.

Error in angle

The angle between the original dipole direction $\boldsymbol{a}$ and the fitted dipoles direction $\boldsymbol{b}$ is calculated via the dot product of the two:

$$\angle(\boldsymbol{a};\boldsymbol{b}) = \arccos \frac{\boldsymbol{a}\cdot\boldsymbol{b}}{||\boldsymbol{a}||_1 \cdot ||\boldsymbol{b}||_2} \tag{4.1}$$

The resulting value is displayed as a scaled colored sphere, i. e. the bigger the sphere the larger is the angle between fitted and original dipole direction.

Error in magnitude

The last error measurement is the difference between the magnitude of the reconstructed current dipole and the original one:

$$\Delta M = M_{\text{reconstr}} - M_{\text{orig}}. \tag{4.2}$$

Again scaled spheres are used to visualize this difference in the figures in Sections 4.5.2 and 4.5.2.

4.5 Results

In order to evaluate the impact of the plastic sheet on source reconstruction first its influence on forward calculations is studied. Then the effect on inverse computations is investigated by source analysis of synthetic forward data for different dipole positions directly underneath the grid and throughout the whole brain volume.

The computations in this chapter were performed using the Venant dipole model (see Section 2.5.1). The accuracy is sufficient and the speed of the current implementation outperforms the subtraction approach by far[44].

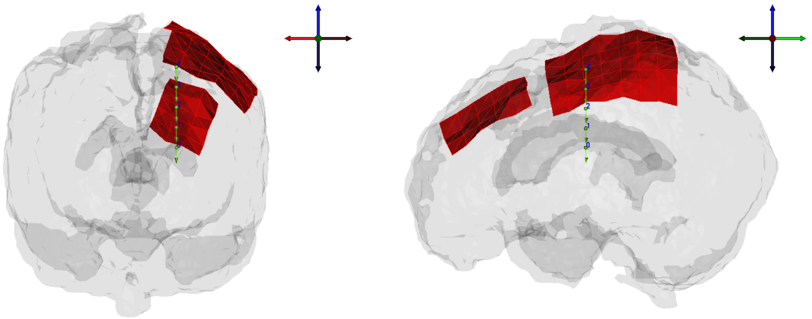

(a) Radial (z-) direction

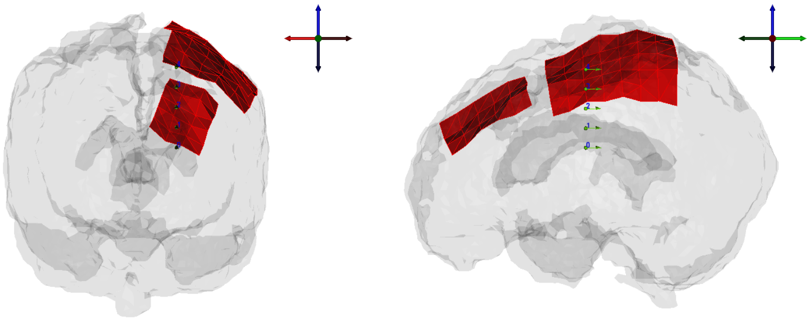

(b) Tangential (y-) direction

Figure 4.5: The five dipoles underneath the grid in radial (z-) and tangential (y-) direction

Dipole number	**Direction**	**RDM in %**	**MAG**
1 (farthest from the grid)	radial	1.85646	1.02583
2	radial	4.2335	1.0845
3	radial	6.01525	1.11145
4	radial	6.82394	1.1033
5 (closest to the grid)	radial	17.1966	1.46569
1	tangential	3.47796	1.01836
2	tangential	4.38049	1.0214
3	tangential	9.94436	1.04499
4	tangential	15.9249	0.975701
5	tangential	19.0578	1.03737

Table 4.2: RDM and MAG between forward solutions with and without grid for the five dipoles in radial and tangential direction

4.5.1 Influence of the plastic sheet on forward calculations

As the electrode grid will have the most influence on sources located directly underneath it, five dipoles were placed in arising order below it as seen in Figure 4.5. Each source was placed both in z- and in y-direction (quasi-radial and -tangential to the grid). Table 4.1 shows the respective spatial position and the induced dipole moment.

The forward solutions for these five sources were calculated using the Venant dipole approach once for the model without the plastic sheet and once for the model with included grid. The effect of the plastic sheet on these forward calculations is shown in Figure 4.6 on page 57. The upper rows of Figs. 4.6(a) and 4.6(b) show the potential on the surface of the head calculated in the model without the grid, whereas the corresponding lower rows depict the scalp potential if the grid is present.

It is noticeable that the smaller the distance of the dipole to the grid gets, the more the potential is affected. Because of the very low conductivity of the silicone material the grid is made of, volume currents in the head will have to flow around it thus blurring and smearing the resulting dipolar pattern. This effect can be observed especially good for the two topmost dipoles close to the grid.

This result is also striking in the values of the RDM calculated for the forward solution without the grid with respect to the results with included plastic sheet. These are listed in Table 4.2 and are maximal for the last two dipole positions. For both radial and tangential directions one pole of the potential distribution nearly vanishes when the source comes close to the grid. RDM values of up to 19 % for the tangential and 17 % for the radial direction resemble this. The MAG values for the tangential sources however do not diverge much of the optimal value 1.0, which indicates that the difference is mere topological and the strength of the remaining unblurred pole is nearly accurate. For the radial case the effect of the grid on the MAG is much stronger.

4.5.2 Influence of the plastic sheet on inverse calculations

As a first step in examining the grid's impact on inverse calculations the calculated forward potential in the model with grid (see Figs. 4.6(a) and 4.6(b), bottom row) was used as reference for a dipole fit procedure (see Section 2.7.1) in the model without grid. This approach will show the errors in source localization if the insulating plastic sheet is not accounted for in a realistic head model.

In order to avoid the simplex optimizer getting stuck in local minima of the cost function the optimization procedure was started from sixteen different seeding positions and the solution that explains most of the input data was kept. The sixteen different seed points are shown in Figure 4.7.

The results of the dipole fit for all five dipoles in both directions are shown in Table 4.3. The third radial dipole has a very high error in magnitude because it was placed in a highly conductive CSF element by the simplex optimizer which is not restricted as to where it may put the source. Apart from this outlier the localization errors are in the sub-centimeter range for every dipole.

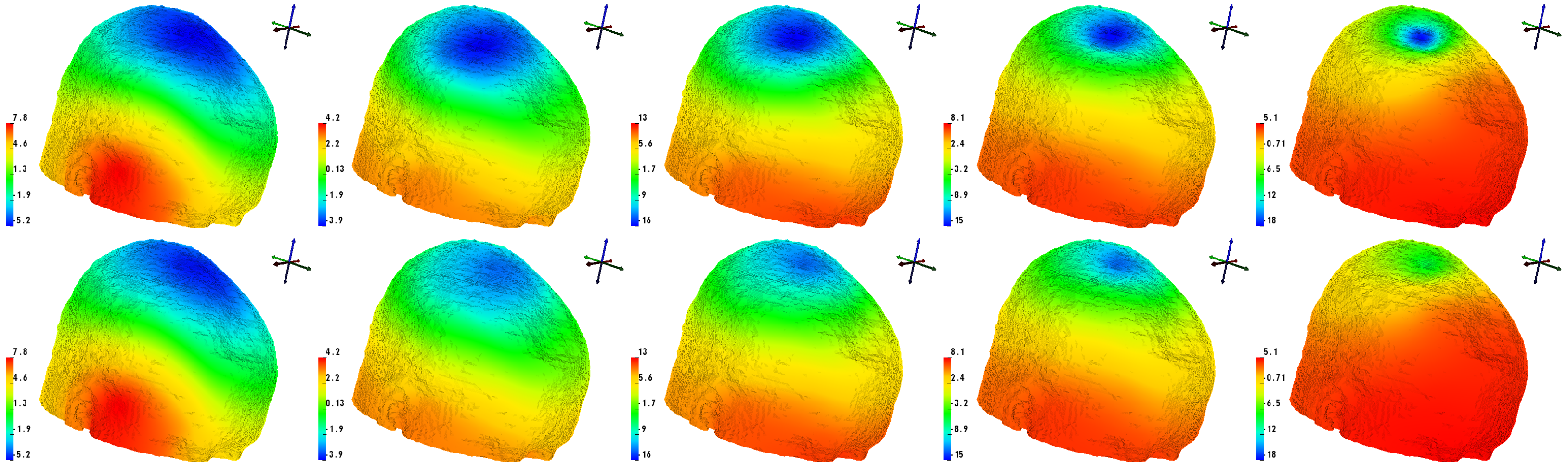

(a) Radial direction

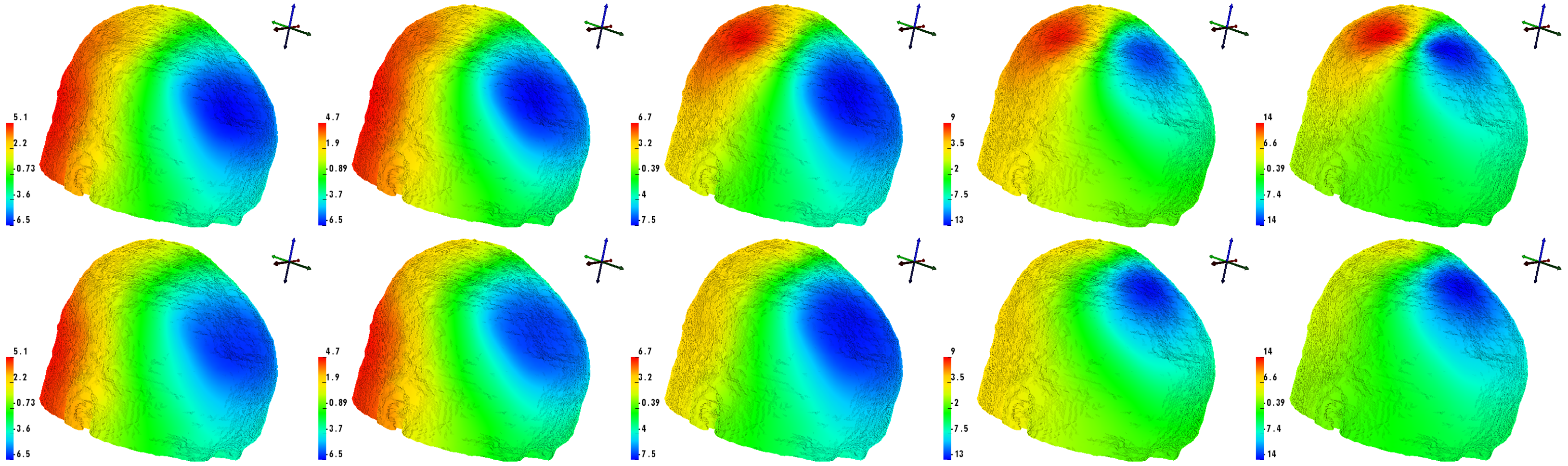

(b) Tangential direction

Figure 4.6: Effect of the plastic sheet on forward calculations for the 5 dipoles in radial and tangential direction
Top row: calculation without plastic sheet, bottom row: calculation with plastic sheet
Left to right: dipole #1 – #5; The scale is μV

	Fit Location			Error	Fit Moment			Error	Fit Amplitude	Error
	x	y	z	$\lvert \boldsymbol{d} - \boldsymbol{d}_{\mathrm{orig}} \rvert_2$	x	y	z			
	in mm	in mm	in mm	in mm	in nAm	in nAm	in nAm	in °	in nAm	in nAm
Dip 1 rad	112.576	101.756	150.186	2.614	−0.34	0.02	−0.94	19.75	108.094	8.094
Dip 2 rad	119.095	101.913	156.663	9.691	−0.05	0.03	−1.00	3.50	101.138	1.138
Dip 3 rad	117.727	101.898	161.048	11.829	−0.11	−0.17	−0.98	11.50	293.403	193.403
Dip 4 rad	116.689	103.531	176.281	7.775	−0.02	−0.05	−1.00	3.04	77.3273	−22.6727
Dip 5 rad	113.182	102.598	186.656	4.637	0.09	−0.26	−0.96	15.92	80.594	−19.406
Dip 1 tang	116.118	104.594	147.832	6.932	0.34	0.94	−0.01	20.12	101.943	1.943
Dip 2 tang	114.817	105.707	160.093	5.983	0.11	0.99	0.03	6.73	100.644	0.644
Dip 3 tang	116.400	104.681	167.714	7.249	−0.13	0.99	−0.10	9.49	109.855	9.855
Dip 4 tang	112.422	103.436	177.850	3.481	0.17	0.98	−0.08	10.66	109.037	9.037
Dip 5 tang	114.783	106.422	184.616	8.368	0.11	0.99	−0.03	6.79	109.829	9.829

Table 4.3: Dipole fit errors of the five dipoles of Figure 4.5

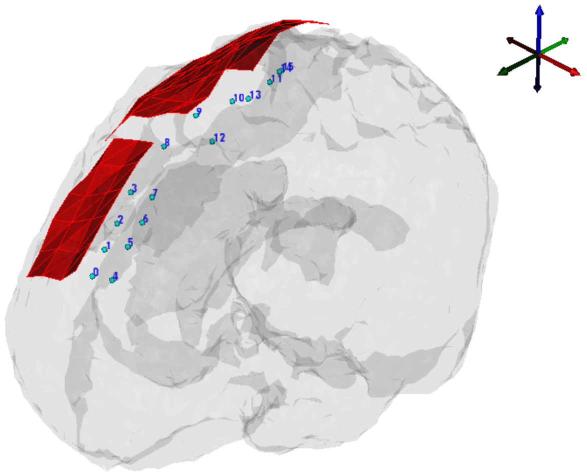

Figure 4.7: The sixteen different seed points for the simplex optimizer

For a deeper understanding of the grid's effects on source reconstruction the same calculation method was performed for a higher number of dipole locations and directions.

To find the directions for the sources that would have the biggest impact on the inverse calculation the following steps were carried out:

- For each dipole position three forward calculations were performed in the model with the plastic sheet wherein which the source was oriented in x-, y- and z-direction respectively.
- The leadfield matrix $A \in \mathbb{R}^{3 \times n_{\text{sens}}}$ was constructed which contains those forward solutions as row vectors.
- A singular value decomposition (SVD) of A was calculated so that $A = U \cdot \Sigma \cdot V^T$. The rectangular diagonal matrix Σ then contains the so called *singular values* of A which are usually ordered in a non-increasing fashion.
- The columns of the matrix $U \in \mathbb{R}^{3 \times 3}$ belonging to the biggest and the smallest singular value of A were chosen as new directions for the dipole at the current position.

  This approach accounts for a possible misslocation of the electrode cap, because it includes the worst imaginable case of positioning: a source of interest that would contribute the least to the measured potential at the sensors. The two considered directions are referred to as the `strong` and the `weak` direction respectively.
- An alternative direction was determined by calculating the SVD for the matrix $B \in \mathbb{R}^{3 \times n_{\text{sens}}}$ containing the difference of two forward solutions (with and without the grid) in x-, y- and z-direction accordingly.

  The direction belonging to the biggest singular value of B therefore is mostly responsible for the "error", i.e. the deviation between the forward solutions with and without grid. It will be labeled the `maxerr` direction in the following.

By this procedure for each point three directions (`maxerr`, `strong` and `weak`) were constructed and a dipolar source was placed with these directions and a moment of 1 nAm. For these configurations the forward solutions were calculated again in the model with the plastic sheet and the obtained potentials at the electrodes were used as input for the inverse solver using a dipole fit routine in the model without grid.

Errors for dipoles in the whole brain volume

The first step in evaluating the impact of the grid for a higher number of dipoles was to place 3172 sources in the whole brain volume. This was accomplished by meshing the 2.5 mm-surface of the cortex that was exported from CURRY with TetGen and using the resulting tetrahedra corner nodes as dipole locations. Figure 4.8 shows these locations with light blue dots.

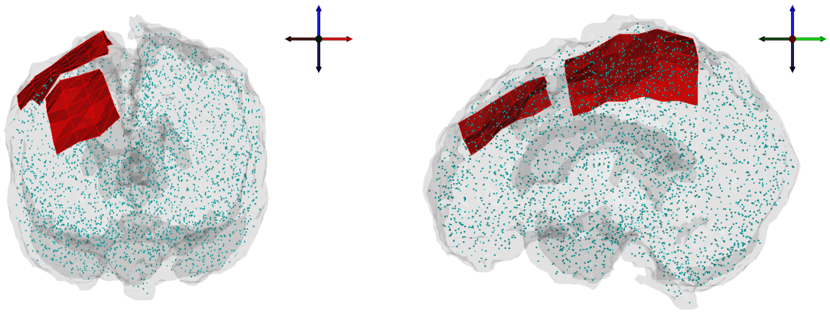

(a) Frontal view

(b) Left side view

Figure 4.8: The 3196 dipole positions spread over the whole brain volume

This series of dipole positions is referred to as the `wholebrainvol` dipole series. For each of these locations the procedure described above was applied, resulting in three error modalities as described in Section 4.4 for each of the three directions (these are shown in Figure B.5 on Page 101).

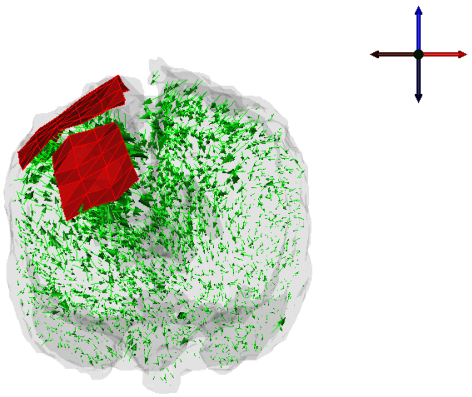

(a) Frontal view

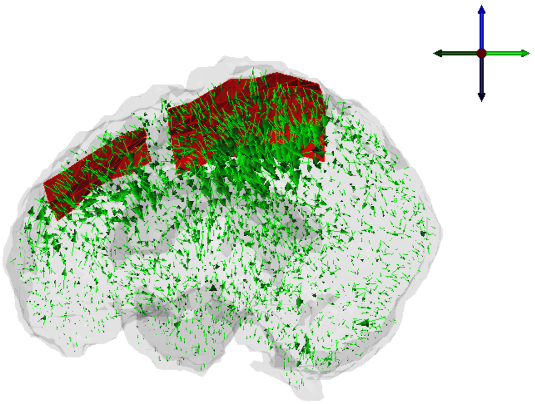

(b) Left side view

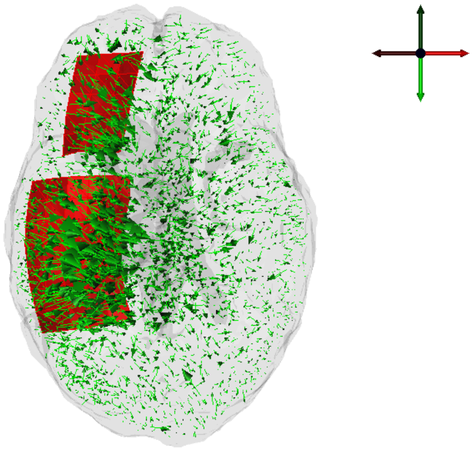

(c) Bottom view

Figure 4.9: Spatial errors for the `maxerr` direction in the whole brain volume. The arrows point from the original dipole position to the fitted location.

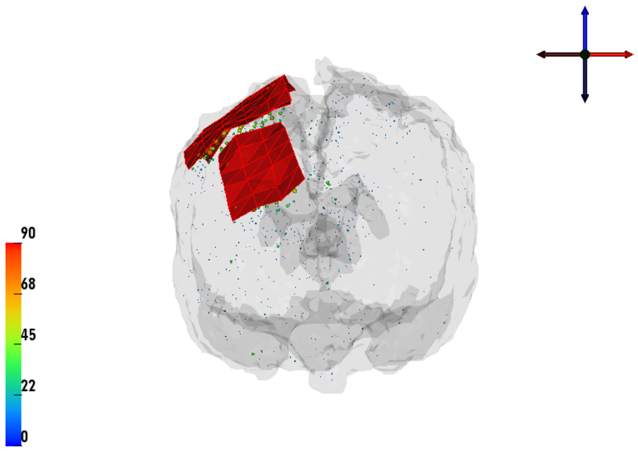

(a) Frontal view

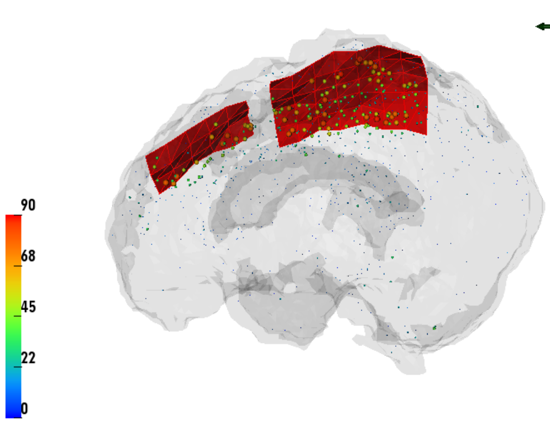

(b) Left side view

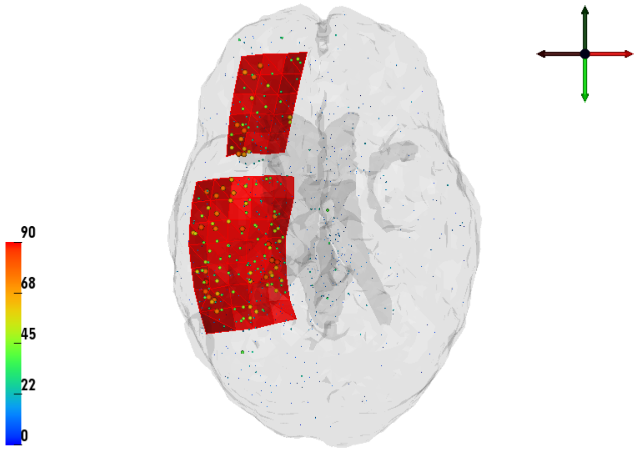

(c) Bottom view

Figure 4.10: Angle errors for the `maxerr` direction in the whole brain volume. The scale is in °.

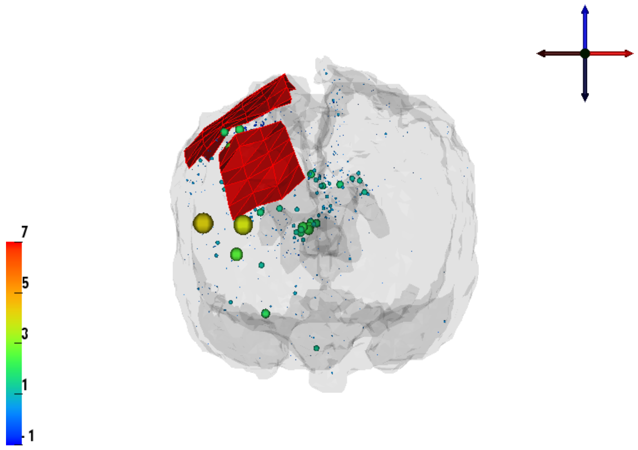

(a) Frontal view

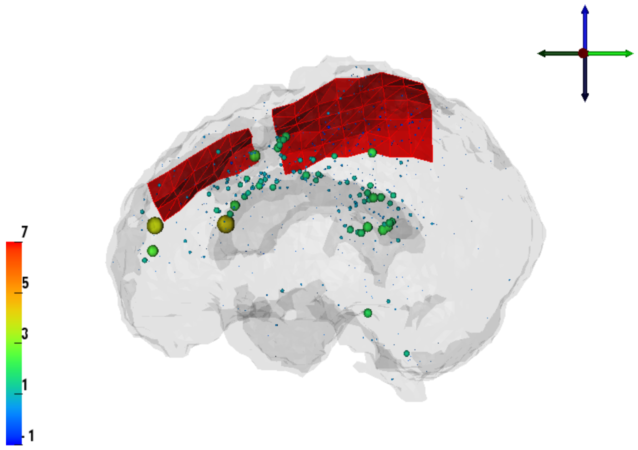

(b) Left side view

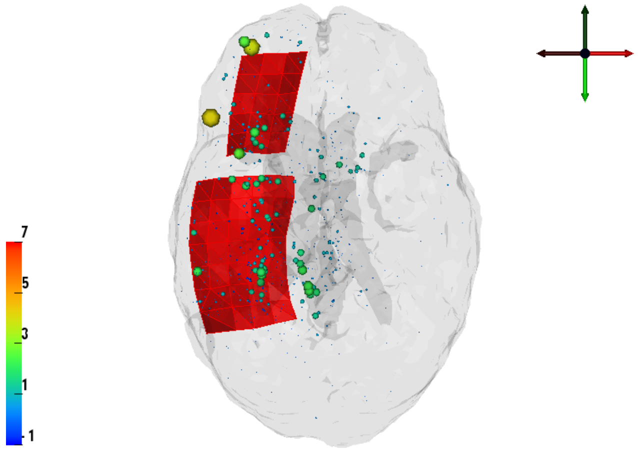

(c) Bottom view

Figure 4.11: Errors in magnitude for the `maxerr` direction in the whole brain volume. The scale is in nAm.

Figures 4.9 to 4.11 show the errors for the `maxerr` direction which are expected to be the highest of the different directions' values.

The spatial reconstruction error is in the subcentimeter range for the left hemisphere, which is not influenced much by the presence of the grid. For the dipoles located in the right hemisphere below the plastic sheet however a misslocalization of one to two centimeters is encountered. Here it is notable that most of the error arrows point away from the grid. The angle error is far below 20° throughout the brain volume, only at locations very close to the grid bigger angles between original and reconstruction occur (up to 90°). The magnitudes of the reconstructed dipoles are for most locations close to the originals, with differences of below 1 nAm. There occur higher magnitude errors of up to 600 % for locations deeper in the brain, especially near the spatial ventricles, as well as for some points in the right hemisphere. This can be caused by dipoles that were placed in a highly conductive CSF element by the optimizer, which is not restricted regarding the location of the fitted dipoles.

The error distribution for all three modalities is shown in the upper row of Figure B.7 on Page 103.

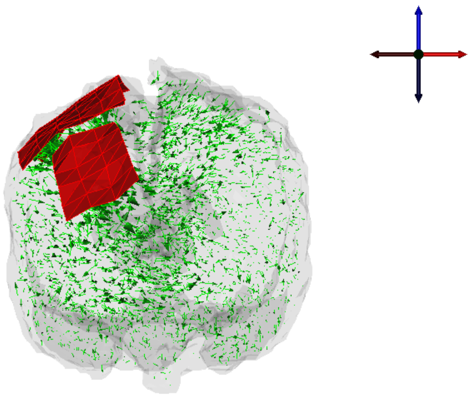

(a) Frontal view

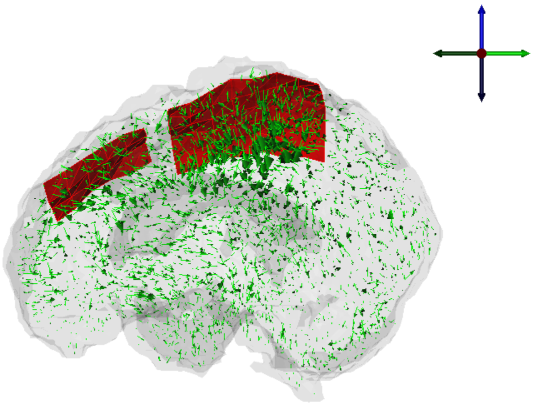

(b) Left side view

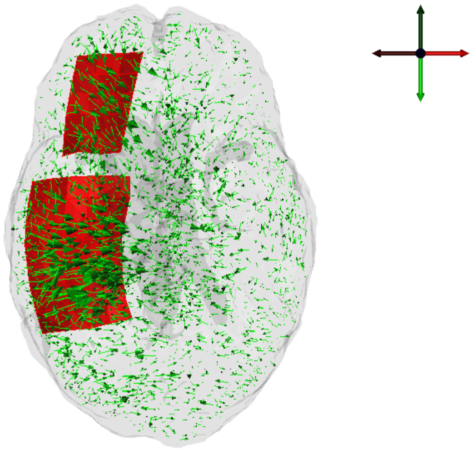

(c) Bottom view

Figure 4.12: Spatial errors for the `strong` direction in the whole brain volume. The arrows point from the original dipole position to the fitted location.

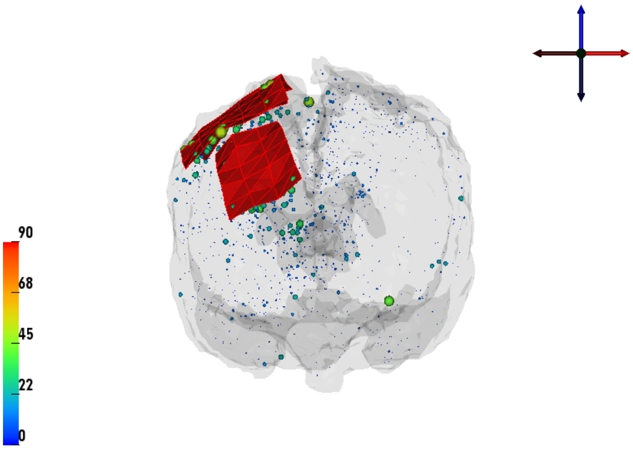

(a) Frontal view

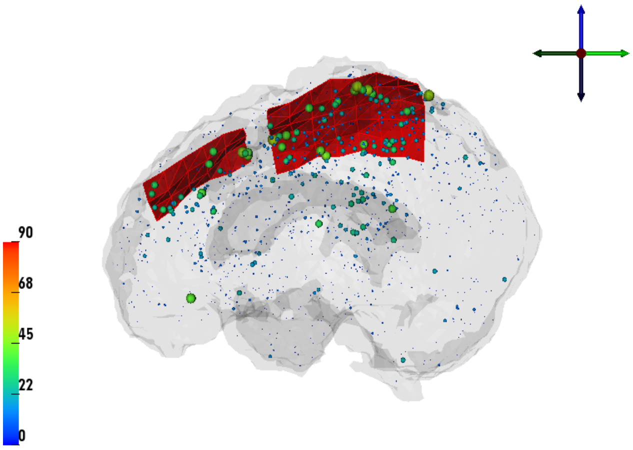

(b) Left side view

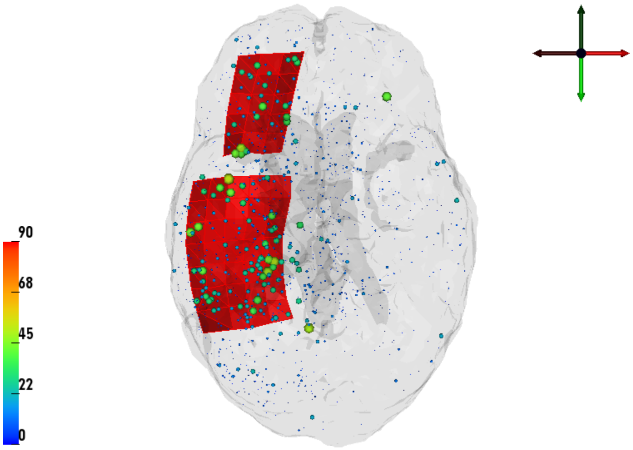

(c) Bottom view

Figure 4.13: Angle errors for the `strong` direction in the whole brain volume. The scale is in °.

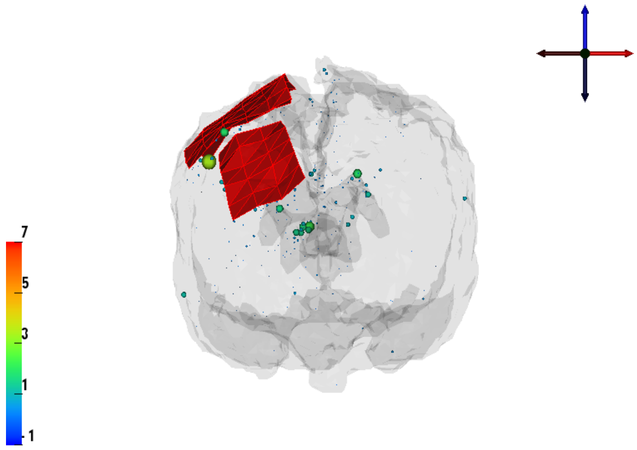

(a) Frontal view

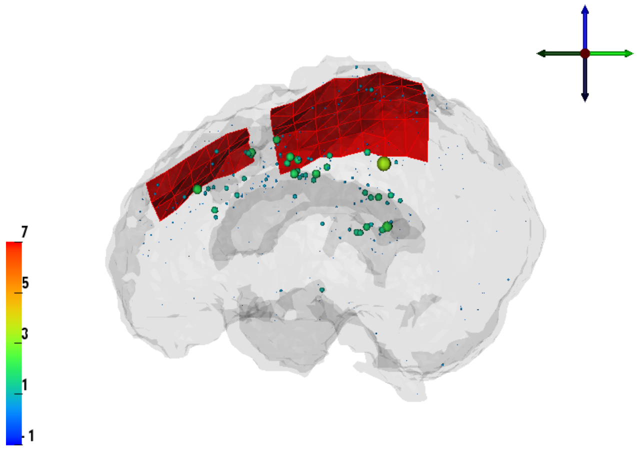

(b) Left side view

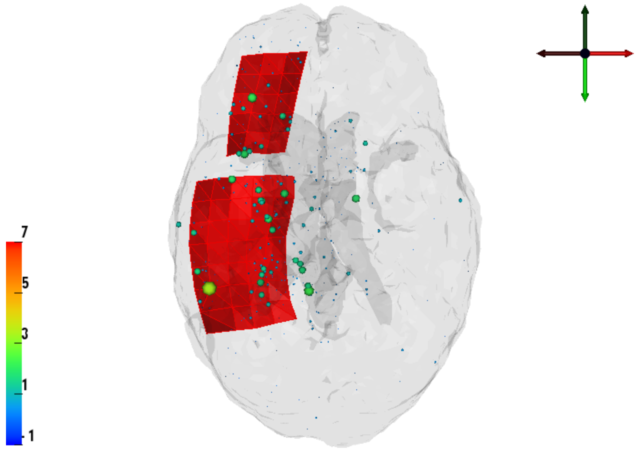

(c) Bottom view

Figure 4.14: Errors in magnitude for the `strong` direction in the whole brain volume. The scale is in nAm.

For the `strong` direction the errors of the `wholebrainvol` series are shown in Figures 4.12 to 4.14. Due to the construction of the different directions the error values for this direction should be the smallest of the three.

The spatial errors are indeed mostly smaller than for the `maxerr` direction (see also Figure B.7 on Page 103, middle row, and the mean values in Table 4.4). As well as for the other directions the arrows with maximal lengths tend to be focused under the grid and point away from it. The angle error distribution looks quite similar, however the absolute values are bigger for the `strong` direction. Especially some of the right-hemispherical points with angle differences of more than 45° stick out. Most locations exhibit a small to insignificant magnitude error. But again some higher errors appear to in the proximity of the plastic sheet, that are in the range of 1 nAm.

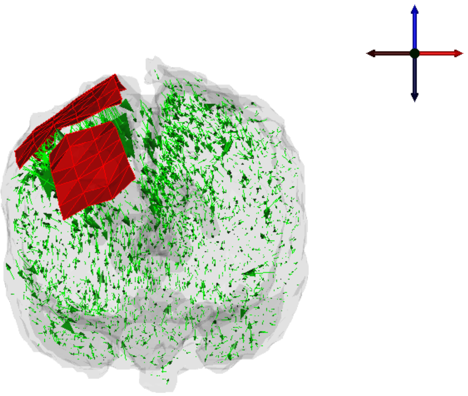

(a) Frontal view

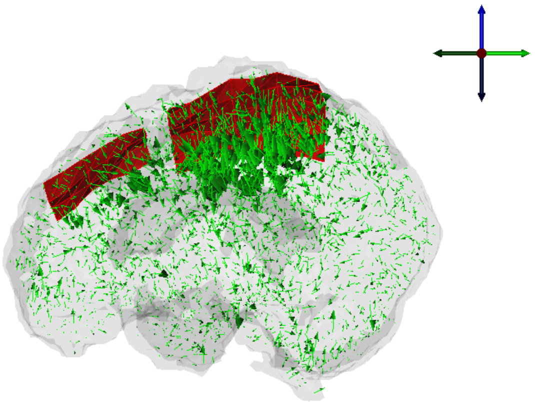

(b) Left side view

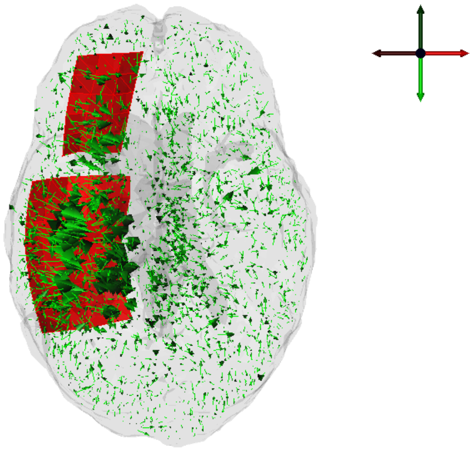

(c) Bottom view

Figure 4.15: Spatial errors for the `weak` direction in the whole brain volume. The arrows point from the original dipole position to the fitted location.

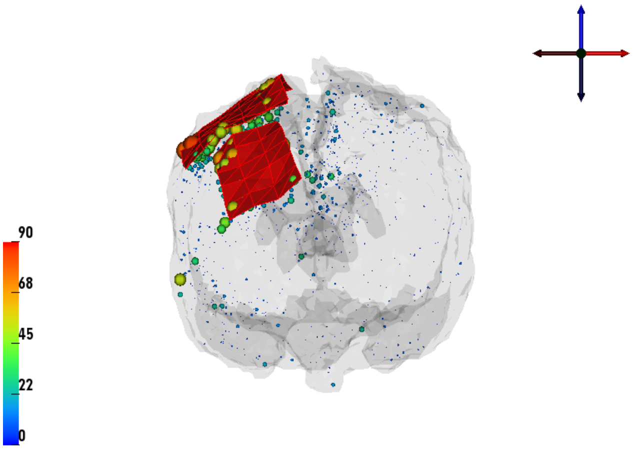

(a) Frontal view

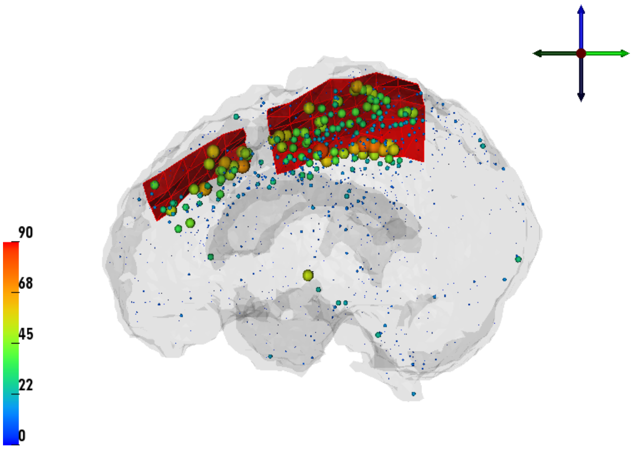

(b) Left side view

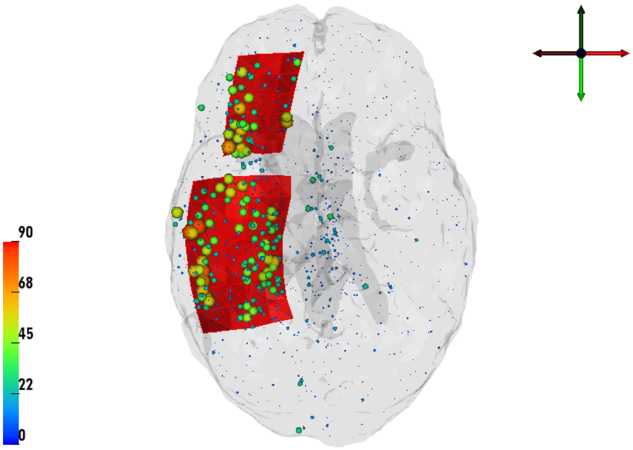

(c) Bottom view

Figure 4.16: Angle errors for the `weak` direction in the whole brain volume. The scale is in °.

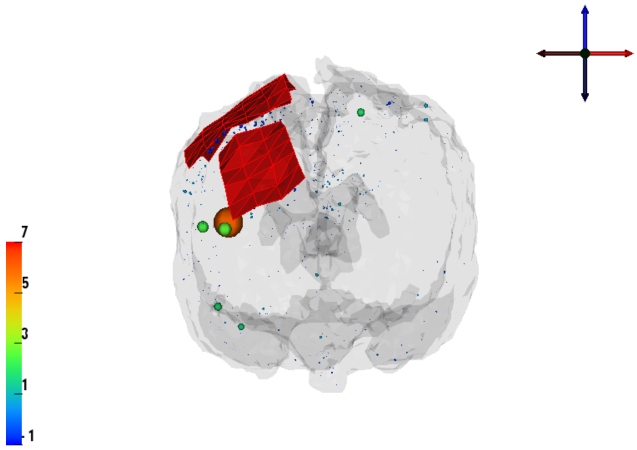

(a) Frontal view

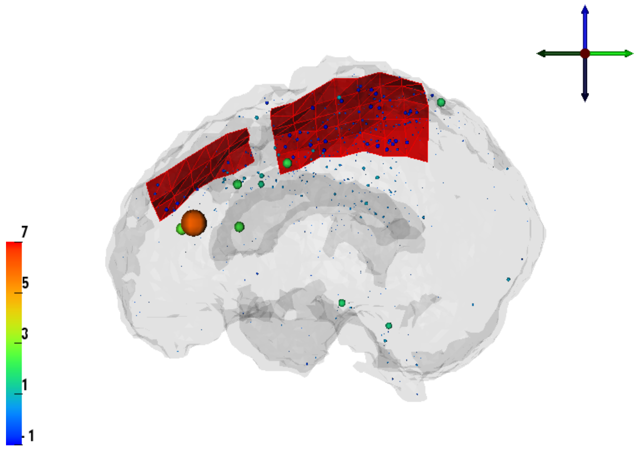

(b) Left side view

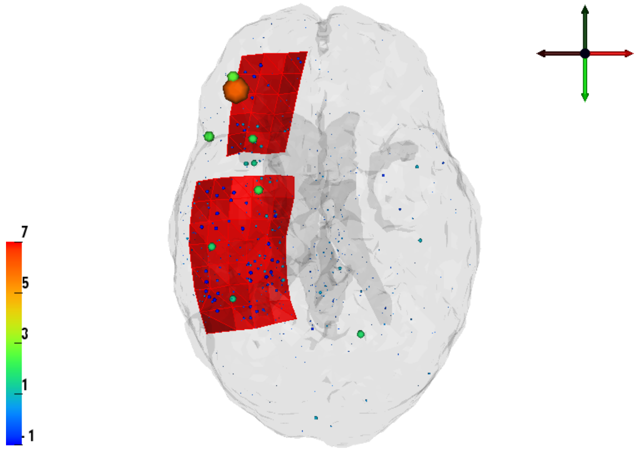

(c) Bottom view

Figure 4.17: Errors in magnitude for the `weak` direction in the whole brain volume. The scale is in nAm.

The errors for the `weak` direction are presented in Figures 4.15 to 4.17. At first glance the spatial error distribution looks quite similar to the `maxerr` series. Also the mean error in Table 4.4 is of the same dimension. The locations which exhibit the biggest angle errors lie clearly in the right hemisphere just below the grid. Differences of 45–60° are focused there, whereas for the rest of the brain volume seems the angle error does not change very much compared to the `strong` direction. For very deep source locations again slightly higher angles of up to 30° occur.

The error distribution for all three modalities is shown in the bottom row of Figure B.7 on Page 103.

	Spatial Error ∅ in mm	**Angle Error** ∅ in °	**Magnitude Error** ∅ in μV
`maxerr`	4.1429 ± 3.8230	6.3577 ± 11.5980	0.0526 ± 0.2771
`strong`	2.9995 ± 2.7503	3.614 ± 6.0093	0.0495 ± 0.2066
`weak`	3.4426 ± 4.0051	4.0166 ± 8.7346	-0.0120 ± 0.2166

Table 4.4: Statistics of the inverse results for the 3172 dipoles placed in the whole brain volume

Errors for dipoles directly below the grid

In order to further evaluate the impact of the plastic sheet on sources directly below it, the volume 2 cm underneath was meshed with a finer constraint and the generated 1959 points were also used for the forward-inverse procedure. The resulting dipole positions are labeled the `volundergrid` dipole series and the three testing directions are presented in Figure B.6 on Page 102.

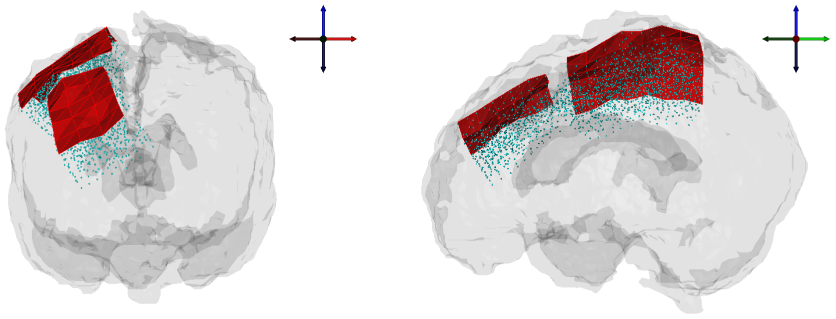

(a) Frontal view (b) Left side view

Figure 4.18: The 1959 dipole positions under the plastic sheet

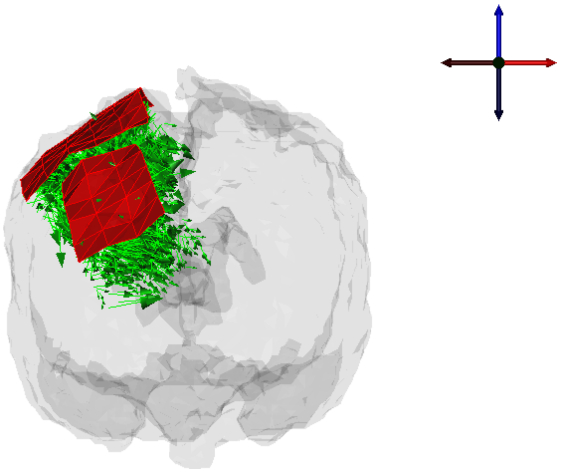

(a) Frontal view

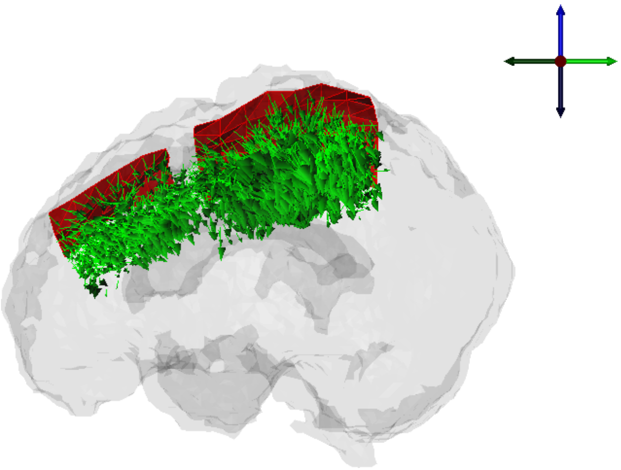

(b) Left side view

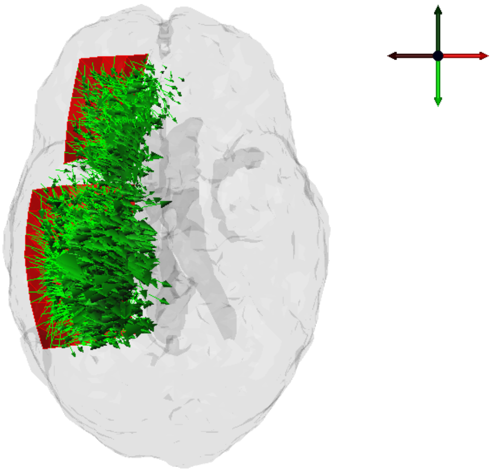

(c) Bottom view

Figure 4.19: Spatial errors for the `maxerr` direction in the volume underneath the grid. The arrows point from the original dipole position to the fitted location.

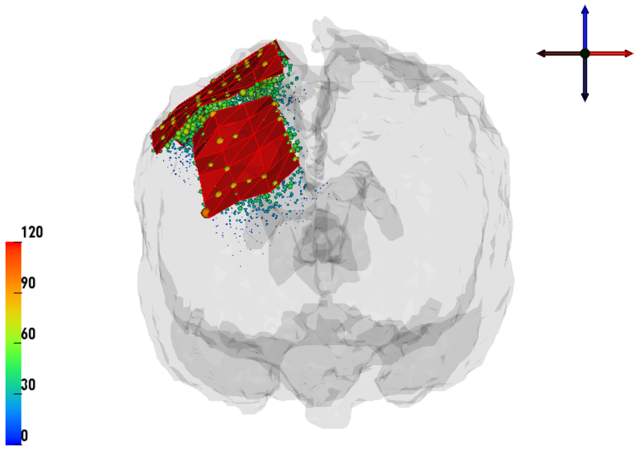

(a) Frontal view

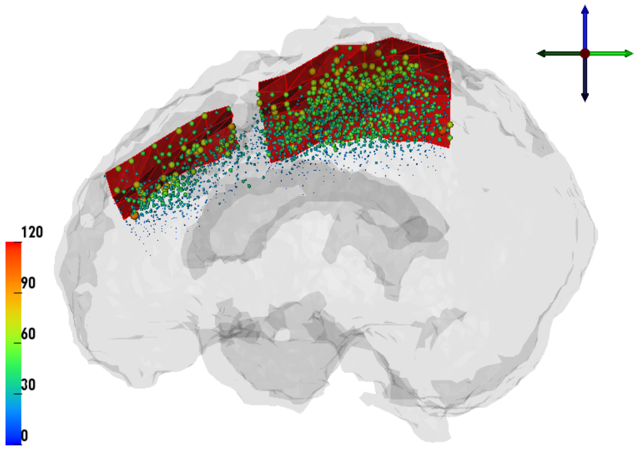

(b) Left side view

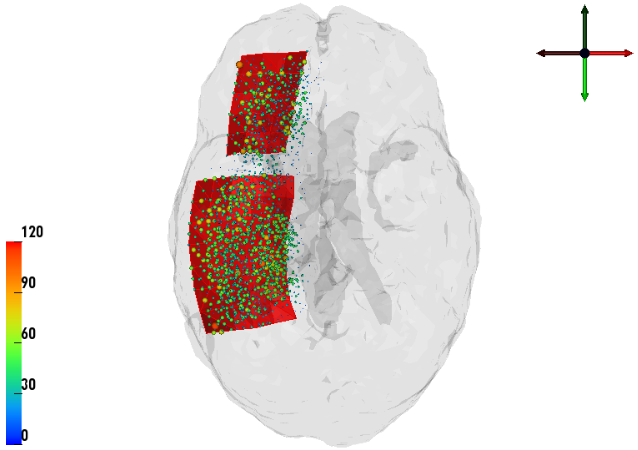

(c) Bottom view

Figure 4.20: Angle errors for the `maxerr` direction in volume underneath the grid. The scale is in °.

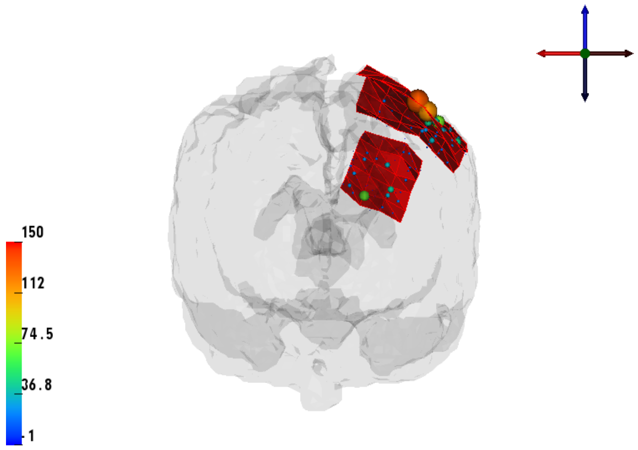

(a) Frontal view

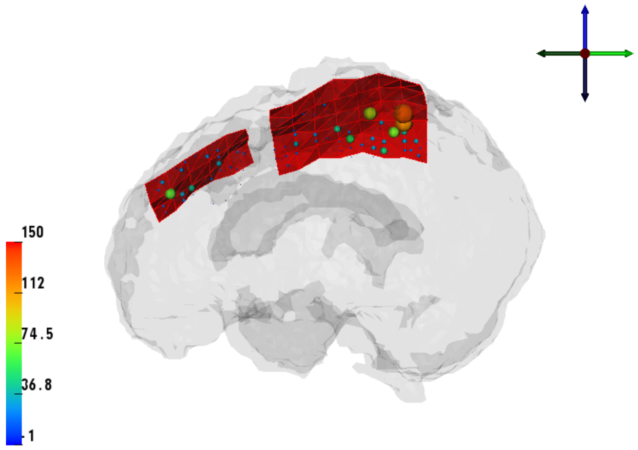

(b) Left side view

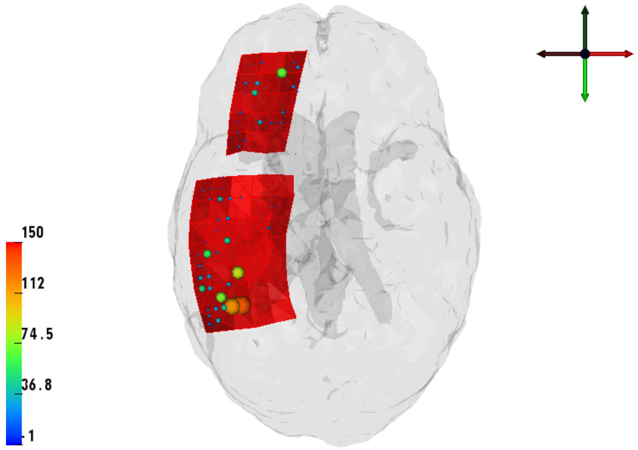

(c) Bottom view

Figure 4.21: Errors in magnitude for the `maxerr` direction in volume underneath the grid. The scale is in nAm.

As before for the `wholebrainvol` series the `maxerr` direction was examined for the `volundergrid` series and the results are presented in Figures 4.19 to 4.21.

The spatial error distribution (see Figure B.8 on Page 104) is quite broad and values from 7.5 mm to 20 mm occur with similar frequencies. It is notable that again the majority of the arrows point away from the grid. For the angle difference the tendency of the `wholebrainvol` trend can be confirmed: close to the grid the difference is as high as 60 to 90°, deeper in the brain it becomes quickly smaller. Errors in magnitude can only be observed for the topmost layer of dipole positions directly beneath the grid. For the other positions a magnitude difference is quasi not existing.

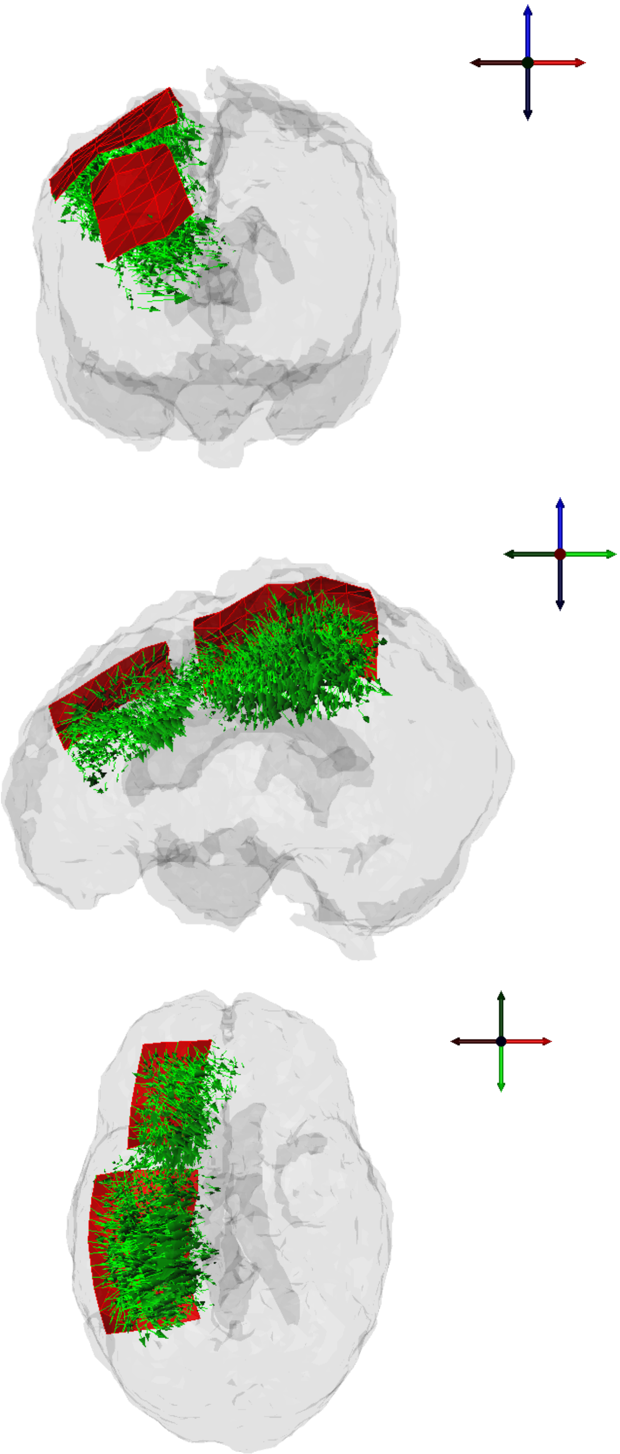

Figure 4.22: Spatial errors for the `strong` direction in the volume underneath the grid. The arrows point from the original dipole position to the fitted location.

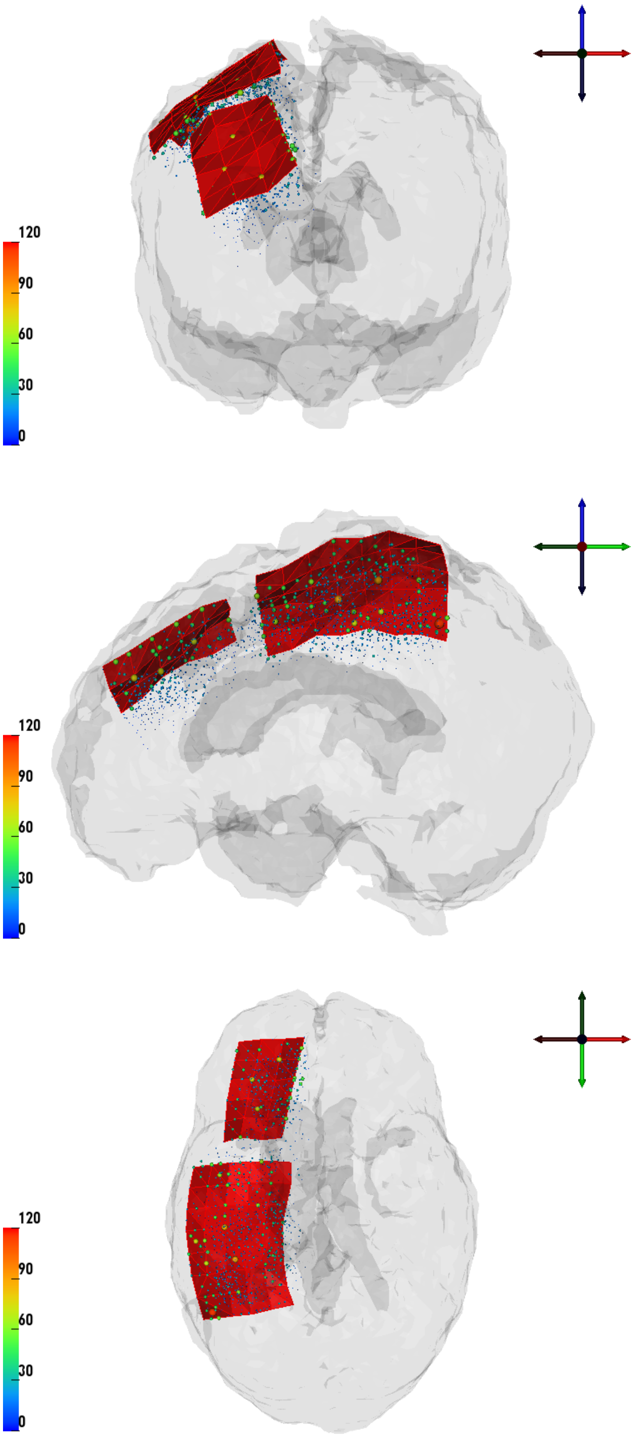

Figure 4.23: Angle errors for the `strong` direction in volume underneath the grid. The scale is in °.

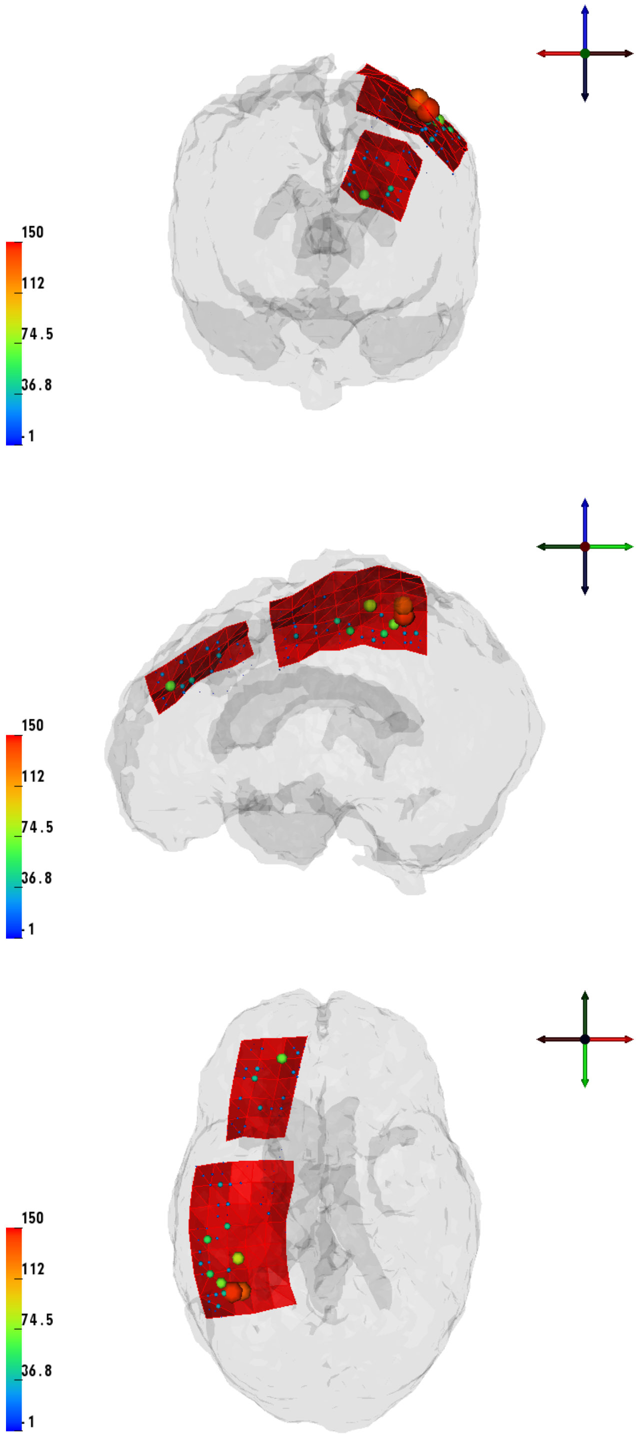

Figure 4.24: Errors in magnitude for the `strong` direction in volume underneath the grid. The scale is in nAm.

For the `strong` direction the errors shown in Figures 4.22 to 4.24 are the smallest of the three also in the `volundergrid` series.

The spatial errors look similarly distributed as for the `maxerr` direction, although smaller in amplitude. The angle error is mostly below 30°and the magnitude error is for nearly all points mostly identical to the one of the `maxerr` direction.

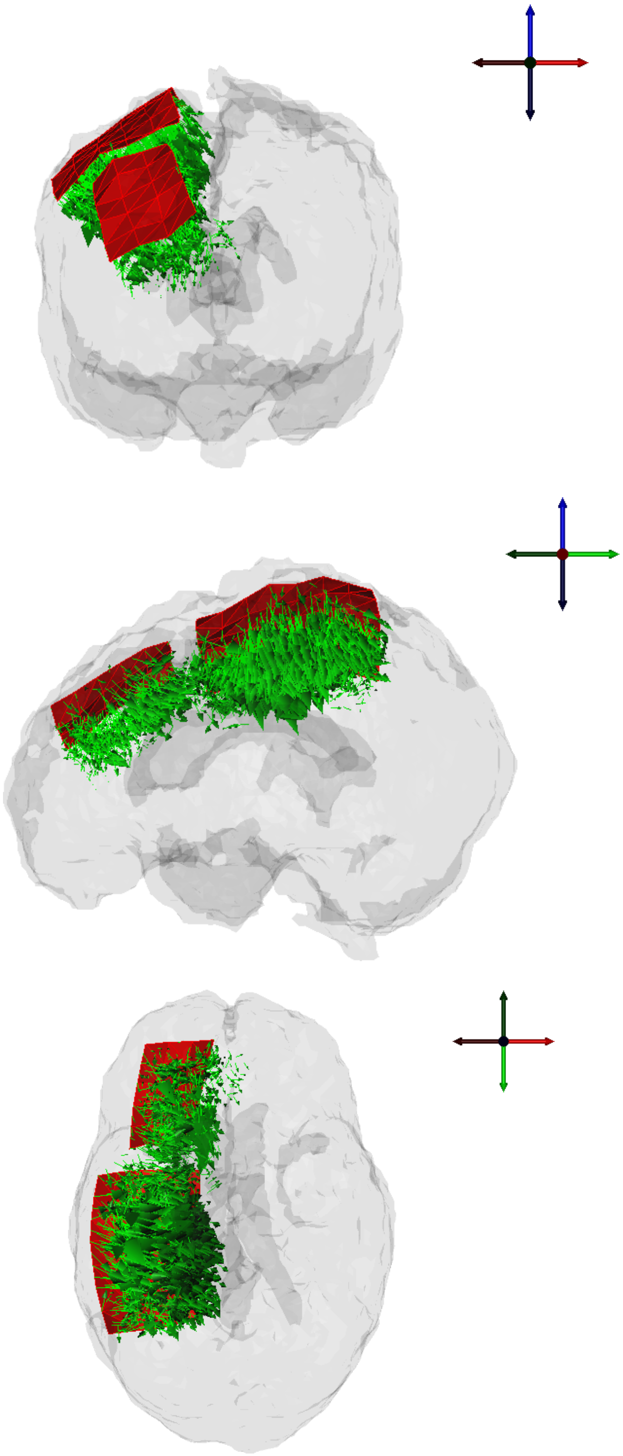

Figure 4.25: Spatial errors for the `weak` direction in the volume underneath the grid. The arrows point from the original dipole position to the fitted location.

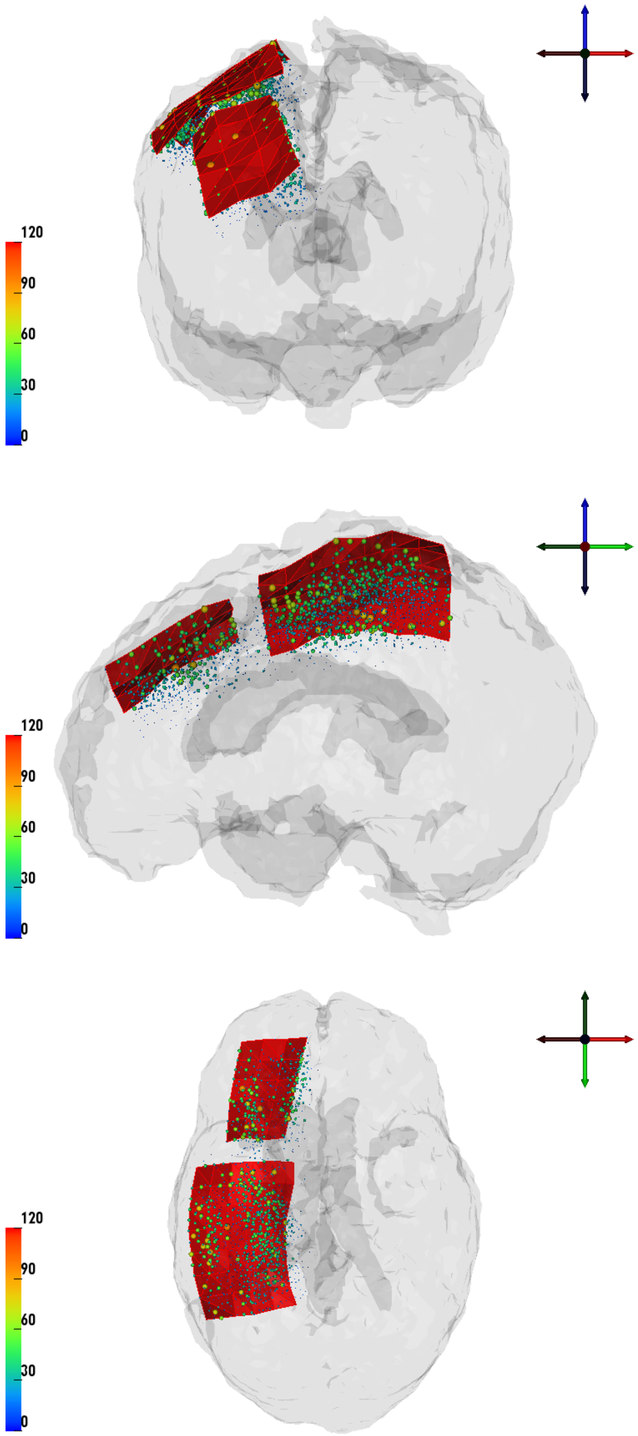

Figure 4.26: Angle errors for the `weak` direction in volume underneath the grid. The scale is in °.

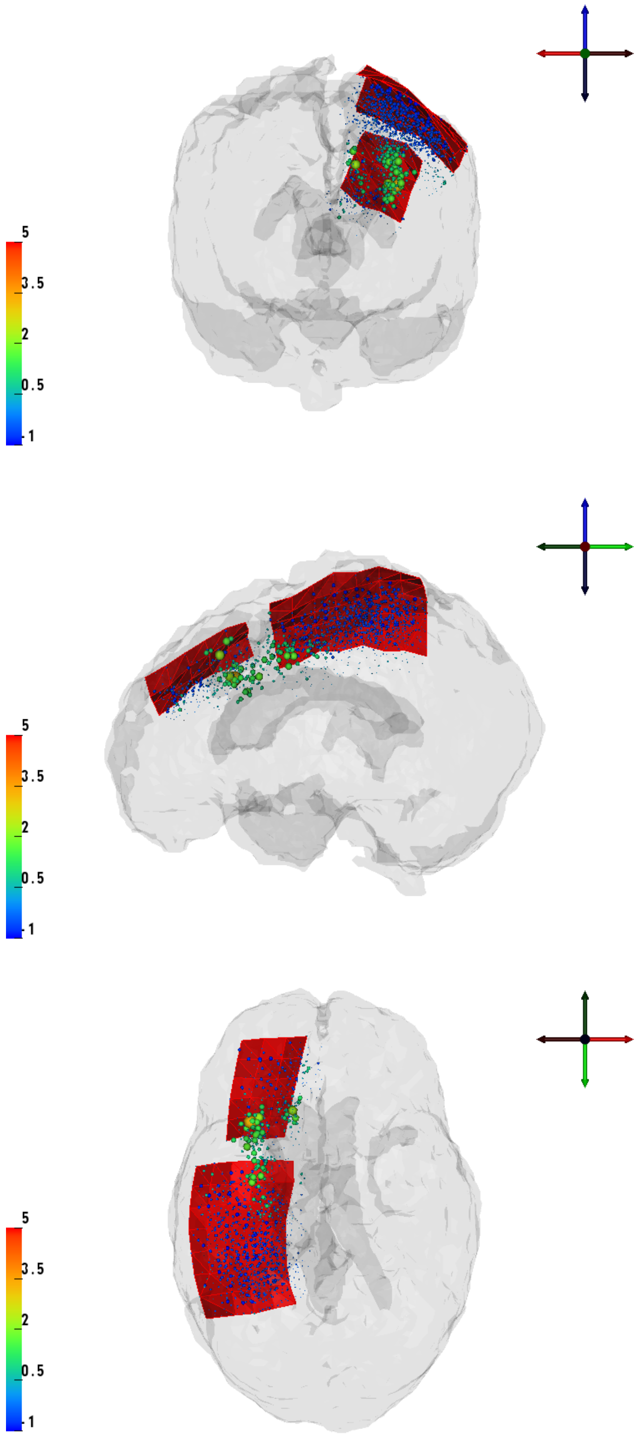

Figure 4.27: Errors in magnitude for the `weak` direction in volume underneath the grid. The scale is in nAm.

The general tendency that was shown for all of the directions is also applicable for the `weak` direction of the `volundergrid` series. As shown for the other two, the spatial error arrows presented in Figure 4.25 also generally point away from the grid and the angle errors in Figure 4.26 are bigger for sources closer to the grid. The magnitude errors in Figure 4.27 however are of higher amplitude than before and especially noticeable is the increase in the volume under the gap between the two parts of the grid. Here even differences of 2 nAm and more are exhibited, which is an error of 200 %.

	Spatial Error ∅ in mm	**Magnitude Error** ∅ in μV	**Angle Error** ∅ in $^\circ$
`maxerr`	13.0920 ± 5.4342	1.0421 ± 6.4726	29.8396 ± 18.1307
`strong`	8.1582 ± 4.4401	1.1459 ± 6.7287	14.1014 ± 11.2328
`weak`	10.9327 ± 6.9110	-0.1195 ± 0.4196	19.9041 ± 15.9477

Table 4.5: Statistics of the inverse results for the 1959 dipoles placed directly below the grid

From the simulations of the `wholebrainvol` and the `volundergrid` dipole series it is evident, that the modeling of the implanted plastic grid has an impact on the potential distribution on the head surface and therefore also on source reconstruction based on the measured signals. Misslocalizations in the dimension of some centimeters and angle differences of up to 90° close to the grid are possible, if the plastic sheet is not considered in realistic head models.

This is reasonable, as the ohmic volume currents, that flow from the active brain areas to the outside measurement sensors, have to flow around the strongly insulating plastic barrier instead of taking the direct way. This blurres and weakens the measured potential at the electrodes, so the potential distribution looks just like one a dipole deeper in the brain would cause if the grid would not be present.

4.6 Source Analysis of Epilepsy Data

After creating the realistic head model of the epilepsy patient it was used to analyze measured data from the subject. For this purpose four 15-minute datasets were recorded during drowsy sleep. These datasets were then subjected to extended infomax ICA (*Independent Component Analysis*, [45]) that incorporated 107 channels (29 scalp EEG, 78 iEEG). Each decomposition returned 107 maximally independent components across the data.

The FEM was then applied to localize the source of the highly dipolar peri-ictal IC1-component (see Figure 4.28).

4.6.1 Model

To model the real situation as closely as possible of course the model with implanted grid was used for source localization. As starting points for the simplex optimization

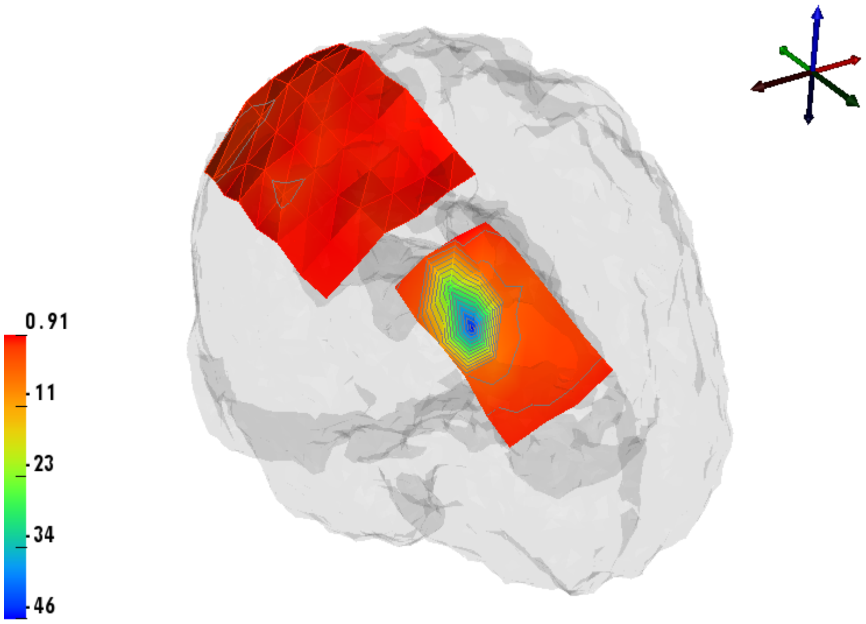

(a) The measured iEEG potential distribution

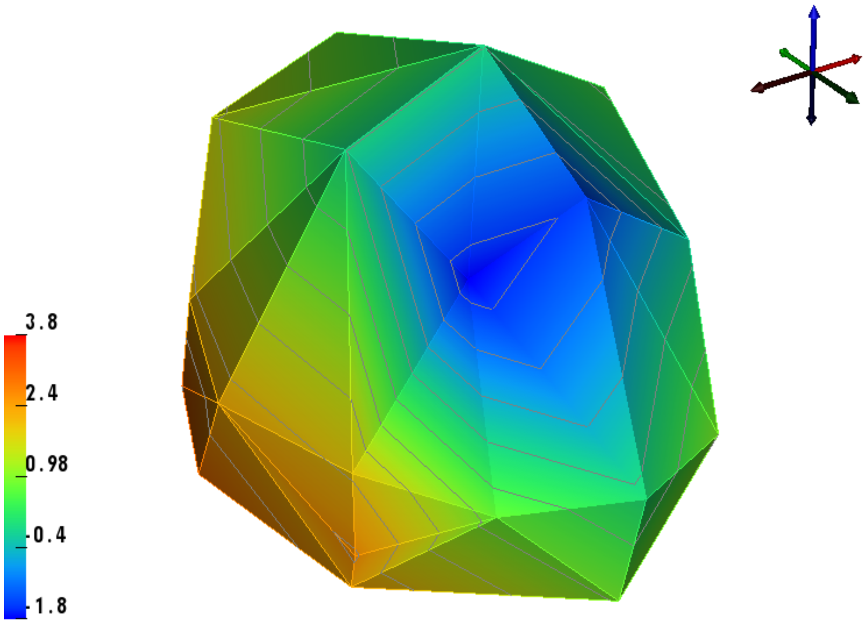

(b) The measured sEEG potential distribution

Figure 4.28: The measured IC1 component on the iEEG and sEEG electrodes (scales are μV)

procedure again the sixteen seed points of Figure 4.7 were used.

4.6.2 Results

The localization results of a dipole fit procedure using the same seedpoints as in the grid error studies (see Figure 4.7) are shown in Figure 4.29. The arrow with the number 0 represents the solution that derives from taking only the iEEG electrode data into account. It is localized at (96.89/62.38/166.78) mm. Using only the sEEG signal results in a dipole at position 1, (129.15/87.66/145.75) mm. Both modalities in combination yield the solution 2 at (100.65/61.85/169.70) mm.

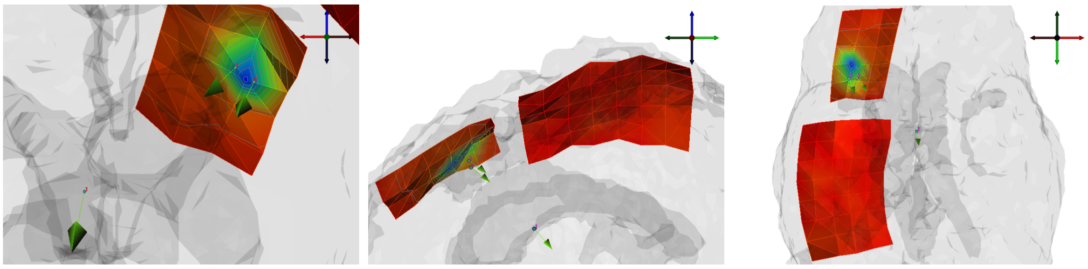

Figure 4.29: Reconstructed dipole positions for iEEG data only (0), sEEg data only (1) and both (2)

The dipoles number 0 and 2 are close to the grid and in the very neighborhood of the peaking iEEG electrode. Their distance is about 4.8 mm. The sEEG fit (arrow number 1) however is localized more than 4 cm deeper in the brain.

	Goodness of Fit	**#Iterations**
`iEEG` only	98.8247 %	248
`sEEG` only	93.5572 %	749
both `sEEG` and `iEEG`	95.3249 %	774

Table 4.6: Results of the dipole fit

Although at least the reconstructed dipole directions for iEEG and sEEG data look quite similar, the spatial distance of both dipole solutions is unexpected. The *goodness of fit (GOF)* for the sEEG-fitted dipole is about 5 % less than the GOF for the iEEG-result (see Table 4.6.

The iEEG fit result lies directly under the grid. As seen in Section 4.5.2 if the grid is not modeled for source reconstruction but was present for the forward calculation, a source in that region would be localized deeper in the brain. But as the dipole fitting was performed in the model with the plastic sheet, both inverse results should have been nearly the same. Therefore the grid, although it has undeniably an influence on the source localization for the brain volume underneath, is not the direct reason for the misslocalization.

A further reason for the fact, that the source is fitted close to the grid if both modalities are used for the reconstruction is the amplitude difference of the two signals. While the sEEG potential distribution has a maximal value of about 4 μV, the grids peak is at -46 μV. Therefore fitting the source close to the grid explains a greater variance (see Table 4.6.

In [5], the same IC1-component was analyzed without modeling the plastic sheet. For the sEEG-based result the same discrepancy was found and the iEEG-based localization was also close to the grid (though for certain seedpoints even above the plastic sheet, whereas in this study the sources were localized below it in all cases).

The results of this study as well as the previous simulations without grid modeling suggest, that the assumption, that the underlying source distribution of iEEG and sEEG is identical in simultaneous iEEG/sEEG-ICA has to be challenged.

A weak signal-to-noise ratio might be a further source of errors, because the sEEG electrodes have to be arranged on the pressure bandage covering the implantation wound, which might spoil the sEEG signals.

Lastly more accurate modeling by segmenting e. g. the skull into more layers (spongiosa and compacta, see Section 3.1.2) or differentiating between gray and anisotropic white matter in the brain compartment might also help decrease the errors. However further investigation is necessary to see if this really is the case.

5 Conclusion

In this thesis the use of the finite element method (FEM) on source reconstruction was first validated in multilayer sphere models and then applied to a realistic head model of an epilepsy patient who had a very strongly insulating plastic sheet with iEEG electrodes implanted for intracranial monitoring.

The multilayer sphere studies in Chapter 3 showed that the FEM solutions of the forward problem converge towards the analytical solution with decreasing mesh size h. Using the full subtraction approach the errors are generally very low. Refining certain compartments of the model with a finer volume constraint for the generated tetrahedra can increase the numerical accuracy of the forward solution. If at all possible preferably all compartments should be refined with a tight volume constraint to get the best numerical results. To reduce computational complexity without loosing too much accuracy the first step is not to constrain the inner brain compartment but keep the outer layers fine. Should for any reason no more than one layer be refined, constraining the tetrahedra volume of the skull compartment proved best for isotropic four layer sphere models.

The software TetGen is capable of generating very high quality tetrahedra meshes from given triangulated surfaces. It however demands that these surfaces do not intersect each other, a requirement that can not always be met when dealing with realistic head models that base on patients' individual CT and MRI data.

Using the transfer matrix method in combination with the Venant dipole approach acceptable computation times are achievable. Once the transfer matrix is computed and stored, a forward calculation reduces to some milliseconds on a normal desktop PC. The matrices can also be saved and reused for later computations with the same model.

With the FEM it is possible to model a very thin iEEG plastic sheet, that patients with medically intractable epilepsy get implanted for intracranial monitoring routinely nowadays, as described in Chapter 4. As the whole sheet is only 0.127 mm thick it requires a very fine mesh resolution. Once a closed surface of this sheet exists, meshing it with TetGen results in quality mesh, that needs to be embedded in the suspect's head model. This proved to be a difficulty as TetGen requires closed, non-intersecting surfaces (see above). Therefore an alternative approach of point-adding and labeling was applied (see Section 4.2.1).

Generally the construction of realistic head models with tetrahedra from registered and segmented image data is possible, but can become difficult in cases of skull trepanation holes or other irregularities. A way to skip this mesh generation part would be to apply hexahedral finite elements and simply use each MR voxel as hexahedron. The sub-millimeter resolution of modern MRI scanners can lead to high quality volume conductor models and the time consuming labeling step could be omitted. However modeling such complex geometries as the implanted plastic sheet with hexahedra might prove very difficult.

Finally applying the FEM to realistic data measured in the epilepsy patient yielded not quite the expected result. Using just the iEEG signal to reconstruct a very dipolar pattern resulted in a dipolar current source directly below the grid. But reconstructing the position only from the sEEG signal leads to a localization about 4 cm deeper in the brain compartment.

This however resonates with the findings of an earlier study[5] were the grid was not modeled at all. Therefore the assumption that the underlying source distribution of iEEG and sEEG is identical in simultaneous iEEG/sEEG-ICA has to be challenged.

Another source of localization errors might result from the weak signal-to-noise ratio, that relates to the pressure bandage covering the iEEG sheet, which might have spoiled the sEEG electrodes' signal.

Furthermore improving the realistic head model e. g. by modeling the skull anatomically correct as three-layered compartment or by distinguishing between isotropic gray and anisotropic white matter in the brain layer could lead to smaller localization errors for sEEG-only-based source reconstruction.

The FEM is the method of choice for this kind of numerics, because of its ability to model such complex geometries and anisotropic conductivities. Using the transfer matrix approach yields acceptable computation times that make the FEM a valuable tool also for clinical routine.

A Methods and Algorithms

A.1 The shifting algorithm

To generate a closed surface suitable for meshing with TetGen from the original electrode data the following algorithm was applied (see Figure A.1):

1. Calculate the surface normal $\boldsymbol{n}_i$ for each triangle t_i
2. For each node calculate the average of the normals of the triangles the node is part of:
$$\boldsymbol{n}_{\text{avg}} = \frac{1}{\#t_i} \sum_{\boldsymbol{x}_i \in t_i} \boldsymbol{n}_i \tag{A.1}$$
3. Add a new point: $\tilde{\boldsymbol{x}} = \boldsymbol{x} + f \cdot \boldsymbol{n}_{\text{avg}}$, where f is the length the point will be projected on in $\boldsymbol{n}_{\text{avg}}$-direction
4. For each triangle t_i define new triangle $\tilde{t}_i$ consisting of the corresponding new vertices
5. Connect the two surfaces s and $\tilde{s}$ by adding appropriate "wall" triangles
6. Make sure all triangles have the correct orientation (i. e. the surface normal points outwards) by sorting the nodes accordingly

A.2 The labeling algorithm

The solid angle Ω of an object with regard to a viewpoint $\boldsymbol{V}$ is defined as the ratio of the area S of the object projected onto the surface of a sphere around $\boldsymbol{V}$ and the radius r of that sphere, i. e.

$$\Omega = \frac{S}{r}. \tag{A.2}$$

For a triangle it can be efficiently calculated as ([46])

$$\tan\left(\frac{1}{2}\Omega\right) = \frac{[\boldsymbol{R}_1 \boldsymbol{R}_2 \boldsymbol{R}_3]}{R_1 R_2 R_3 + (\boldsymbol{R}_1 \cdot \boldsymbol{R}_2) R_3 + (\boldsymbol{R}_1 \cdot \boldsymbol{R}_3) R_2 + (\boldsymbol{R}_2 \cdot \boldsymbol{R}_3) R_1}, \tag{A.3}$$

where for $i \in \{1, 2, 3\}$ the $\boldsymbol{R}_i$ denote the position vectors of the triangle corner points. If a point P lies inside a closed surface consisting of triangles, it holds that

$$\sum_{t_i} \Omega_i = 4\pi. \tag{A.4}$$

Therefore one can apply the following algorithm to decide whether a given tetrahedron identified by its barycenter $\boldsymbol{B}$ lies inside or outside a closed triangulated surface s.

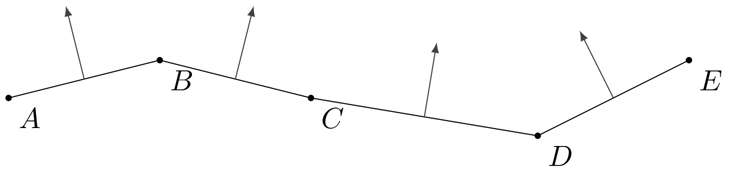

(a) Calculate surface normals

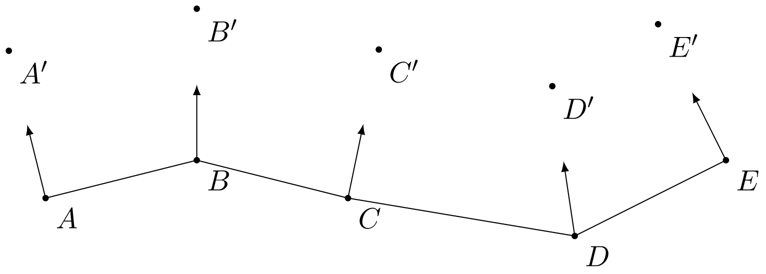

(b) Shift vertices in average surface normal direction

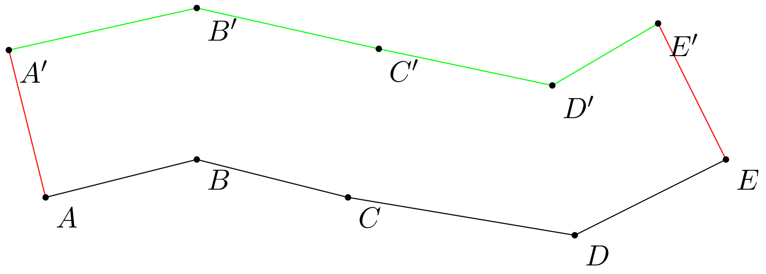

(c) Connect old (black) and new (green) surfaces by ’wall’ elements (red)

Figure A.1: Shifting process (for simplification in 2-d)

1. Calculate the barycenter $\boldsymbol{B}$ of the tetrahedron $\boldsymbol{S}$
2. For each triangle of the surface calculate the solid angle Ω_i regarding $\boldsymbol{S}$
3. If $\sum \Omega_i = 4\pi$ then $\boldsymbol{B}$ lies inside s

With this algorithm it is now possible to successively assign material labels to tetrahedra according to a given surface. As every tetrahedron inside the surface is labeled, one must start with the outmost surface (in this case, the outer skull surface) and continue inwards with the inner skull, the brain and the plastic sheet surfaces.

B Additional Figures

B.1 Multilayer Sphere Studies

On the following pages some additional figures are listed that thematically belong to Chapter 3.

First the remaining meshes of Group 1 are presented in Figure B.1. These are the eight meshes with two refined compartments and the four with only one unrefined layer.

Figure B.2 shows the RDM and MAG values of Group 1's meshes for all eccentricities. To better distinguish the different models Figure B.3 zooms into the last five eccentricities. A better overview of the overall error is given by presenting the RE in Figure B.4.

Two refined compartments

`fineskull-skin` `fineskull-skin*` `fineCSF-skull` `finebrain-skull`

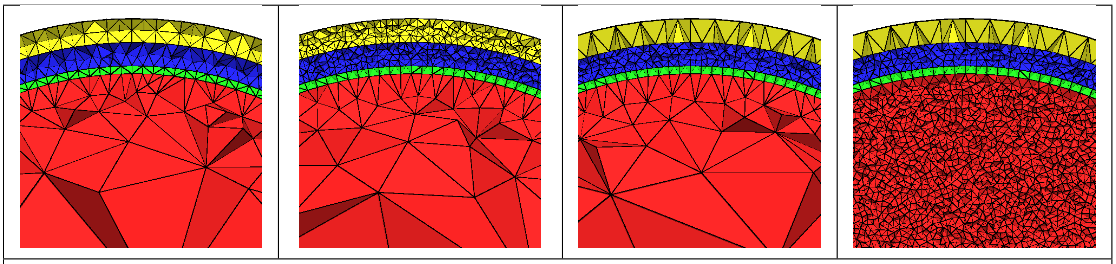

Two refined compartments

`fineCSF-skin` `fineCSF-skin*` `finebrain-skin` `finebrain-CSF`

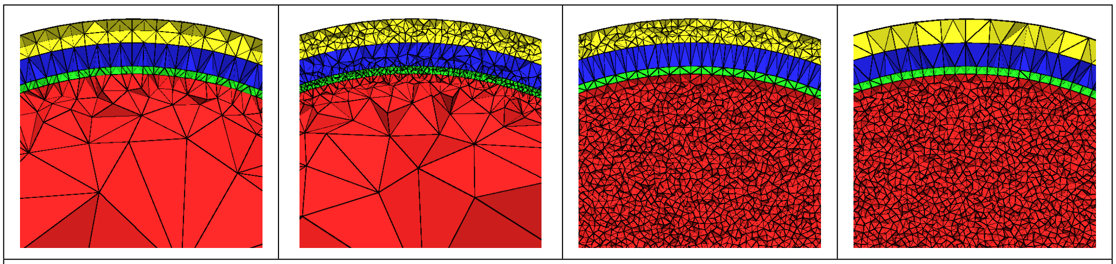

Three refined compartments

`fineCSF-skull-skin` `finebrain-skull-skin` `finebrain-CSF-skin` `finebrain-CSF-skull`

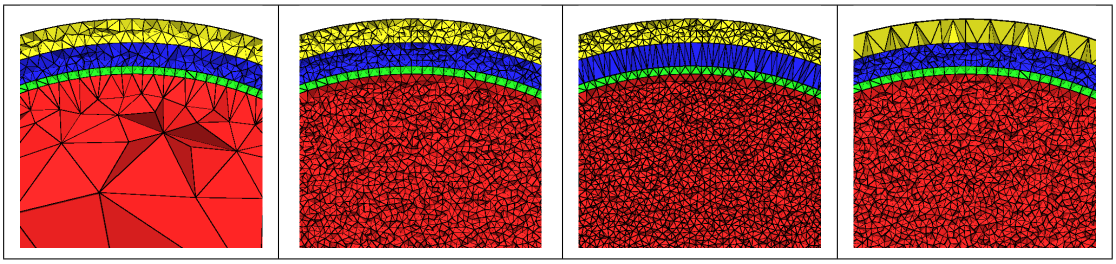

Figure B.1: Cross-sections of the remaining 12 tetrahedral meshes with different volume constraints of Group 1. The corresponding parametrizations of the models are shown in Table 3.2

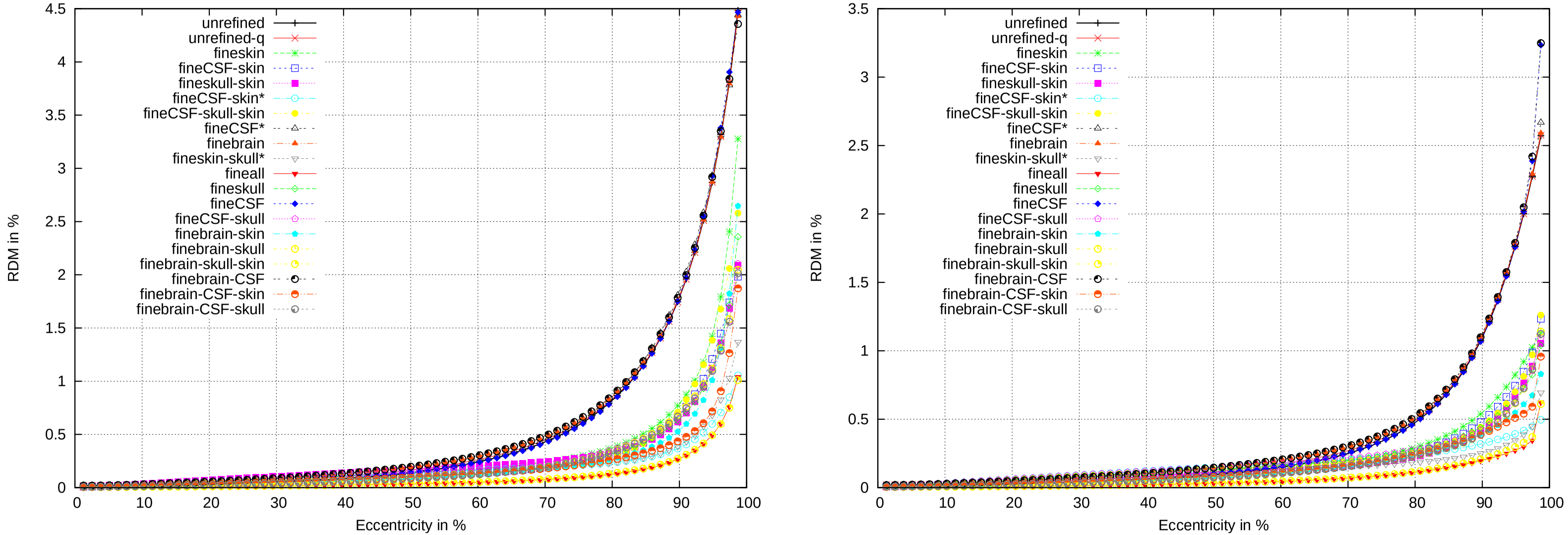

(a) Radial Direction (b) Tangential Direction

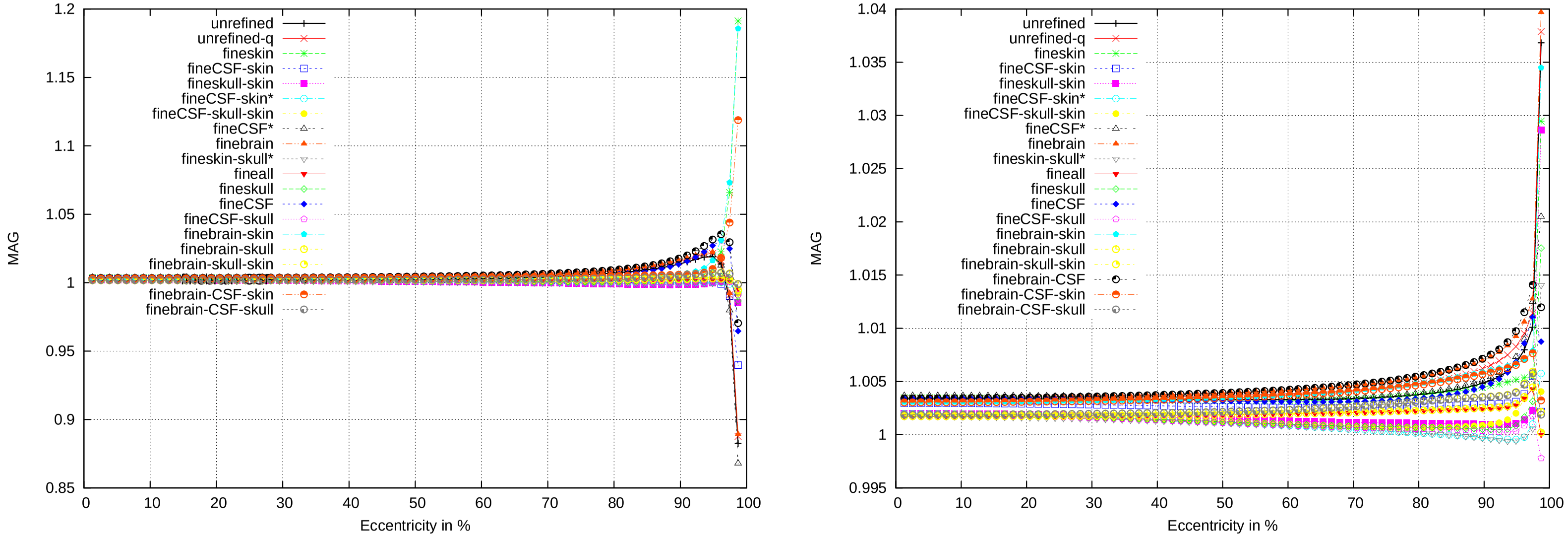

(c) Radial Direction (d) Tangential Direction

Figure B.2: RDM and MAG for every tetrahedra model shown in Table 3.2 in chapter 3

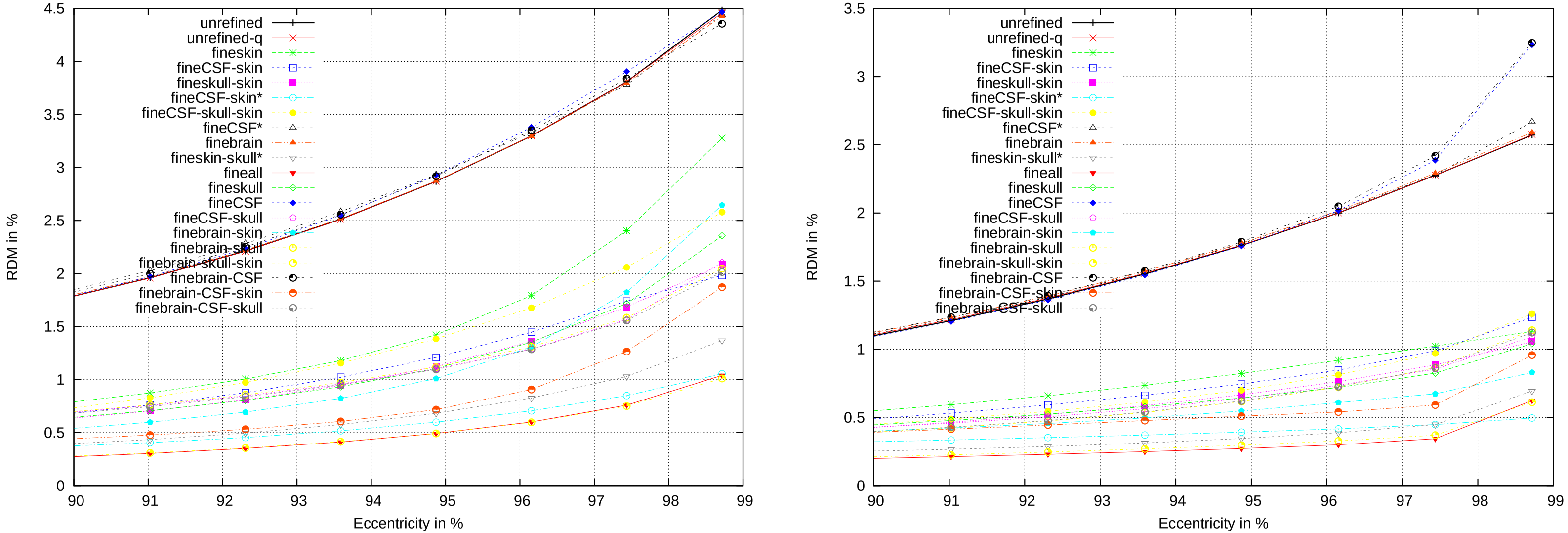

(a) Radial Direction (b) Tangential Direction

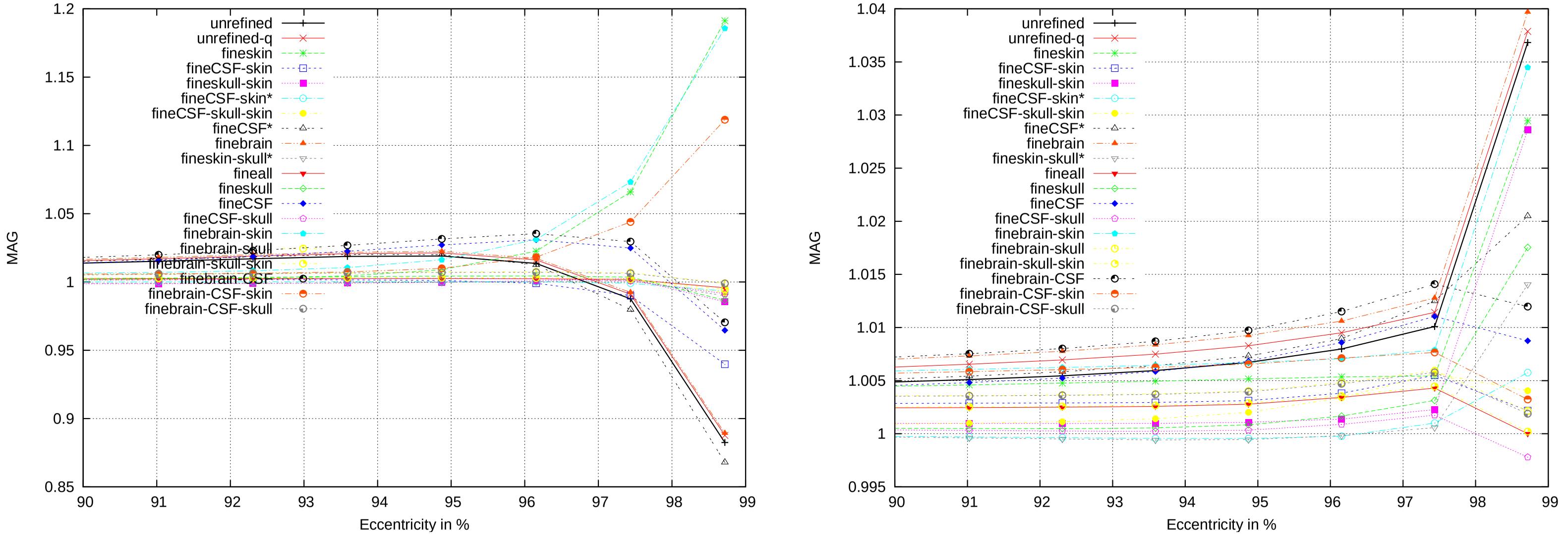

(c) Radial Direction (d) Tangential Direction

Figure B.3: RDM and MAG for every tetrahedra model shown in Table 3.2 in chapter 3 for eccentricities greater than 90 %

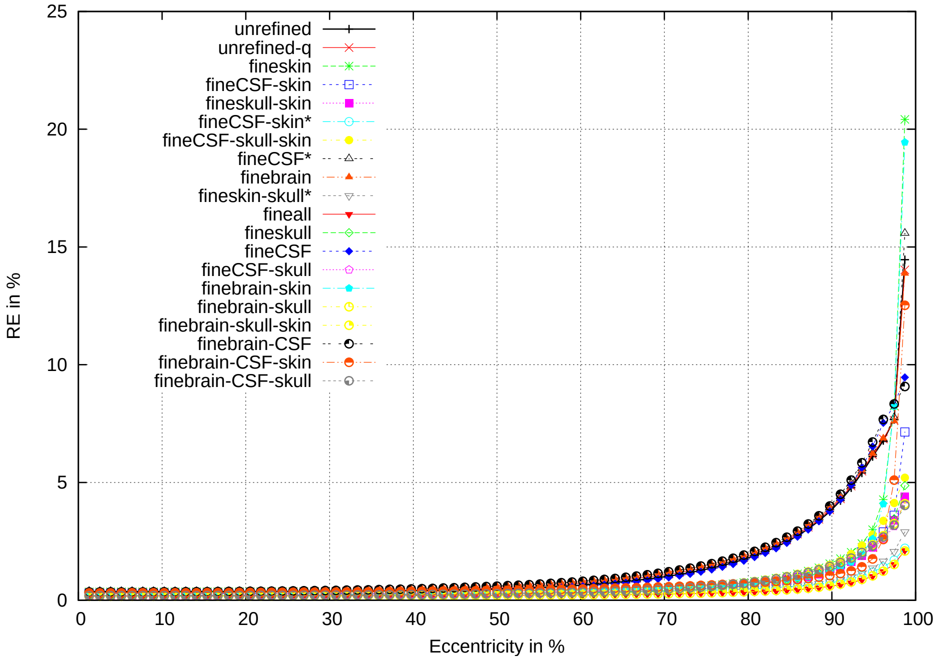

(a) Radial direction

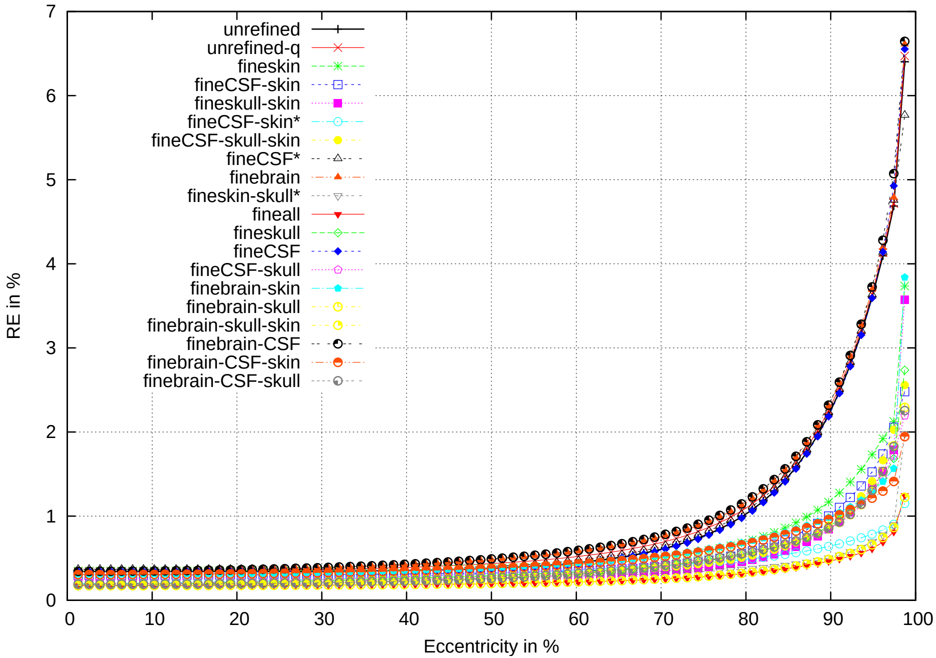

(b) Tangential direction

Figure B.4: RE for every tetrahedra model shown in Table 3.2 in chapter 3

B.2 Epilepsy Patient's Head Model

B.2.1 Directions

In Section 4.5.2 three directions called `maxerr`, `strong` and `weak` were defined for each source location in the epilepsy patient's head model. These are visualized in Figure B.5 for the `wholebrainvol` series and in Figure B.6 for the `volundergrid` dipole series.

Particularly the `volundergrid` series shows the influence of the grid. It is notable, that most arrows for the `maxerr` direction point towards the mid of the grid, which is explainable by the definition of the direction. As it points into the direction, that produces the biggest difference between forward solutions with and without grid, it is reasonable for locations below the grid, that dipoles pointing towards the middle of the sheet will produce the biggest differences. Because for such directions, the impressed primary currents point directly towards a strong insulator which causes the ohmic return currents to blur much more than for sources pointing directly to a measurement electrode.

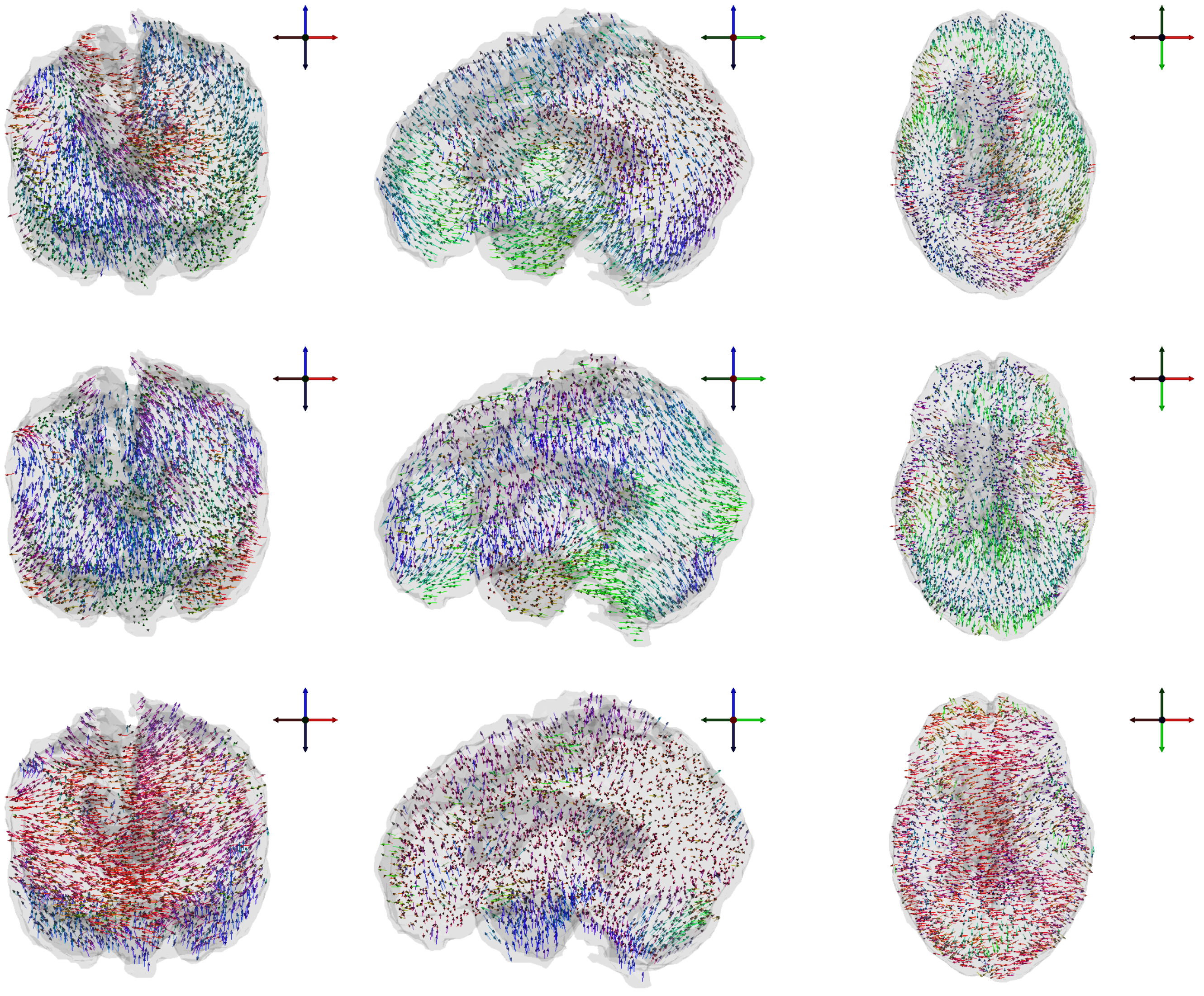

Figure B.5: The three directions `maxerr` (upper row), `strong` (middle row) and `weak` (bottom row) for the `wholebrainvol` dipole series in frontal (left column), sagittal (middle column) and transversal view (right column). The x, y and z direction of the arrows is color-coded

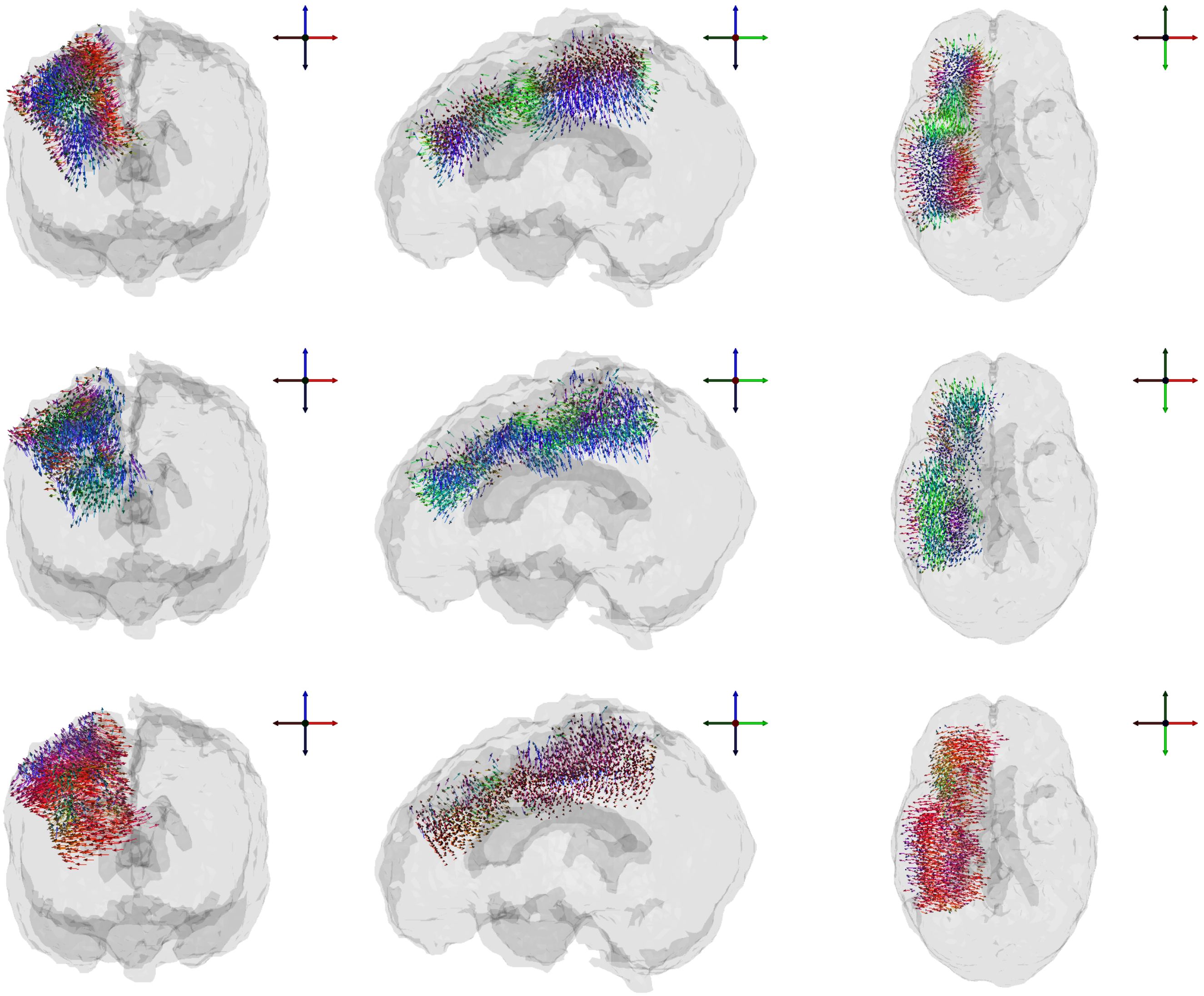

Figure B.6: The three directions `maxerr` (upper row), `strong` (middle row) and `weak` (bottom row) for the `volundergrid` dipole series in frontal (left column), sagittal (middle column) and transversal view (right column). The x, y and z direction of the arrows is color-coded

B.2.2 Error Statistics

To shed further light on the error statistics for the realistic head model of the epilepsy patient the error distribution of all three types of errors defined in Section 4.4 for the three directions is plotted for the `wholebrainvol` series in Figure B.7.

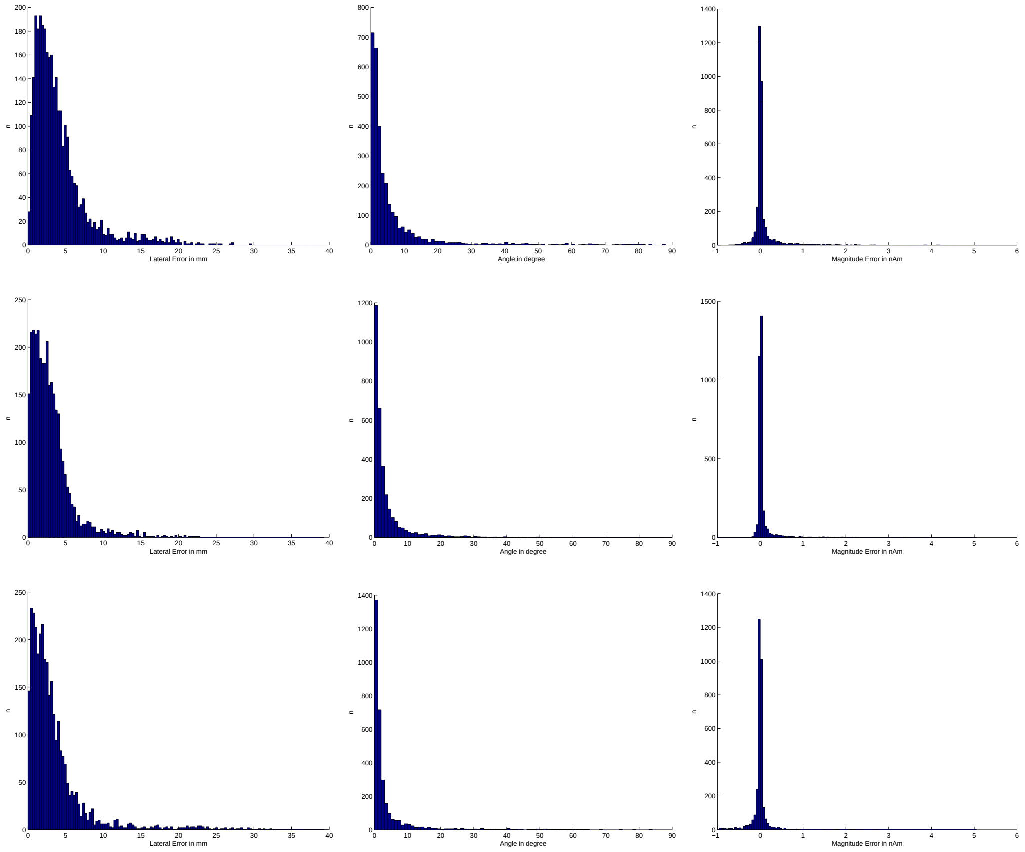

Figure B.7: Error distribution of the `wholebrainvol` dipole series for the *maxerr* (top row), *strong* (middle row) and *weak* direction (bottom row)

The spatial error is below 5 mm for at least 74 % (in the case of the `maxerr`-direction) of the test locations (see Table B.1).

Direction	**Lat. Error < 5 mm**	**Angle $< 20\ °$**	**Magn. Diff. < 1 nAm**
`maxerr`	74.1 %	93.3 %	98.2 %
`strong`	86.0 %	96.8 %	98.8 %
`weak`	82.6 %	95.5 %	99.7 %

Table B.1: Error distribution statistics for the `wholebrainvol` dipole series

Figure B.8 shows the same statistics for the `volundergrid` dipole series in the volume under the grid.

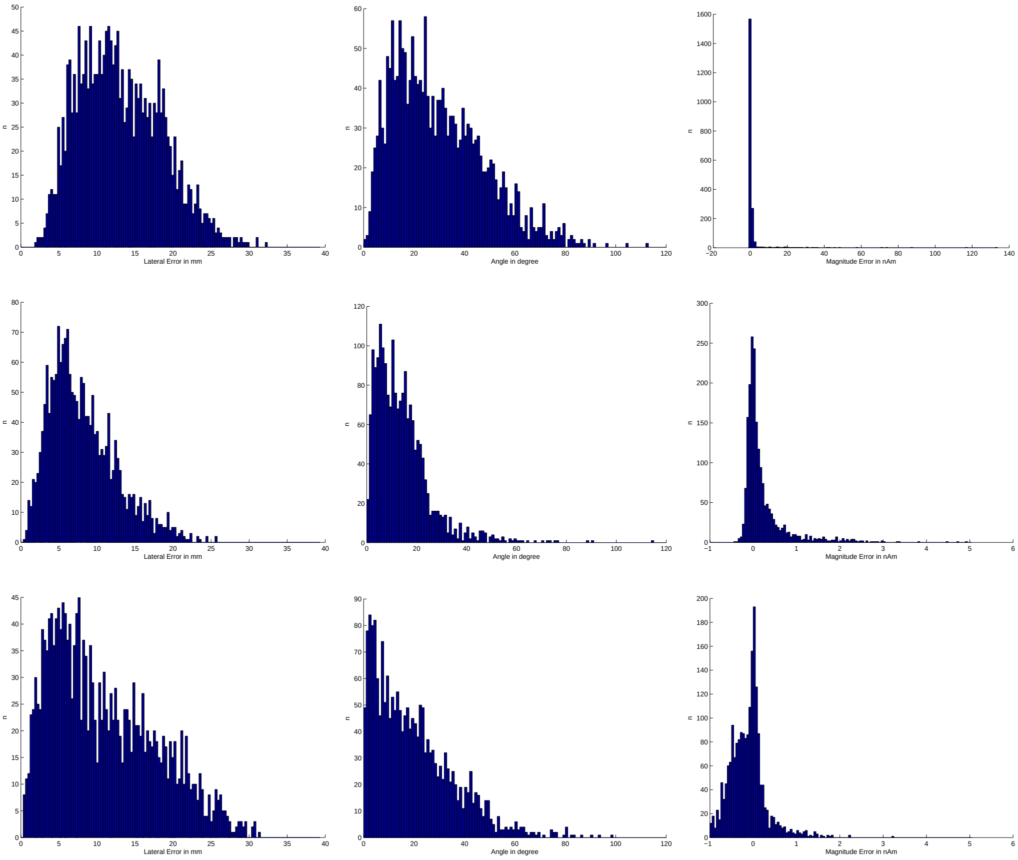

Figure B.8: Error distribution of the `volundergrid` dipole series for the *maxerr* (top row), *strong* (middle row) and *weak* direction (bottom row)

The error distribution for the `volundergrid` dipole series is for all directions much broader und reaches to higher error values than the `wholebrainvol` distribution. Table B.2 also illustrates this, as particularly the spatial errors are much worse than for the `wholebrainvol` series. This once again emphasizes the importance of modeling electrode grids made from strong insulating materials when constructing realistic head models.

Direction	**Lat. Error < 5 mm**	**Angle < 20 °**	**Magn. Diff. < 1 nAm**
`maxerr`	4.0 %	36.0 %	87.7 %
`strong`	26.8 %	78.5 %	89.1 %
`weak`	23.5 %	57.9 %	97.6 %

Table B.2: Error distribution statistics for the `volundergrid` dipole series

Bibliography

[1] Lew, S. ; Wolters, C. ; Dierkes, T. ; Röer, C. ; MacLeod, R.: Accuracy and run-time comparison for different potential approaches and iterative solvers in finite element method based EEG source analysis. In: *Applied Numerical Mathematics* (2008). – in review

[2] Berger, H.: Über das Elektrenkephalogramm des Menschen. In: *Arch Psychiatr Nervenkr* 87 (1929), S. 527–570

[3] Cohen, D.: Magnetoencephalography: Evidence of Magnetic Fields Produced by Alpha-Rhythm Currents. In: *Science* 161 (1968), Nr. 3843, S. 784–786

[4] Cohen, D.: Magnetoencephalography: Detection of the Brain's Electrical Activity with a Superconducting Magnetometer. In: *Science* 175 (1972), Nr. 4022, S. 664–666

[5] Makeig, S. ; Worrell, G. ; Johnson, C. ; Buchanan, R. ; Wolters, C.: *BISTI Grant Application of 2004*. – Unpublished

[6] 2000-2003. – SimBio: A Generic Environment for Bio-Numerical Simulation, IST-Program of the European Commission, Project No.10378, http://www.simbio.de.

[7] 2002. – Problem Solving Environment for modeling, simulation, and visualization of bioelectric fields. Scientific Computing and Imaging Institute (SCI), http://software.sci.utah.edu/biopse.html.

[8] Noback, C. (Ed.) ; Ruggiero, D. (Ed.) ; Demarest, R. (Ed.) ; Strominger, N. E. (Ed.): *The Human Nervous System*. Springer, 2007

[9] Surveillance, U. N. C. I.: *Anatomy and Physiology*. Epidemiology and End Results (SEER) Program, `http://training.seer.cancer.gov/module_anatomy/unit5_2_nerve_tissue.html`

[10] Hodgkin, A. L. ; Huxley, A. F.: A quantitative description of membrane current and its application to conduction and excitation in nerve. In: *J Physiol* 117 (1952), Aug, Nr. 4, S. 500–544

[11] Murakami, S. ; Okada, Y.: Contributions of principal neocortical neurons to magnetoencephalography and electroencephalography signals. In: *The Journal of Physiology* 575 (2006), Nr. 3, S. 925–936

[12] Schwan, H. ; Kay, C.: The Conductivity of Living Tissues. In: *Annals of the New York Academy of Sciences* 65 (1957), Nr. 6 The Electophysiology of the Heart, S. 1007–1013

[13] Munck, J. de: The potential distribution in a layered anisotropic spheroidal volume conductor. In: *Journal of Applied Physics* 64 (1988), July, Nr. 2, S. 464–470

[14] Munck, J. de ; Peters, M.: A fast method to compute the potential in the multisphere model. In: *Biomedical Engineering, IEEE Transactions on* 40 (1993), Nr. 11, S. 1166–1174

[15] Akhtari, M. ; Bryant, H. C. ; Mamelak, A. N. ; Flynn, E. R. ; Heller, L. ; Shih, J. J. ; Mandelkern, M. ; Matlachov, A. ; Ranken, D. M. ; Best, E. D. ; DiMauro, M. A. ; Lee, R. R. ; Sutherling, W. W.: Conductivities of three-layer live human skull. In: *Brain Topogr* 14 (2002), Nr. 3, S. 151–167

[16] Schwarz, H. R.: *Methode der finiten Elemente.* Teubner Verlag, Stuttgart, 1991

[17] Wolters, C. H. ; Kuhn, M. ; Anwander, A. ; Reitzinger, S.: A parallel algebraic multigrid solver for finite element method based source localization in the human brain. In: *Comp. Vis. Sci.* 5 (2002), Nr. 3, S. 165–177

[18] 2000-2005. – A parallel MPI-based C++ class structured code for fast high-resolution EEG and MEG forward modeling. A. Anwander and C.H. Wolters [6].

[19] Buchner, H. ; Knoll, G. ; Fuchs, M. ; Rienäcker, A. ; Beckmann, R. ; Wagner, M. ; Silny, J. ; Pesch, J.: Inverse localization of electric dipole current sources in finite element models of the human head. In: *Electroencephalogr Clin Neurophysiol* 102 (1997), Apr, Nr. 4, S. 267–278

[20] Wolters, C. H. ; Köstler, H. ; Möller, C. ; Härtlein, J. ; Grasedyck, L. ; Hackbusch, W.: Numerical mathematics of the subtraction method for the modeling of a current dipole in EEG source reconstruction using finite element head models. In: *SIAM J. on Scientific Computing* 30 (2007), Nr. 1, S. 24–45

[21] Drechsler, F. ; Wolters, C. H. ; Dierkes, T. ; Si, H. ; Grasedyck, L.: A highly accurate full subtraction approach for dipole modelling in EEG source analysis using the finite element method. In: *Applied Numerical Mathematics* (2008). – in review

[22] Nelder, J. ; Mead, R.: A simplex method for function minimisation. In: *Computer J.* 7 (1965), S. 308–313

[23] Si, H.: TetGen – A Quality Tetrahedral Mesh Generator and Three-Dimensional Delaunay Triangulator, User's Manual / Weierstraß-Institut für Angewandte Analysis und Stochastik, Berlin. 2004. – Forschungsbericht

[24] Edelsbrunner, H.: Incremental Topological Flipping Works for Regular Triangulations. In: *Algorithmica* 15 (1996), Nr. 3, S. 223–241

[25] Shewchuk, J.: General-Dimensional Constrained Delaunay and Constrained Regular Triangulations, I: Combinatorial Properties. In: *Discrete and Computational Geometry* 39 (2008), Nr. 1, S. 580–637

[26] Paul Chew, L.: Constrained delaunay triangulations. In: *Algorithmica* 4 (1989), Nr. 1, S. 97–108

[27] Shewchuk, J.: Constrained Delaunay Tetrahedralizations and Provably Good Boundary Recovery. In: *Proceedings of the 11th International Meshing Roundtable* (2002), S. 193–204

[28] Schönhardt, E.: Über die Zerlegung von Dreieckspolyedern in Tetraeder. In: *Mathematische Annalen* 98 (1928), Nr. 1, S. 309–312

[29] Bagemihl, F.: On indecomposable polyhedra. In: *American Mathematical Monthly* 55 (1948), Nr. 7, S. 411–413

[30] Pebay, P. ; Frey, P.: A Priori Delaunay-Conformity. In: *Proceedings of 7th International Meshing Roundtable, SANDIA* (1998)

[31] Murphy, M. ; Mount, D. ; Gable, C.: A point-placement strategy for conforming Delaunay tetrahedralization. In: *Proceedings of the eleventh annual ACM-SIAM symposium on Discrete algorithms* (2000), S. 67–74

[32] Si, H. ; Gärtner, K.: Meshing Piecewise Linear Complexes by Constrained Delaunay Tetrahedralizations. In: *Proceedings of the 14th International Meshing Roundtable* (2005), S. 147–163

[33] Shewchuk, J.: Adaptive Precision Floating-Point Arithmetic and Fast Robust Geometric Predicates. In: *Discrete and Computational Geometry* 18 (1997), Nr. 3, S. 305–363

[34] Delaunay, B. N.: Sur la sphère vide. In: *Izv. Akad. Nauk SSSR, Otdelenie Matematicheskii i Estestvennyka Nauk* 7 (1934), S. 793–800

[35] Rajan, V.: Optimality of the Delaunay triangulation in $\mathbb{R}^d$. In: *Discrete and Computational Geometry* 12 (1994), Nr. 1, S. 189–202

[36] Lawson, C.: Software for C^1 surface interpolation. In: *Mathematical Software* 3 (1977), S. 161–194

[37] Meijs, J. W. ; Weier, O. W. ; Peters, M. J. ; Oosterom, A. van: On the numerical accuracy of the boundary element method. In: *IEEE Transactions on Biomedical Engineering* 36 (1989), Oct, Nr. 10, S. 1038–1049

[38] Fisher, R. S. ; Vickrey, B. G. ; Gibson, P. ; Hermann, B. ; Penovich, P. ; Scherer, A. ; Walker, S.: The impact of epilepsy from the patient's perspective I. Descriptions and subjective perceptions. In: *Epilepsy Res* 41 (2000), Aug, Nr. 1, S. 39–51

[39] Ben-Menachem, E. ; Hellström, K. ; Waldton, C. ; Augustinsson, L. E.: Evaluation of refractory epilepsy treated with vagus nerve stimulation for up to 5 years. In: *Neurology* 52 (1999), Apr, Nr. 6, S. 1265–1267

[40] Engel, J. J. (Ed.): *Surgical Treatment of the Epilepsies.* New York: Raven Press, 1987

[41] Luders, H. ; Awad, I.: *Epilepsy Surgery.* Kap. Conceptual Considerations, S. 51–62, New York: Raven Press, 1992

[42] *CURRY Reference Guide.* Compumedics Neuroscan, 1999

[43] Hill, D. L. G. ; Maurer, C. R. ; Wang, M. Y. ; Maciunas, R. J. ; Barwise, J. A. ; Fitzpatrick, J. M.: *Lecture Notes in Computer Science.* Bd. 1205: *Estimation of intraoperative brain surface movement.* Springer, 1997. – 449–458 S

[44] Lanfer, B.: *Validation and Comparison of Realistic Head Modelling Techniques and Application to Tactile Somatosensory Evoked EEG and MEG Data*, Universität Münster, Diplomarbeit, 2007

[45] Makeig, S. ; Bell, A. ; Jung, T. ; Sejnowski, T. et al.: Independent component analysis of electroencephalographic data. In: *Advances in Neural Information Processing Systems* 8 (1996), S. 145–151

[46] Oosterom, A. van ; Strackee, J.: The Solid Angle of a Plane Triangle. In: *IEEE Transactions on Biomedical Engineering* BME-30 (1983), Nr. 2, S. 125–126

Danksagung

An dieser Stelle möchte ich folgenden Personen für die vielfältige Unterstützung danken, ohne die diese Arbeit nicht möglich gewesen wäre:

Herrn Prof. Rudolf Friedrich, Institut für Theoretische Physik, für die Übernahme der fachlichen Betreuung meiner Diplomarbeit,

Herrn Prof. Christo Pantev, Institut für Biomagnetismus und Biosignalanalyse, für die Möglichkeit, diese Diplomarbeit an seinem Institut zu erstellen,

Herrn PD Carsten Wolters, der mich allzeit gut fachlich betreut und jederzeit meine Fragen beantwortet hat,

Herrn Dr. Thomas Dierkes und Herrn Dipl.-Phys. Benjamin Lanfer, für anregende Diskussionen und viele hilfreiche Tipps,

und nicht zuletzt meinen Eltern, für ihre fortwährende Unterstützung während meines Studiums.

Erklärung

Hiermit versichere ich, dass ich die vorliegende Arbeit selbstständig verfasst und keine anderen als die angegebenen Quellen und Hilfsmittel verwendet sowie Zitate kenntlich gemacht habe.

Münster, den 27. Juni 2008

Christian Röer